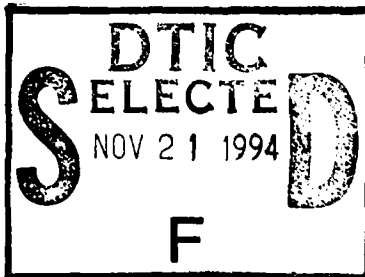AD-A286 435

Global Acoustic Mapping of Ocean Temperatures

GAMOT

°C

Woods Hole Oceanographic Institution
The Pennsylvania State University
Naval Research Laboratory–Stennis
The Florida State University
University of Alaska
University of Texas at Austin

DTIC QUALITY INSPECTED 6

QUARTERLY PROGRESS REPORT
July–September 1994
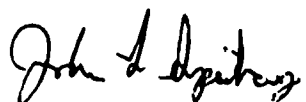
GAMOT

October 15, 1994

Dr. Ralph Alewine
Advanced Research Projects Agency
3701 North Fairfax Drive
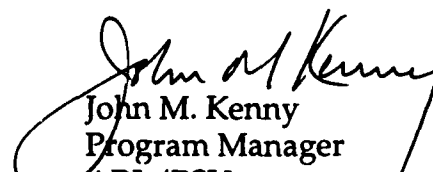Arlington, VA 22203-1714

Dear Dr. Alewine,

The attached report fulfills the sixth quarterly progress report requirement for the period from July 1 to September 30 1994 as contained in the ARPA Grant No: MDA972-93-1-0004 entitled "Real Time System for Practical Acoustic Monitoring of Global Ocean Temperature" issued by the Contracts Management Office. The United States Government has a royalty-free license throughout the world in all copy rightable material contained herein. This report is approved for unlimited distribution and public release. Copies of this report are also mailed to the distribution list contained in Attachment Number 2 of the Grant.

Financial status reports will be submitted separately from this report. Woods Hole Oceanographic Institution, as the Grantee, will submit all financial reports directly to you.

The information contained in this report represents the inputs and opinions of the entire GAMOT team; the Woods Hole Oceanographic Institution, the Pennsylvania State University, the Florida State University, University of Alaska, University of Texas at Austin and NRL-Stennis. If this report generates any questions, please do not hesitate to direct your questions or comments to the Principal Investigators or the Program Manager.

John L. Spiesberger
Principal Investigator
WHOI/PSU

Daniel E. Frye
Principle Investigator
WHOI

John M. Kenny
Program Manager
ARL/PSU

A-1

GAMOT EXECUTIVE SUMMARY

Work continues on all GAMOT Tasks as described in ARPA Grant No: MDA972-93-1-0004.

- **Task A.** Task A work remains on schedule.

The acoustic multipaths from the Kaneohe source have been identified at one SOSUS station using a ray tracing algorithm called ZRAY. This is the furthest, 4000 km, that ray theory has been successfully used to understand acoustic propagation in the ocean. This further validates that acoustic thermometry is valid at basin-scales and that changes in the travel time from the Kaneohe source are not due to changes in the multipaths.

We also found that there is no such thing as axially trapped energy for basin scale transmission near 130 Hz. Sound, which would otherwise be trapped at the axis, is vertically scattered more than 1000 m from the axis by fluctuations smaller than the mesoscale.

We devised a new theory for the climate shift observed in the Pacific in the mid 1970's. Our theory is based on an oceanographic origin for the changes. The basic idea is that Rossby waves change the depth of the seasonal and main pycnoclines. By changing the pycnocline depths, the wintertime sea surface temperatures can be modulated because the pycnocline depths are a barrier to the mechanical mixing of water in the winter

We have ported the second version of the tomography signal processing software to the SSAR. The software has the second revision of the peak-picking algorithm. The software now includes an adaptive coherent integration time so that we maximize the signal-to-noise ratio for each reception. This software performs Doppler correction, circulating sums, matched filtering and pulse compression, estimation of multipath arrival angle, and peak-picking. The tomography processing software will be used at to test the SSAR at in the Pacific this November.

We analyzed the SSAR data from the August 1994 AUTEC test and found that the SSAR data was consistent with the expected multipaths computed from a ray trace algorithm. Thus, much of the software and hardware for the SSAR appear to be operating properly.

- **Task B.** Task B tasks and deliverables are on schedule.

FSU designed an acoustic tomography assimilation scheme for a reduced gravity model, but with spatially variable density. The goal of this effort is to estimate the time independent density field in the upper northeast Pacific ocean.

NRL discovered the decadal impacts of the 1982-83 El Niño. They are investigating the five year changes in sea surface height observed by satellite altimeter data and simulated by eddy resolving global and basin scale models. They performed two "identical twin" 1/8 degree eddy resolving simulations of the Pacific ocean north of 20S. NRL has assumed the responsibility to work with Mississippi State University to develop visualization techniques.

The University of Alaska continues the work on the validation of the GAMOT methodology to derive ocean temperature, and hence travel times, from the NRL model.

• **Task C:** A second test cruise was conducted at the AUTEC Range in August to verify SSAR performance with a 70 Hz source. This test consisted of the deployment of a normal SSAR (Snubber design) and a moored SSAR. The moored SSAR was deployed on a subsurface mooring, thus removing surface generated noise. A 70 Hz source transmitted an M-sequence signal and both systems recorded data on hard disk. The normal SSAR also telemetered processed data. In addition, the SSAR acoustic navigation system was tested against the AUTEC Range system. All data were successfully collected and processing of this information is ongoing.

In October a test of the SSAR was conducted in open water offshore Florida. In this test two SSARs (Snubber design) were deployed. One was configured to listen for low frequency sounds in the 10-50 Hz range while the other was configured in the standard mode; i.e., 30-100 Hz band. Both units recorded data to disk and telemetered processed data. This cruise was successful and the data are being evaluated.

Preparations are underway for deployment of three SSARs (two Snubber, one Standard) in the Pacific during the ATOC ATE. These SSARs will be deployed about 500 km from the FLIP-mounted source and will record raw data on disk and telemeter processed data via satellite. All of the units will be retrieved at the end of the test.

Fabrication of the remainder of the operational SSARs is continuing. It has been delayed somewhat by the preparations for the Atlantic and Pacific tests, but is anticipated to be completed by the end of the year.

The SSAR design is complete and a Design and Test Report will be available at the end of December. The schedule for this deliverable was delayed due to the busy test schedule between August and November. The new coil cord design used in the hose worked well during the Atlantic test but a problem was uncovered and is being addressed in a modified design. In-house tests of this component are continuing at WHOI. Several techniques for attaching the hydrophones to the acoustic array were also tested during the Atlantic test. This data is still under evaluation and further tests are planned for the Pacific deployments in November. The goal of these tests is to identify the

technique that minimizes in band noise due to impulses resulting from the non-linear interaction between the SSAR systems and surface waves.

Design work has begun on the low power receiver. No significant problems have been encountered.

• **Task D.** No action has been taken on Task D this quarter.

• **Meetings.** . Members of the GAMOT team attended several conferences including MTS '94, the Hong Kong AGU, and the TOS Pacific Basin Meeting, and presented their work. The GAMOT modellers met at Penn State for a two day working group meeting.

Issues and Concerns: One issue is addressed:

• The October Atlantic Test was not part of our original Task C requirements. As a consequence, the resources set aside for deployment of the operational SSARs were used to perform this important test (with ARPA's concurrence). Thus, new funds are needed to conduct the deployment cruises.

Three papers are contained in this report:
Spiesberger, J., Kaneohe Acoustic Thermometer Further Validated With Rays Over 3700 KM And The Demise Of The Idea Of Axially Trapped Energy, submitted to J. Acoust. Soc. Am., (1994).

Schchepetkin, A. F., O'Brien, J.J., A Physically Consistent Formulation of Lateral Friction in Shallow Water Equation Ocean Models, (1994).

Paul, W., Bocconcelli, A., Drifting Buoy System Using Rubber Stretch Hose, to be published in the December 1994 issue of *Sea Technology*.

TASK A
TOMOGRAPHIC DATA ANALYSIS

In the last quarter we have accomplished the following tasks.

The acoustic multipaths from the Kaneohe source have been identified at one SOSUS station using a ray tracing algorithm called ZRAY. This was a breakthrough since this is the furthest, 4000 km, that ray theory has been successfully used to understand acoustic propagation in the ocean. The acoustic source was centered at 133 Hz. Travel times from this section have been compared to an eddy resolving section taken in July 1988 by NAVOCEANO. We find that ray travel times through the CTD section are consistent with measured travel times.

This manuscript further validates that acoustic thermometry is valid at basin-scales. We confirm our previous publications in that we demonstrate that temperature is the only ocean parameter that can lead to the observed changes in travel time at basin scales in the northeast Pacific. We prove that the changes in the travel time from the Kaneohe source are not due to changes in the multipaths.

This manuscript also finds that there is no such thing as axially trapped energy for basin scale transmission near 130 Hz. We find that sound, which would otherwise be trapped at the axis, is vertically scattered more than 1000 m from the axis by fluctuations smaller than the mesoscale. The most likely cause of the scattering is internal waves. A copy of the manuscript, submitted to the J. Acoust. Soc. Am., is included in this report. It is titled ``Kaneohe acoustic thermometer further validated with rays over 3700 km and the demise of the idea of axially trapped energy,'' (Spiesberger, 1994).

We devised a new theory for the climate shift observed in the Pacific in the mid 1970's. Our theory is based on an oceanographic origin for the changes. The basic idea is that Rossby waves change the depth of the seasonal and main pycnoclines. By changing the pycnocline depths, the wintertime sea surface temperatures can be modulated because the pycnocline depths are a barrier to the mechanical mixing of water in the winter. If our theory is valid in part, the ramifications are important because it may be possible to predict sea surface temperatures years ahead of time, because we now know it possible to predict some Rossby waves years ahead of time (Jacobs et al., 1994). Since the atmosphere is in direct contact with the sea surface, it might then be possible to predict atmospheric climate years ahead of time. A manuscript with our findings is included in this report (Meyers, Johnson, Liu, O'Brien, and Spiesberger, 1994).

We have ported the second version of the tomography signal processing software to the SSAR. The software has the second revision of the peak-

picking algorithm. The software now includes an adaptive coherent integration time so that we maximize the signal-to-noise ratio for each reception. This software performs Doppler correction, circulating sums, matched filtering and pulse compression, estimation of multipath arrival angle, and peak-picking. The tomography processing software will be used at to test the SSAR at in the Pacific this November.

We are writing user-friendly SSAR data reading algorithms in preparation for SSAR data from the Pacific.

We analyzed the SSAR data from the August 1994 AUTEC test. We found that the SSAR data was consistent with the expected multipaths computed from a ray trace algorithm. Thus, much of the software and hardware for the SSAR appear to be operating properly.

We found that it is possible to localize some SOSUS stations to within 200 km in range and 500 m in depth from only the relative arrival times of multipaths. This localization is possible for transmission over 3000 km. The success of this localization is based on the success of using ray theory to interpret multipaths transmitted at basin-scales (Spiesberger, Terray, and Prada, 1994; Spiesberger, 1994).

This finding may have repercussions on what tomography data can be published. Because of this finding, we are considering how to communicate our results of our successful analysis of the fifteen basin-scale sections we collected in 1987 at SOSUS stations.

We are continuing to develop tomography processing software which will lead toward real-time mapping of ocean temperatures from moored sources, fixed sources, and fixed and drifting receivers. This work is outlined, specified, and is being coded.

We are using the FSU and NRL ocean models to compute changes in travel time between the Kaneohe source and seven SOSUS stations. These predicted changes in travel time through these models have many of the same characteristics as observed. This analysis will lead to a manuscript to be written later this Fall.

We are working on a transition plan to take the GAMOT technology between the University setting and a government agency. This work is underway, and is scheduled for completion by next summer.

We are modifying our tomography inverse program to account for the real-time enabling telemetry scheme which will allow localization of autonomously moored sources to better than 6 m in real time.

We are computing temperature changes from the NRL model to compare with XBT data taken in the last decade. The purpose of this is to make consistency checks of the NRL model with data. This work is being done in collaboration with the modellers in the GAMOT group.

2

REFERENCES

1. Jacobs, G.A., H.E. Hurlburt, J.C. Kindle, E.J. Metzger, J.L. Mitchell, and W.J. Teague, ``Decade scale transpacific propagation and warming effects of an El Nino anomaly," *Nature*, 370, p.360-363, (1994).

2. Meyers, S.D., Johnson, M., Liu, M., O'Brien, J.J., and Spiesberger, J.L., Interdecadal variability in a numerical model of the northeast Pacific Ocean. 1970-1989, in preparation, (1994).

3. Spiesberger, J.L., Terray, E., and Prada, K., Successful ray modeling of acoustic multipaths over a 3000 km section in the Pacific, J. Acoust. Soc. Am., 95, 3654-3657, (1994).

4. Spiesberger, J.L., Kaneohe acoustic thermometer further validated with rays over 3700 km and the demise of the idea of axially trapped energy, submitted to the J. Acoust. Soc. Am., (1994).

ENCLOSURE

Spiesberger, J., Kaneohe Acoustic Thermometer Further Validated With Rays Over 3700 KM And The Demise Of The Idea Of Axially Trapped Energy, submitted to J. Acoust. Soc. Am., (1994).

Figure

Fig. 1   Task A Schedule

NUM	TASK A	Start Date	Finish Date	1993 — 1994 — 1995 timeline
A.1	ESTIMATE IMPROVED RESOLUTION FROM SSAR BY NUMERICAL SIMULATION	1/15/94	1/15/95	
A.2	DETERMINE THE OPTIMUM :			
	SSAR ARRAY DEPTH	5/1/93	6/30/93	
	SOURCE LOCATION AND DEPTH	5/1/93	11/30/93	
A.3	ESTIMATE THE INFLUENCE OF FREQ, INCLINATION, DISTANCE AND SVP ON MULTIPATH STABILITY	5/1/93	6/30/95	
A.4	DEVELOP ALGORITHMS AND COMPUTATIONS WHICH:			
	DO NOT GENERATE EXTRANEOUS EIGEN RAYS	5/1/93	5/15/93	
	CALC LOSS FOR GEOMETRIC RAYS	5/1/93	5/15/93	
	CALC LOSS FOR SHADOW ZONES OF CAUSTICS	5/1/93	5/15/93	
A.5	INCORPORATE THE RAY TRACE ALGORITHM INTO THE INVERSE PROGRAM	7/15/93	5/15/94	
A.6	ASSIMILATE TOMO DATA INTO O'BRIEN OCEAN MODEL	12/18/94	7/2/95	
A.7	AUTOMATE THE PROCEDURE TO CHANGE SPATIAL COORDS OF MULTIPATHS DUE TO SEASONAL CYCLE	5/1/93	6/30/95	
A.8	DEMO REAL TIME TOMOGRAPHY:			

NUM	TASK A	Start Date	Finish Date
	USING DATA FROM SSAR	12/18/94	6/30/95
	USING DATA FROM FIXED RCVRS	12/18/94	6/30/95
A.9	ANALYSIS OF 1987 TOMO DATA TO DETERMINE SEASONAL CYCLE INFLUENCES ON ACOUSTIC TRAVEL TIMES:		
	FORWARD PROBLEM	7/15/93	6/30/94
	INVERSE PROBLEM	9/15/93	12/18/94
A.10	SIMULATION OF OCEAN CLIMATE TEMPS FROM AN O'BRIEN OCEAN MODEL USING SSARS	5/1/94	5/30/95

Timeline header: 1993 — A M J J A S O N D; 1994 — J F M A M J J A S O N D; 1995 — J F M A M J J

KANEOHE ACOUSTIC THERMOMETER FURTHER VALIDATED WITH RAYS OVER 3700 KM AND THE DEMISE OF THE IDEA OF AXIALLY TRAPPED ENERGY

John L. Spiesberger

Department of Meteorology and the Applied Research Laboratory, 512 Walker Bldg.,

Pennsylvania State University, University Park, Pennsylvania 16802

1

ABSTRACT

In the 1980's, the Kaneohe source, on the north shore of Oahu, transmitted sound at 133 Hz, 60 ms resolution from 183 m depth to a U.S. Navy receiver at 3709 km distance at 1433 m depth near northern California. Delays of these acoustic arrivals were previously related to the average temperature change along the section, even though models for the propagation of sound could not reproduce the data [J.L. Spiesberger et al., J. Acoust. Soc. Am., **92**, p.384-396, (1992)]. Despite the fact that sound reflects one or more times from the Oahu slope before being trapped in the sound channel, ray theory is shown capable of determining the spatial coordinate of the acoustic pulses whose delays are tracked in the 1980's. Rays that bounce from the bottom are probably chaotic, but the coordinates and travel times of eigenrays are insensitive to initial conditions and ocean fluctuations. The stability of these eigenray paths, inclined at about 15° at the sound-channel axis, provides further evidence that the changes in delay of $\sim \pm 0.2$ s observed in the 1980's are due to temperature and not due to changes in the multipaths. To date, this is the longest distance over which stable and repeatable features in an acoustic data set have been successfully modelled. The coda of the reception can probably not be explained with a propagation model in which the sound speed field is smoothed to suppress scales smaller than the mesoscale. Instead, scattering of sound from smaller scales, perhaps associated with internal waves, distributes otherwise axially-trapped sound more than 1000 m in the vertical. These scattering processes impose fundamental limits on the vertical resolution achievable with tomog-

2

raphy. The idea that sound samples the ocean along vertically thin ray paths needs to be replaced with the idea that the thickness of some sound paths can be more than a 1000 m; the scale of the acoustic waveguide.

I. INTRODUCTION

Between 1983 and 1989, the Kaneohe acoustic thermometry experiment detected interannual changes in ocean temperature at basin-scales in the northeast Pacific.[1,2] Signals at 133 Hz, 60 ms resolution, were transmitted from the Kaneohe source to more than eight receivers known as U.S. Naval Sound Surveillance Systems (SOSUS). Receptions at one of these stations, at about 3709 km distance, are studied in more detail here than previously possible because the Navy recently allowed publication of the receiver's position (Fig. 1).

The travel time changes of these acoustic signals, typically ±0.2 s, can be converted to changes in the spatially averaged temperature along a section within ±0.02 °C (Fig. 2).[2,3] The accuracy of ±0.02 °C is limited by fluctuations other than temperature such as associated with currents and salinity. Although this acoustic thermometer is a sensitive method for recognizing average changes in temperature, until now no acoustic model had successfully reproduced the acoustic pattern of pulses detected at the receiver.[2,3] Since some acoustic arrivals are stable in the presence of ocean fluctuations and since their travel times can be measured from day- to-day for many years (Figs. 3 and 4), there must be some solution of the acoustic wave equation which also yields pulsed acoustic arrivals whose patterns are stable in the presence of

3

fluctuations. The difficulty in modelling sound from the Kaneohe source is related to the fact that sound reflects at least once from the steep north slope of Oahu before becoming trapped in the acoustic waveguide of the north Pacific (Fig. 7 of Ref. 2).[4,5] This reflection from the bottom is due to the shallow 183 m depth of the source. Although the distance of propagation is long, it is probably not the primary reason for previous modelling difficulties because ray theory successfully accounts for propagation near 250 Hz over 3000 km in the northeast Pacific.[6]

The Kaneohe source data are re-examined with a recent ray trace program, ZRAY,[6,7] and an eddy-resolving survey of temperature and salinity taken along the section in July 1988. Twelve new results given in this paper are:

1. Ray theory is adequate for determining the travel times and spatial coordinates of the acoustic pulses found to be stable in the records (Arrivals A-E in Figs. 3 and 4). These ray paths can be assumed to be frozen in the presence of ocean fluctuations, as inferred before (Appendix B in Ref. 2).

2. To date, this 3709 km section is the longest in which stable arrivals are successfully interpreted with a model for the propagation of sound in seawater.

3. Some ray trajectories are sensitive to initial conditions, and may be chaotic. This unpredictability is probably due to the fact that all rays reflect from the volcanic

4

slope of Oahu.

4. The spatial coordinates of eigenrays are insensitive to initial conditions and fluctuations in the ocean. Evidently, eigenrays, which pass through both the source and receiver, are more insensitive to fluctuations than ray paths, which are not constrained to pass through the receiver. The additional constraint that eigenrays pass through the receiver selects ray paths with similar geometries in the presence of fluctuations.

5. Rays A-E sample similar locations in the ocean. This explains why the stable arrivals all change travel times by about the same amount at the same time.[2]

6. The upper turning depths of rays A-E are almost entirely below the seasonal thermocline, as inferred previously.[2] The seasonal cycle of travel time is predicted here to have an amplitude of less than 0.05 s.

7. Given ray coordinates for stable arrivals, acoustic tomography could be applied to these data in the future to infer changes in average temperature as a function of depth[8,9]

5

8. The differences in delay of 0.2 to 0.4 s between measurements and ray predictions are plausible.

9. The coda of each reception cannot be explained with models whose sound speed profiles are smoothed to suppress structures smaller than the mesoscale.

10. The coda might be understood by accounting for the scattering of sound from smaller scales, such as associated with internal waves. Sound that is otherwise trapped near axis depth in smoothed models is scattered by smaller scales more than 1000 m in the vertical at the receiver. The concept that sound propagates along thin ray paths needs to be replaced by a picture in which some or all sound paths have vertical extents of thousands of meters; the vertical scale of the acoustic waveguide. Because of this scattering, the adiabatic approximation is invalid for sound initially trapped near the sound channel axis.

11. At basin-scales, the vertical resolution of tomographic maps is fundamentally limited by the vertical scattering of energy by fluctuations smaller than the mesoscale.

12. It is unclear how the theory for the scattering of sound by internal waves by Flatte et al.[10] is relevant for understanding acoustic aberrations in this experi-

6

ment. That theory computes wave strength and diffraction parameters along ray paths. Instead, it may be necessary to estimate the effects of ocean fluctuations on eigentubes whose vertical extents might be more than 1000 m.

Because ray theory is computationally efficient and simple to interpret, it is important to explore the limits of its utility.

II. EXPERIMENT AND DATA

The Kaneohe source is mounted on the bottom at 183 m depth on the north coast of Oahu. Its position is 21.51235 °N, 202.22849 °E in the World Geodetic System 1984. This position is measured with an r.m.s. error of about ±20 m (Ref. 2). The location of the SOSUS receiver is 40.07856 °N, 234.88797 °E, and is located on the bottom at 1433 m depth. The receiver was originally located using benchmarks on the California coast and acoustic ship surveys. In 1987, Spiesberger re-surveyed two of these benchmarks with a Global Positioning Satellite (GPS) system. He verified that their previously reported positions were accurate to ±15 m. The position of the SOSUS receiver is thus measured with an r.m.s. error of about ±20 m. The depth of the source and receiver have r.m.s. errors of about 10 m.

The geodesic distance between the source and the receiver, 3709.21 km, is computed on the WGS-84 reference ellipsoid with a program published by NOAA.[11] Transmission and arrival times were measured with atomic standards to within 1 ms (Ref. 2). The

source level was about 183 dB re 1 μPa @ 1 m. A linear maximal sequence generator was used to modulate the phase of the 133 Hz carrier to produce a pulse resolution of about 0.06 s. Detailed description of the experiment and signal processing is discussed elsewhere.[2,12,13]

Fig. 3 shows daily incoherent averages of the processed acoustic signals computed according to,

$$a(t) = \left(\frac{1}{N} \sum_{n=1}^{N} \frac{1}{\sigma_n^2} I[t(n)] \right)^{1/2} .$$

The arrival time is t, the number of pulse-like transmissions is N, the variance of the acoustic noise in each record is σ_n^2, the arrival time of a multipath for the nth transmission is $t(n)$, and the intensity of a multipath is $I[t(n)]$. In 1983 there were about 700 transmissions per day and in later years about 70 per day.[2] Arrivals A-E are stable throughout the experiment (Figs. 3 and 4). Since the changes in travel time of these arrivals are almost identical throughout the experiment, their average delay changes are plotted for simplicity (Fig. 2). The travel time changes of ± 0.2 s are typical for changes observed at six other SOSUS receivers.[2] However, these other data change quite differently than the travel times shown in Fig. 2, indicating that section-averaged temperature is structured in the Pacific.[2]

III. RAYTRACING WITH ZRAY

Details of the raytracing algorithm, ZRAY, and its eigenray finder are discussed elsewhere.[6,7] The algorithms compute travel time, ray coordinates, and amplitudes for geometric and non-geometric rays in a vertical slice of the ocean. A non-geometric ray

8

corresponds to energy reaching a receiver in the shadow zone of a caustic. The travel time of the non-geometric eigenray is computed by calculating when a plane wave, perpendicular to the caustic, crosses the receiver (Fig. B3 of Ref. 9). Amplitudes for geometric and non-geometric eigenrays are estimated with standard relations (Eqns. (2.5.3) and (2.5.6) of Ref. 14). The vertical slice coincides with the geodesic between the source and the receiver. Sound speed is computed from CTD data or from Levitus's[15] seasonal values of temperature, salinity, and depth with Del Grosso's[16] algorithm. The months corresponding to Levitus's seasons are Aug-Oct (Summer), Nov-Jan (Fall), Feb-Apr (Winter), and May-July (Spring). Vertical profiles of the speed of sound are specified at Levitus's standard depths.[15] The profiles are taken at 100 km intervals to smoothly represent variations of sound speed along the section. In Spring, the depth of minimum sound speed is 800 m near the source and 500 m near the receiver (Fig. 5). The Earth flattening transformation is used to account for the curvature of the Earth.[17]

ZRAY computes rays by numerically integrating a system of differential equations. Unless otherwise indicated, rays are traced with the following precision. A Runga-Kutta algorithm of 4th degree is used, with a maximum and minimum step size in the vertical of 50 and 1.25 m, with the multiplier parameter, multiplier, set to 0.125 (p. 42-43 in Ref. 7).

The depth of the bottom is measured within about 2% of the total depth within 130 km of the source. Bottom depths along the last 100 km near the receiver are probably

measured to within 50 m. Between these two bathymetric data bases, depths are extracted at 9 km intervals from ETOPO5.[18] Rays are taken to reflect specularly from the bottom and surface. We assume that the energy lost from each bottom reflection is 3 dB.

ZRAY represents the bottom with quadratic splines to avoid discontinuities in slope. Bottom depths are filtered with a horizontal length scale of 1 km before the quadratic splines are fit to the data. The bottom is smoothed because the eigentubes of acoustic energy interact with the bottom over a non- zero length. We guess this length to be one kilometer. Quantitative estimate of this length scale is beyond the scope of this paper because that scale would require constructing eigentubes which are numerically intensive to compute.[19] After low pass filtering and fitting quadratic splines with ZRAY, the source is located at the filtered bottom depth of 162 m.

Travel times and amplitudes of rays are processed like the acoustic data.[12,13] The impulse response of ZRAY is convolved with a Gaussian envelope about 0.06 s wide containing a 133 Hz carrier wave. This is complex demodulated to zero Hz and low pass filtered to remove the double frequency component of the demodulated signal.

IV. RAYTRACES COMPARED WITH DATA

A. Raytracing using climatological averages

The ray impulse responses from all of Levitus's climatological seasons compare quite well with stable arrivals A-E (Figs. 6,7). The duration of the arriving energy is about

three and one-half seconds in both data and model. We needed to find a solution of the wave equation yielding stable arrivals A-E in the presence of ocean fluctuations. We have done so with rays in the context of Levitus's climatological averages.

We could not find any acoustic features that could be tracked over many months to years following arrival E in the data (Fig. 4). Ray predictions are also not trackable from season to season following arrival E (Fig. 7). Raytraces indicate that arrivals following E are unresolved compared to the pulse resolution of about 0.060 s (Fig. 8). These unresolved rays may interfere in significantly different ways as the ocean fluctuates, and thus lead to arrivals that are unstable from month-to-month.

It is an accident that the impulse response from our ray theory has the same duration, about 3.5 s, as the data (Fig. 6). Most of the rays in the last few seconds of the predictions are non-geometric. The receiver, located in the shadow zone, is up to 1000 m below the caustic surface (Fig. 8). The formula used for these non-geometric intensities is invalid. It assumes that the speed of sound varies linearly with depth. This is not a good approximation for rays 800 to 1000 m above the receiver depth of 1433 m. These caustics are near the minimum of sound speed in the waveguide where the speed of sound varies quadratically rather than linearly with depth. The reason the formula for intensity predicts energy up to 1000 m away from a caustic is that these caustics, near the sound channel axis, have very large radii of curvature. According to the formula we use, intensity in the shadow zone monotonically increases with the radius of curvature.

11

Insignificant energy would be predicted to reach the receiver even if we utilized a formula for intensity in a shadow zone valid for our background sound speed profiles. Instead, we hypothesize that sound is scattered at least 1000 m vertically by ocean fluctuations. To obtain reliable amplitudes of multipaths, acoustic models need to incorporate scattering processes.

Previous analysis predicted that arrivals A-E have similar upper turning depths because the they all change travel time by the same amount at the same time.[2] This prediction is correct. Upper turning depths for rays A-E differ by at most 150 m (Fig. 9).

Each stable arrival, A-E, is composed of many eigenrays. The rays making up any one stable arrival have upper turning depths within 50 m of one another (Fig. 10). The upper turning ranges are usually different (not shown). Paths A-E are inclined at about 15° to the horizontal at the depth where the speed of sound is minimum in the waveguide.

If ray paths A-E are not spread too much in the vertical by scattering processes. tomographic maps of range-averaged temperature as a function of depth might be made using their ray coordinates (Fig. 11), These maps would be insensitive to choice of ray path because the ocean is sampled in the vertical almost identically by each eigenray making up a stable arrival. The upper turning depths of the eigenrays change by less than 50 m as the seasons progress (Fig. 10). Thus, the ray coordinates are insensitive to season, and one could assume the ray paths to be frozen in the presence of ocean

fluctuations to excellent approximation. A linear tomographic inversion would be well justified since the tomographic inversion is linear if the ray paths are accurate enough.

Rays A-E reflect from the volcanic slope at least once before becoming trapped in the acoustic waveguide in the northeast Pacific (Fig. 11; Table I). Their upper turning depths shoal as they travel into colder waters toward the north.

Travel times show little evidence of a seasonal cycle at this or the other SOSUS receivers (Fig. 2; Fig. 1 in Ref. 2). At this receiver, raytraces predict a seasonal cycle whose amplitude is less than 0.05 s, with longer travel times during the Winter (Fig. 12). The small seasonal variation is due to the fact that these rays travel almost entirely below the upper 100 m marking the lower limit of the seasonal thermocline.[20,21]

B. Raytracing using CTD section

Fifty-six CTD's were taken along the section between 6 and 19 July 1988 (Figs. 1, 13, and 14). Compared with Levitus's spring-time conditions, sound speeds exhibit a field of eddies and long waves having maximum perturbations between ± 2 m $\cdot$ s^{-1}. to ± 8 m $\cdot$ s^{-1} near 100 to 300 m depth. These are equivalent to temperature perturbations of about ± 0.5 to ± 2 °C. A dynamical analysis of these fluctuations is beyond the scope of this paper.

Tracing rays with this CTD section yields arrivals A-E (Fig. 15). Remarkably, travel times and coordinates computed from the CTD and Levitus data are almost identical (Figs. 10 and 15). Travel times compared with Levitus's Spring are within 0.03 s. The upper turning depths are within 25 m (Fig. 10). The spatial coordinates

13

of eigenray paths A-E are insensitive to realistic fluctuations.

Measured minus predicted travel times

For arrivals A-D, measured travel times exceed those based on raytracing using the CTD data by between +0.21 and +0.39 s (Table II). These differences are significant compared to the precision with which the acoustic delay is measured over a week, about 0.01 s (Ref. 2).

A plausible scenario accounts for differences up to about 0.5 s (Table III). Two-tenths of this half-second could be due to a warming of the ocean between early May and mid July; a plausible change given the observed rate at which travel times change from month-to-month (Fig. 2). If a warming did occur, it was probably not dominated by the seasonal cycle which is predicted to be only about ±0.05 s. However, a change of -0.2 s is equivalent to a reasonable change in the ocean's temperature, as can be gathered from the following. The distance, L, rays A-E spend in the upper kilometer is about 1060 km out of a total distance of 3709.21 km. The average change in temperature due to a travel time change, δt, is,

$$\delta\theta \cong -\frac{c\delta t}{3.19 \times 10^{-3}L} \quad (^\circ C) \; , \qquad (1)$$

where the average speed of sound is c (Eqn. (4) in Ref. 2). For $L = 1060$ km, $c = 1.5$ km $\cdot$ s^{-1}, and $\delta t = -0.2$ s, we get an average change in temperature of $\delta\theta = +0.088$ °C in the upper kilometer (right-hand axis, Fig. 2).

Uncertainty in Del Grosso's algorithm for the speed of sound in seawater[16] leads

to an uncertainty in delay of about 0.12 s. His algorithm for sound speed would have to be too fast in order reduce the travel time differences in Table II. The whole story about what a more accurate algorithm for sound speed might be has been the subject of recent interest.[22-26]

Rays are assumed to reflect specularly from the bottom but a more complete accounting for the interaction with the bottom is possible. This remains for the future. Other possible causes of the travel time differences are discussed in the Appendix.

C. Ray sensitivity

To test the sensitivity of the raytrace result to changes in geometry, the geodesic distance is increased by 140 m and the depth of the source increased by 13 m. No significant change in the impulse response is found for arrivals A-E (not shown). This coordinates of eigenrays are insensitive to small changes in geometry.

The transition from predictability to chaos is characterized by an exponential growth in the number of rays required to determine eigenrays and by an increase in the number of eigenrays contained in a stable acoustic arrival.[27-31] Some rays reflecting from the Oahu slope are sensitive to initial conditions. One test for ray chaos is to see if the same ray can be obtained by tracing a ray from source to receiver, and then backwards from the receiver to the source. With an infinite precision computer, reciprocity is obeyed. With a finite precision computer, it may be impossible to obey reciprocity if the ray coordinates are chaotic, and it is then difficult to get the same ray path from forward and backward ray traces. For eigenrays A-E, we cannot obtain the same path when

15

the raytrace is reversed, even when the integration step size is decreased to about 2 m (Fig. 16). However, given any fixed geometry and sound speed field, the coordinates and travel times of eigenray paths change little.

Palmer et al.[27] examined chaotic rays which reflect from the bottom of the ocean. They found that travel times were insensitive to initial conditions, even though particular ray trajectories were sensitive to initial conditions. Instead of one ray making up an acoustic arrival, they found a multiplicity of rays in an acoustic arrival. Many of these predictions apply to this section. For example, there are many rays with similar coordinates making up each stable arrival A-E (Fig. 10).

We find that eigenray paths A-E required more computation than in a 3000-km section in the Pacific where bottom interactions were unimportant.[6] In our use of ZRAY, a fan of evenly spaced rays is launched over a range of inclination angles. The eigenray finder iterates on this fan at finer resolution to estimate geometric and non-geometric rays. For the 3000-km section, we required an initial fan density of 100 rays per degree of inclination to determine a satisfactory set of eigenrays. For the section from the Kaneohe source, we required a ray density of 800 rays per degree of inclination. In both the 3000-km and Kaneohe source cases, the integration step sizes were identical. The fact that many more rays are required for the longer section may be evidence of the transition to ray chaos.

Paths previously found useful for studying climatic temperature variability over basin-scales were rather steep, about 10° to the horizontal at the sound channel axis.[9]

16

Paths A-E are steep also, being inclined at about 15° at the axis. To date, only steeply inclined paths have been used to map basin-scale changes in ocean temperature at distances of a few thousand kilometers or greater. Flatly inclined paths are believed to be more sensitive to fluctuations.

D. Scattering of sound from the mesoscale

Tracing rays through an unstructured ocean, based on Levitus's climatological averages, does not explain why significant energy is observed in the last second of the data (Section IV, A). The question addressed here is whether rays traced through an ocean structured with eddies yield significant energy at the observed coda.

Fig. 17 shows predictions, based on rays, for arrival times as a function of depth above the SOSUS receiver. If the observed acoustic data at the SOSUS receiver from Fig. 3 were plotted on the travel time scale in Fig. 17, significant energy extends to 7.4 s in Fig. 17. Between 6.5 and 7.4 s, the vertical distances between the non-geometric rays and the receiver are between 200 and 1000 m for both unstructured and structured oceans. Therefore, realistic mesoscale structure is inadequate for scattering energy nearer to the receiver depth than predicted for an unstructured ocean. We cannot explain why the last second of energy is observed by tracing rays through a realistic eddy field. We therefore hypothesize that structures smaller than the mesoscale must be accounted for to understand the vertical distribution of energy near the receiver.

V. DISCUSSION

Findings in this paper confirm most of the indirect inferences published before.

17

Travel time changes of arrivals A-D are excellent acoustic thermometers.[3,2] In partic-
ular, the changes in travel time along paths A-E are due to changes in temperature,
and not due to changes in the multipaths. By identifying the spatial coordinates of
rays associated with arrivals A- E, it is possible to use tomography[8] to infer changes
in range-averaged heat content as a function of depth as has been demonstrated using
another basin-scale section.[9] However, the vertical resolution of these maps is probably
limited by the vertical scattering of sound from scales smaller than the mesoscale.

Perhaps fluctuations from internal waves are the cause for the scattering of sound
over 1000 m in the vertical. The vertical scattering of energy in the ocean proba-
bly increases with distance from the source. Future research needs to pin down how
scattering depends on the launch angle of the energy from the source, the distance of
propagation, the acoustic frequency, and the large-scale features of the sound speed
profiles. The concept of an axially trapped ray is not useful or valid in this experiment.
The whole idea that the tomographic inverse problem can be cast in terms of thin rays
is in doubt and needs to be checked by including scattering processes in forward models
and theories. The Kaneohe source data can be used to test these models and theories.

A. Formulation of tomography with thick "rays"

The acoustic tomography inverse problem needs to be re-cast to account for the
fact that the vertical extents of some sound paths may be large and not thin like
rays. Define the wavefront of an eigentube, $w(s)$, to be an outward propagating wave
having the same pulse delay everywhere on its surface. Parameterize the center of the

18

wavefront by distance, s, from the source. The vertical extent of the wavefront is zero for a ray-like picture and can be more than a kilometer for eigentubes such as observed in this experiment. The change in travel time of the ith eigentube can be defined as,

$$\delta T_i \cong - \int_{\Gamma_i} \frac{ds_i}{c_0^2(s_i)} \int_{w_i(s)} d\chi_i \delta c(s_i, \chi_i(s_i)) A_i(\chi_i) \quad . \tag{2}$$

Γ_i denotes the center of the ith eigentube trajectory with differential increment ds_i, $c_0(s_i)$ is the reference speed of sound on $c(s_i)$. The line integral is evaluated along the wavefront $w_i(s)$ with differential element $d\chi_i$. This line integral weights changes in sound speed along the wavefront, $\delta c(s_i, \chi_i(s_i))$ with an averaging weight $A_i(\chi_i(s_i))$. The amplitude of the sound along the wavefront determines A_i. For example, if the wavefronts have spatial extent L and the sound is equally intense everywhere along L, then,

$$A_i(\chi_i) = \frac{1}{L} \quad .$$

Many tomographic schemes synthesize a map by minimizing a smoothed version of the second moment of the sound speed perturbation.[8,32] The data-data covariance matrix is required *a-priori*. To illustrate how this matrix is formed for eigentubes, we show the $i - j$th element,

$$\overline{\delta T_i \delta T_j} = \int_{\Gamma_i} \int_{\Gamma_j} \int_{w_i} \int_{w_j} ds_i ds_j d\chi_i d\chi_j \frac{A_i(\chi_i) A_j(\chi_j)}{c_0^2(s_i) c_0^2(s_j)} \overline{\delta c(s_i, \chi_i(s_i)) c(s_j, \chi_j(s_j))} \quad , \tag{3}$$

where the overline denotes expected value. When the size of an eigentube reduces to zero, as in the ray picture, this element reduces to the familiar two-dimensional integral used in previous formulations. Construction of the model-data covariance vector, also

19

required in this tomographic approach, is similar so is not shown here.

Although we now understand important features of this acoustic transmission, our understanding is incomplete. A better understanding of how sound interacts with the bottom on the Oahu slope would be interesting. Each eigenray is implicitly assumed to interact with the bottom over a distance of one kilometer since the bottom data are smoothed with a running low-pass filter having a one-kilometer scale. Eigentubes should be constructed for an ocean represented with small scales to better estimate the length over which sound interacts with the bottom. Another topic for future investigation is whether realistic interactions of sound within the bottom lead to significant changes in the delay of pulses compared to delays based on specular reflection.

Further investigation regarding the transition to ray chaos in the context of this experiment might place experimental limits upon which theories may be compared. It might be interesting to consider three-dimensional models for the propagation of sound to quantify the approximations made here with this two-dimensional model. A three-dimensional model is not required to explain arrivals A-E, but that does not mean that three- dimensional effects are insignificant.

Practical limits for computing travel times with rays have not yet been found in the ocean. Even when ray coordinates are chaotic, the coordinates and travel times of eigenray paths are stable and insensitive to fluctuations. It is convenient and fortuitous that much can be understood with the simplicity of rays, even when the Kaneohe source is mounted in relatively shallow water and sound propagates across 3709 km.

20

21

APPENDIX

The uncertainty in the algorithm for the speed of sound in seawater may be 0.05 $m \cdot s^{-1}$ r.m.s..[16] For simplicity, assume the error is uniform with depth. Then, the change in pulse delay over a distance R is,

$$\delta t \cong -\frac{R\delta c}{c^2} \ , \tag{4}$$

.[2] For $R = 3709$ km, $\delta c = 0.05 \times \sqrt{2} \cong 0.071$ $m \cdot s^{-1}$ (r.m.s. converted to amplitude with $\sqrt{2}$), $c = 1500 m \cdot s^{-1}$, $\delta t \cong -0.12$ s.

ZRAY can smooth the sound speed in the vertical in different ways and still enforce that the resulting curve pass through each data point.[6,7] Travel times change by about 0.07 s by varying the smoothing by plausible amounts.

Travel times in ZRAY are computed along a vertical slice passing through the geodesic. Sound might, however, reflect from nearby bathymetric features near the source. We have not examined nearby features on the Oahu slope. Instead, a hypo-

thetical case is considered where sound travels a distance and azimuthal angle r_1 and α respectively to a feature not on the geodesic, and then directly from this side object to the receiver over a distance r_2. The new distance of travel, $r_1 + r_2$, minus the distance on the geodesic, R, is obtained using the solution for oblique triangles. For $R = 3709$ km, $r_1 = 20$ km, $\alpha = 5°$, $R - (r_1 + r_2) = 0.077$ km, resulting in a travel time difference of 0.077 km/1.5km $\cdot$ s^{-1} $= 0.05$ s.

ZRAY, and our Levitus data base interpolater, interpolate the speed of sound linearly at each depth between neighboring vertical profiles of sound speed. Other interpolation schemes are possible such as quadratic and cubic splines. Typical differences in the speed of sound between neighboring stations in the CTD section are $\delta c \sim 2$ m $\cdot$ s^{-1} in the upper kilometer (Fig. 13). If different interpolation schemes modify the sound speed in-between stations by $\delta c/f$, where $f > 1$, then the change in travel time between stations separated by distance r is,

$$\delta t \cong -\frac{r\delta c/f}{c^2} \ .$$

For $f \sim 20$, $r = 70$ km (average spacing between CTD's), $\delta t = -0.003$ s. For fifty-six CTD stations where interpolation errors add with the same sign, the effect is about $55 \times 0.003 = 0.17$ s. If the sign of the interpolation errors are statistically independent between stations, the effect is about $\sqrt{55} \times 0.003 = 0.023$ s. The actual effect of interpolation probably lies in-between these estimates, say 0.1 s. Now since the rays spend about 1000 km in the upper kilometer where sound speed changes are larger, 0.1 s is reduced to one-third this value, 0.03 s, and we add 0.02 s for interpolation errors

23

below a kilometer. The order of magnitude estimate for interpolation error is taken to be 0.05 s.

We estimated that delays change by about 0.02 s for ray paths A-D by modifying the bottom depths by 2% of total depth near the source. The uncertainty in geodesic distance between the source and receiver is limited by the Global Positioning System survey. For a source and receiver uncertainty of 15 m and 20 m respectively, the geodesic could be in error by 35 m. The associated change in delay is 0.02 s.

The change in delay due to horizontal refraction is about 0.002 s along this section (Table I in Ref. 2). Clocks were maintained to an absolute accuracy of 0.002 s (Ref. 12).

Yet to be estimated is how much aliasing is contained in the CTD section. Aliased features in temperature lead to an uncertainty in the delays predicted with raytracing through this section.

References

[1]Spiesberger, J. L., T. G. Birdsall and K. Metzger, Acoustic thermometer, Office of Naval Res. Contract N00014-82-C-0019, 1983, available through the Woods Hole Oceanographic Institution, Woods Hole, MA. 02543.

[2]Spiesberger, J. L., K. Metzger and J. A. Furgerson, "Listening for climatic temperature change in the northeast Pacific: 1983- 1989," *J. Acoust. Soc. Am.*, 92, p. 384-396, (1992).

[3]Spiesberger, J.L., and K. Metzger, "Basin-scale monitoring with acoustic thermometers," *Oceanography*, 5(1), 1992, p. 92-98.

[4]Lichte, V. H., Über den Einflußhorizontaler Temperaturschichtung des Seewassers auf die Reichweite von Unterwasserschallsignalen. *Physikalische Zeitschrift, 17*, 1919, p. 385-389. English translation by A.F. Wittenborn, with a forward by R. J. Urick is available from Woods Hole Oceanographic Institution, Woods Hole, MA. 02543.

[5]Ewing, M. and J. L. Worzel, Propagation of sound in the ocean, III. *Mem. Geol. Soc. Am.*, *27*, 1948, p. 1-35.

[6]Spiesberger, J.L., E. Terray, and K. Prada, "Successful ray modeling of acoustic multipaths over a 3000-km section in the Pacific," J. Acoust. Soc. Am., 95, 3654-3657, (1994).

[7]J.B. Bowlin, J.L. Spiesberger, T.F. Duda, and L. Freitag, "Ocean acoustical ray-tracing software RAY," Woods Hole Oceanographic Tech. Rep., WHOI-93-10, 1993.

[8]Munk, W. and C. Wunsch, "Ocean acoustic tomography: A scheme for large scale monitoring," *Deep-Sea Res.*, *26*, p. 123- 161, (1979).

[9]Spiesberger, J.L. and K. Metzger, "Basin-scale tomography: A new tool for studying weather and climate," J. Geophys. Res., 96, 4869- 4889, (1991).

[10]Flatte, S.M. (ed.), R. Dashen, W.H. Munk, K.M. Watson, and F. Zachariasen, Sound Transmission through a Fluctuating Ocean, Cambridge University Press, pp. 299, (1979).

[11]T. Vincenty, "Direct and inverse solutions of geodesics on the ellipsoid with application of nested equations," *Survey Review*, 176, Vol. XXIII, p. 88-94, (1975).

[12]J.L. Spiesberger, P.J. Bushong, K. Metzger, and T.G. Birdsall, "Ocean acoustic tomography: estimating the acoustic travel time with phase," IEEE J. Ocean. Eng. **14**, 108-119 (1989).

[13]J.L. Spiesberger, P.J. Bushong, K. Metzger, and T.G. Birdsall, "Basin-scale tomography: synoptic measurements of a 4000 km length section in the Pacific," J. Phys. Oceanogr., **19**, 1073-1090 (1989).

[14]L.M. Brekhovskikh and Y. Lysanov, *Fundamentals of Ocean Acoustics*, (Springer-Verlag, New York, 1982).

[15]S. Levitus, *Climatological Atlas of the World Ocean*, NOAA Prof. Pap. 13 (U.S. government Printing Office, Washington, DC, 1982).

[16]V.A. Del Grosso, "New equation for the speed of sound in natural waters with comparisons to other equations," J. Acoust. Soc. Am., **56**, 1084-1091 (1974).

[17]A. Ben-Menahem and J. S. Sarva, *Seismic waves and sources*, 1108pp., (Springer-Verlag, New York, 1981).

[18]National Geophysical Data Center, ETOPO5, "5 minute gridded world elevations and bathymetry - a digital database," Boulder, CO 1987.

[19]J. Bowlin, "Generating eigenray tubes from two solutions of the wave equation," J. Acoust. Soc. Am., **89**, 2663-2669 (1991).

[20]Y.Q. Kang, "Low frequency temperature fluctuations in the upper 400 meters of the central north Pacific," Ph.D. thesis, Univ. of Hawaii, Honolulu, (1980).

[21]T.P. Barnett, "On the nature and causes of large-scale thermal variability in the central North Pacific," *J. Phys. Oceanogr.*, **11**, 887-904, (1981).

[22]J.L. Spiesberger and K. Metzger, "New estimates of sound-speed in water," J. Acoust. Soc. Am., 89, 1697-1700, (1991).

[23]J.L. Spiesberger and K. Metzger, "A new algorithm for sound speed in seawater," J. Acoust.. Soc. Am., **89**, 2677-2688, (1991).

[24]J.L. Spiesberger, "Is Del Grosso's sound-speed algorithm correct?" J. Acoust. Soc. Am., **93**, 2235-2237, (1993).

28

[25]B.D. Dushaw, P.F. Worcester, B.D. Cornuelle, and B.M. Howe, "On equations for the speed of sound in seawater," **93**, 255-275, (1993).

[26]F.J. Millero and X. Li, Comments on "On equations for the speed of sound in seawater," [J. Acoust. Soc. Am. 93, 255-275 (1993)][30], *J. Acoust. Soc. Am.*, **95**, 2757-2759, (1994).

[27]Palmer, D.R., Georges, T.M., and Jones, R.M., "Classical chaos and the sensitivity of the acoustic field to small-scale ocean structure," *Computer Physics Communications*, 65, 219-223, 1991.

[28]D.R. Palmer, M.G. Brown, F.D. Tappert, and H.F. Bezdek, "Classical chaos in non-separable wave propagation problems," *Geophys. Res. Letters,* **15**, 569-572, (1988).

[29]D.R. Palmer, T.M.Georges, and R.M. Jones, "Classical chaos and the sensitivity of the acoustic field to small-scale ocean structure," *Computer Physics Communications,* **65**, 219-223, (1991).

[30]F.D. Tappert, M.G. Brown, and G. Goni, "Weak chaos in an area-preserving mapping for sound ray propagation," *Physics Letters A*, **153**, 181-185, (1991).

[31]M.G. Brown, F.D.. Tappert, and G. Goni, "An investigation of sound ray dynamics

in the ocean volume using an area preserving mapping," *Wave Motion,* **14**, 93-99, (1991).

[32]B.D. Cornuelle, "Acoustic Tomography," *IEEE Trans. Geo. Rem. Sens.*, GE-20(3), 326-332, (1982).

Peak	# Turning Points	# Bottom Reflections
	157	2
A	158	3, 4
	159	3, 4
	160	5
	160	2
B	161	2, 4
	162	3
	161	1
C	163	2
	164	3
	163	1
D	164	3
	165	2
E	166	1

Table I. The geometry of rays A through E computed with rays traced through climatological conditions given by Levitus during the Spring.[15]

| Peak | Travel Times | | $T_1 - T_0$ |
	T_1 (s)	T_0 (s)	(s)
A	2503.99	2503.75	+0.24
B	2504.32	2504.09	+0.23
C	2504.82	2504.41	+0.41
D	2505.03	2504.68	+0.35

Table II. The measured (T_1) and predicted (T_0) travel times of peaks A through D. The measured travel times are for the first week in May 1988. The predicted travel times are from rays traced through the sound speed field synthesized with the CTD section (Fig. 13) and Del Grosso's algorithm for the speed of sound.[16] Measured travel times account for the delay of 0.065 s through the narrowband Kaneohe source.

Cause of Travel Time Difference	Travel Time (s)
Ocean changes temperature between May and July 1988	0.2
Uncertainty in sound speed algorithm	0.12
Interpolating sound speed in vertical	0.07
Interpolating sound speed in horizontal	0.05
3-D reflections	0.05
Position error of source and receiver	0.02
Errors in bottom depth for specular reflections	0.02
Horizontal refraction	0.002
Clock errors	0.002
Aliasing From CTD Survey	?
Sound penetrating bottom near source	?
Sum of above	0.53 + ?

Table III. Possible causes for differences between measured and predicted travel times given in Table II. See Appendix for details.

FIG. 1. Plan view of the Kaneohe source experiment. The Kaneohe source is located about five miles north of Kaneohe Bay, Oahu. The receiver near the coast of northern California, is one of many U.S. Navy SOSUS stations used to receive these transmissions. Circles indicate the positions of fifty-six stations where conductivity, temperature, and depth were measured with a CTD in July 1988 by the Naval Oceanographic Office.

FIG. 2. Changes in acoustic travel time (left-hand scale) measured along the section in Fig. 1 for the indicated months. Changes in travel time are reckoned to the first delay measured in Nov. 1983. The right-hand axis indicates, within 10%, how much the spatially averaged temperature needs to change in the upper kilometer to give the indicated changes in travel time.

FIG. 3. The daily incoherent average of acoustic multipaths for four days in 1983 and one day in 1987. The vertical dashed lines join together acoustic arrivals which are similar. The vertical axis is amplitude. The travel time in November 1983 is obtained by adding 2500 s to the arrival times shown. Daily averages have been shifted by a constant arrival time to line up peaks A through E with the record on 29 November 1983. Adapted from Ref. 2.

FIG. 4. The black streaks indicate the arrival times of stable acoustic pulses A-E whose travel times can be measured throughout the experiment at the SOSUS station in the indicated months in 1987-89. Travel times are 2500 s greater than the displayed arrival times. The signal processing required to produce this plot is described in Figs.

34

FIG. 5. Vertical profiles of sound speed between the Kaneohe source, at 0 km, and the receiver, at 3709 km. The surface speed of each profile is plotted at the range of its station. A change of 50 m s^{-1} is indicated by the floating scale. Sound speeds are computed from temperature, salinity, and depth according to Levitus's climatology for Spring[15] and Del Grosso's algorithm for the speed of sound.[16] Only the upper four ·kilometers are shown.

FIG. 6. The incoherent average of acoustic multipaths on 29 Nov 1983 (solid) compared with a prediction from ray theory (dashed). The ray trace is computed with Levitus' climatology for Summer.[15] Travel times of the ray trace are shifted to highlight the correspondence of arrivals A through E in the data and prediction. The left-hand axis gives the received level in dB referenced to a pressure of 1 μPa, as predicted with ray theory. The right-hand axis refers to the data plotted on an amplitude scale. Travel time in November 1983 is obtained by adding 2500 s to the arrival times shown.

FIG. 7. Comparison of raytrace for summer (solid) with raytraces for Spring, Fall, and Winter (dashed). The raytrace for summer is identical to that in Fig. 6. Parameters used for each raytrace are identical. The seasonal fields are obtained from Levitus's climatological values of temperature and salinity.[15] Travel times for the summer raytrace are 2500 s greater than the indicated arrival times. To show the best correspondence between arrivals A-E, travel times for Spring and Fall raytraces are

35

increased by 0.01 and 0.04 s respectively and the travel times for the Winter raytrace are decreased by 0.05 s.

FIG. 8. *Left*: Received level (dB re 1 μPa) of geometric and non-geometric rays versus their arrival time. Rays are traced using Levitus's[15] summertime conditions. *Right*: Depths of same geometric and non-geometric eigenrays at the receiver versus their arrival time. When plotted depths are less than the receiver depth of 1433 m, the eigenrays are non-geometric and the depth of the caustic above the receiver is indicated. Travel times are obtained by adding 2500 s to the arrival times.

FIG. 9. The upper and lower turning depths of rays A through E at four locations along the acoustic section. Depths are taken from the ray traces computed with Levitus' climatology for Spring.[15]

FIG. 10. The upper turning depths of rays A-E at about 1500 km from the Kaneohe source for the indicated seasons and for the July 1988 CTD survey. Each arrival, A-E, consists of a group of eigenrays. The integer gives the number of eigenrays within 10 dB of the most energetic in each group. The mean, standard deviation, and extreme upper turning depths for each group are indicated by the symbols *, o, and - respectively.

FIG. 11. Rays A-E and bathymetry and blowups near the source and the receiver.

FIG. 12. The travel times of peaks A through E computed for the indicated Levitus[15] seasons and the CTD cruise in July 1988. Levitus's Spring is an historical average of data from May, June, and July.

36

FIG. 13. Sound speeds computed from the July 1988 CTD cruise minus sound speeds computed from Levitus climatology for Spring.[15] Negative values indicate the CTD section is colder and slower than the Levitus data. Contours intervals are $2 \text{ m} \cdot \text{s}^{-1}$ and $0.2 \text{ m} \cdot \text{s}^{-1}$ in the upper and lower panels respectively.

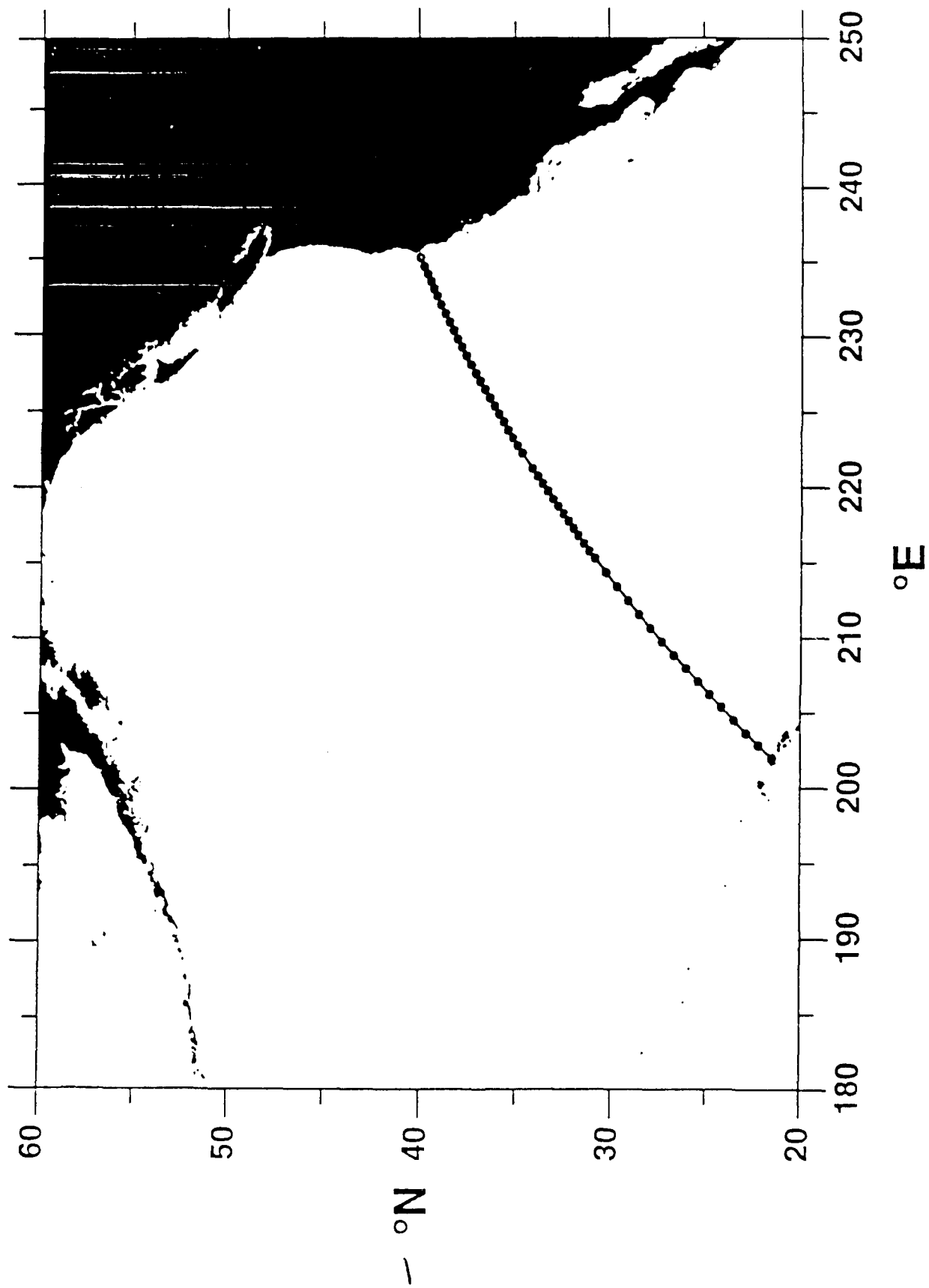FIG. 14. Same as Fig. 13 except this is a blowup of the seasonal thermocline. Contour interval is $2 \text{ m} \cdot \text{s}^{-1}$.

FIG. 15. Comparison of raytrace for summer (solid) with the raytrace for the July 1988 CTD section. Travel times are 2500 s greater than the arrival times shown.

FIG. 16. Sensitivity of the ray path A to small perturbations in launch angle. The figure shows the result of attempting to trace the same eigenray from the source to the receiver (solid) and from the receiver to the source (dashed). The angle of the ray for the reverse ray trace is taken to be equal to the angle of the ray from the forward ray trace at the receiver. Ray coordinates appear identical except for the reverse raytrace following the bottom reflection. Angles of rays are specified to fifteen significant digits.
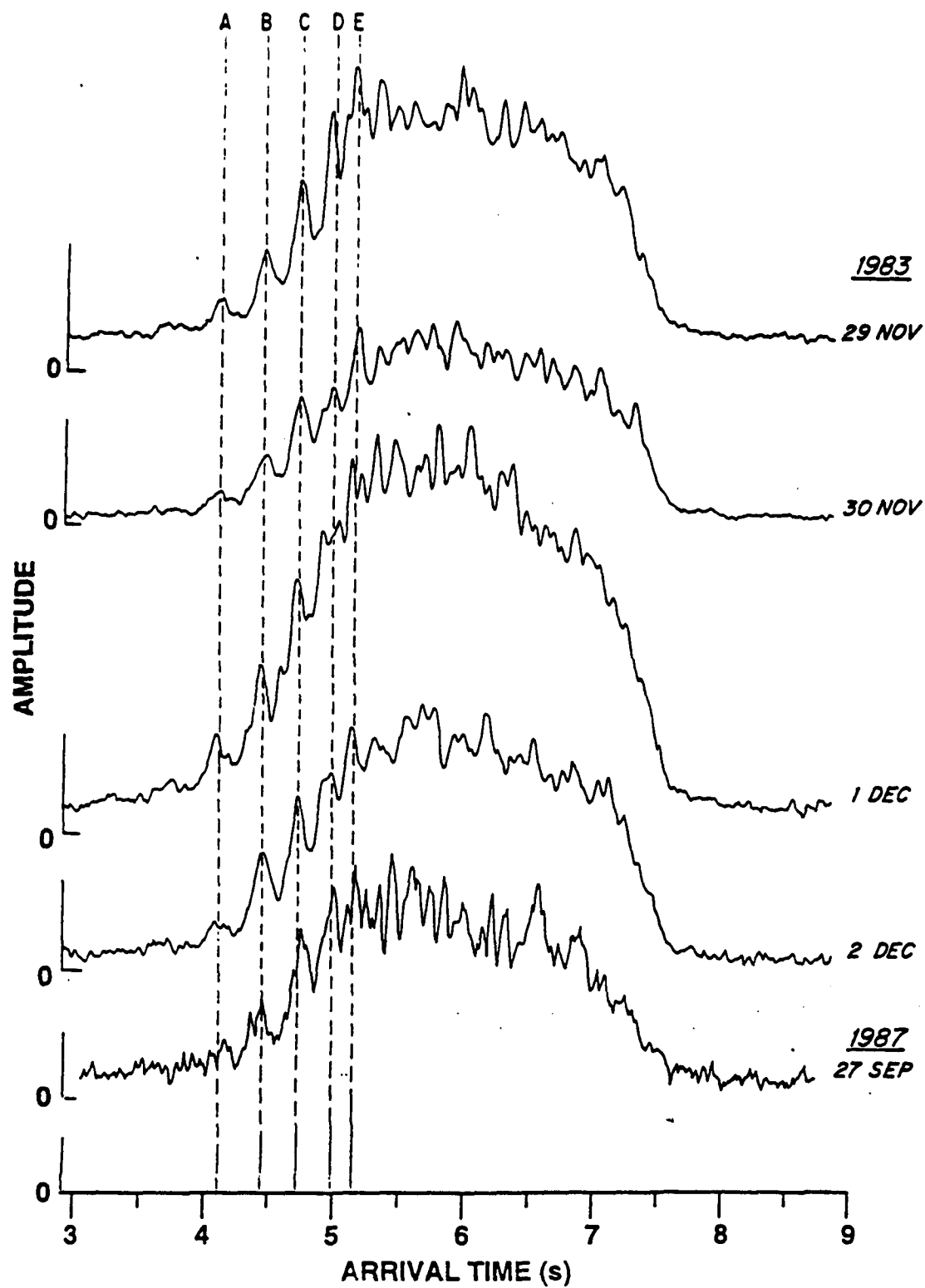
FIG. 17. Ray depths at the range of the acoustic receiver versus their travel time at the range of the acoustic receiver for the indicated cases.
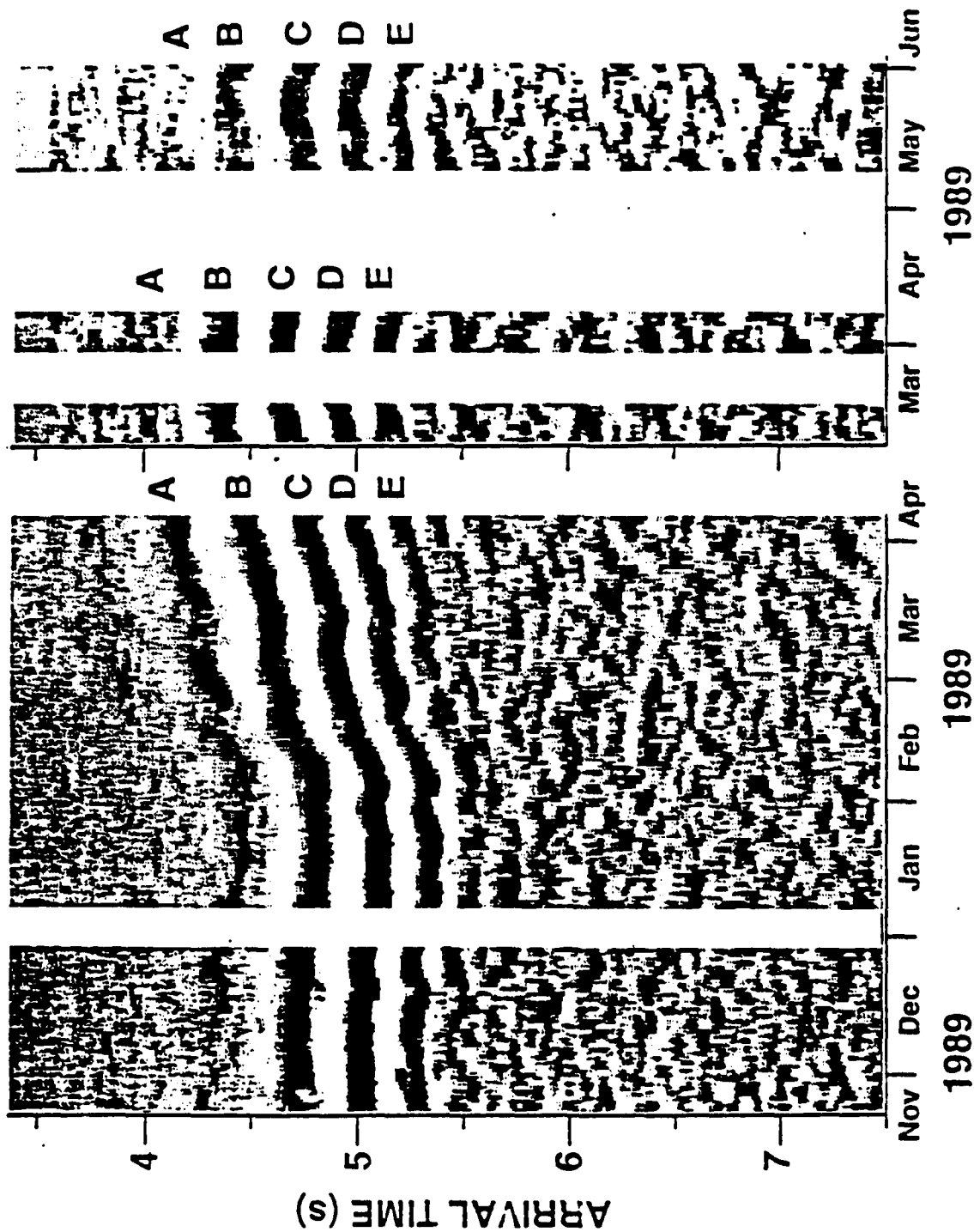
The receiver is at 1433 m depth. The left hand column is the result of shooting 38,561 rays from the source between the inclination angles of $-8.2°$ and $40°$. Only rays with less than ten bottom reflections are shown. The right-hand column is a blow up in arrival time of the panels on the left to show the data near the stable multipath

37

arrivals A-E as indicated in Figs. 7 and 15. The approximate arrival times of A-E are indicated in the right column. Travel times are 2500 s greater than the arrival times shown.
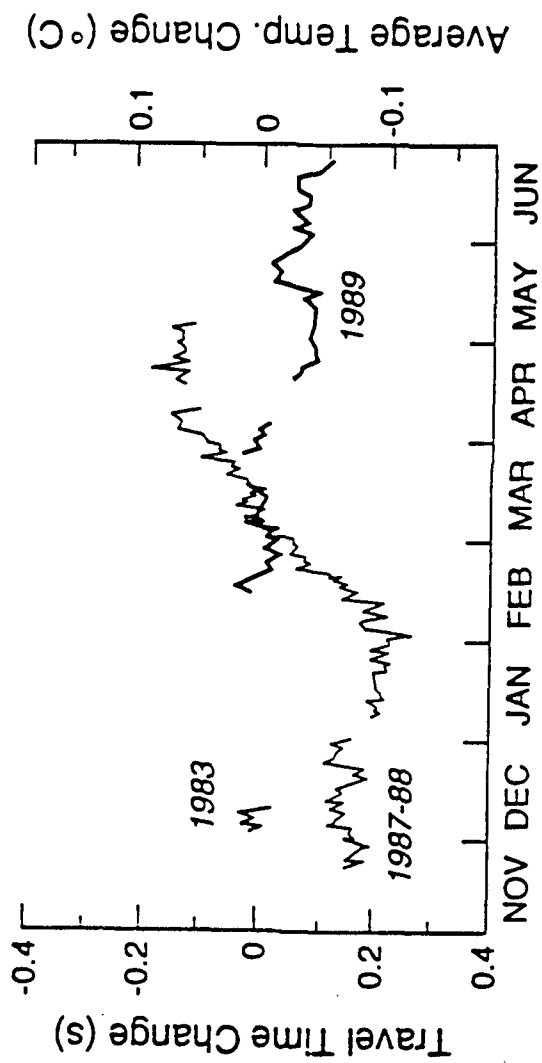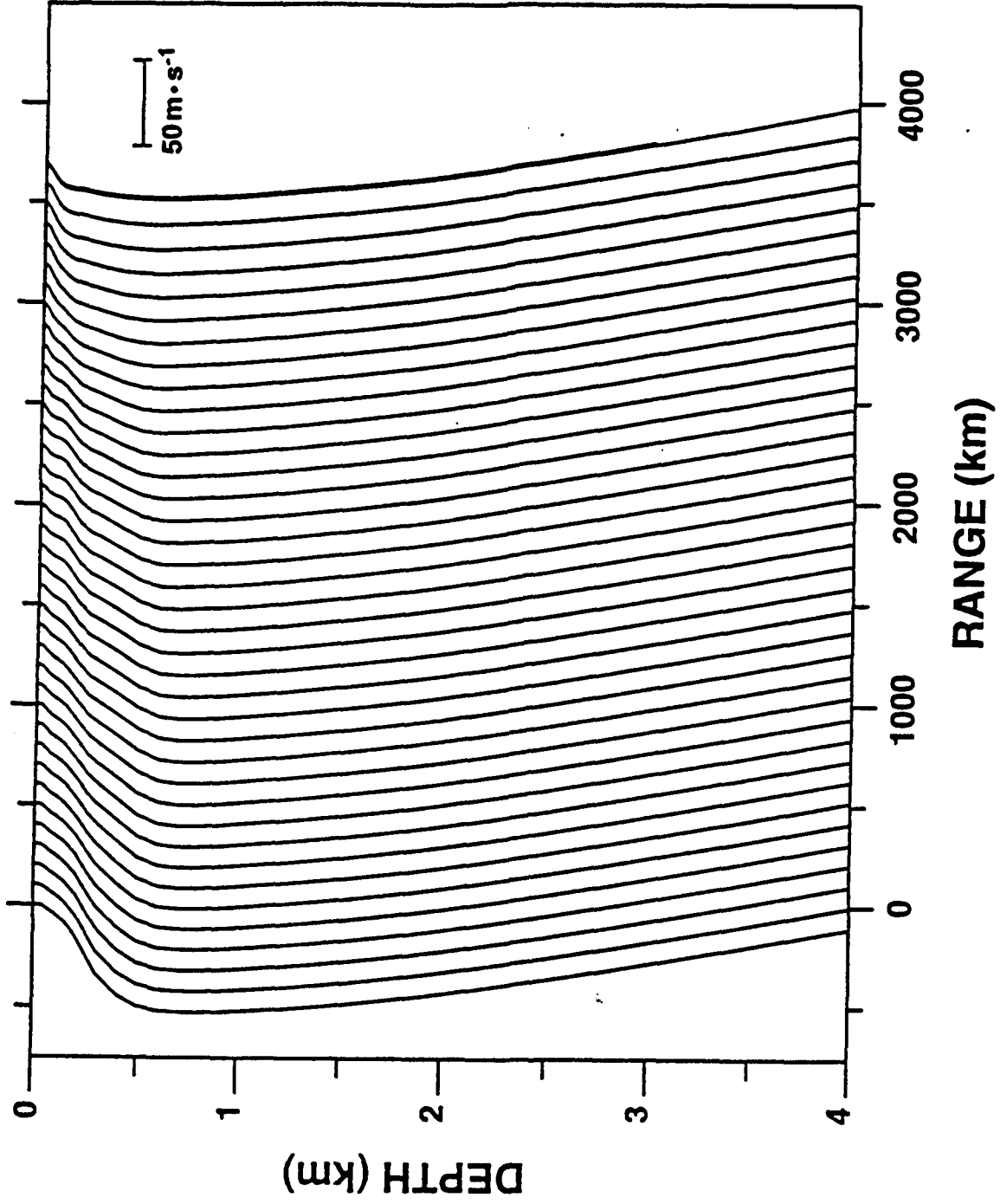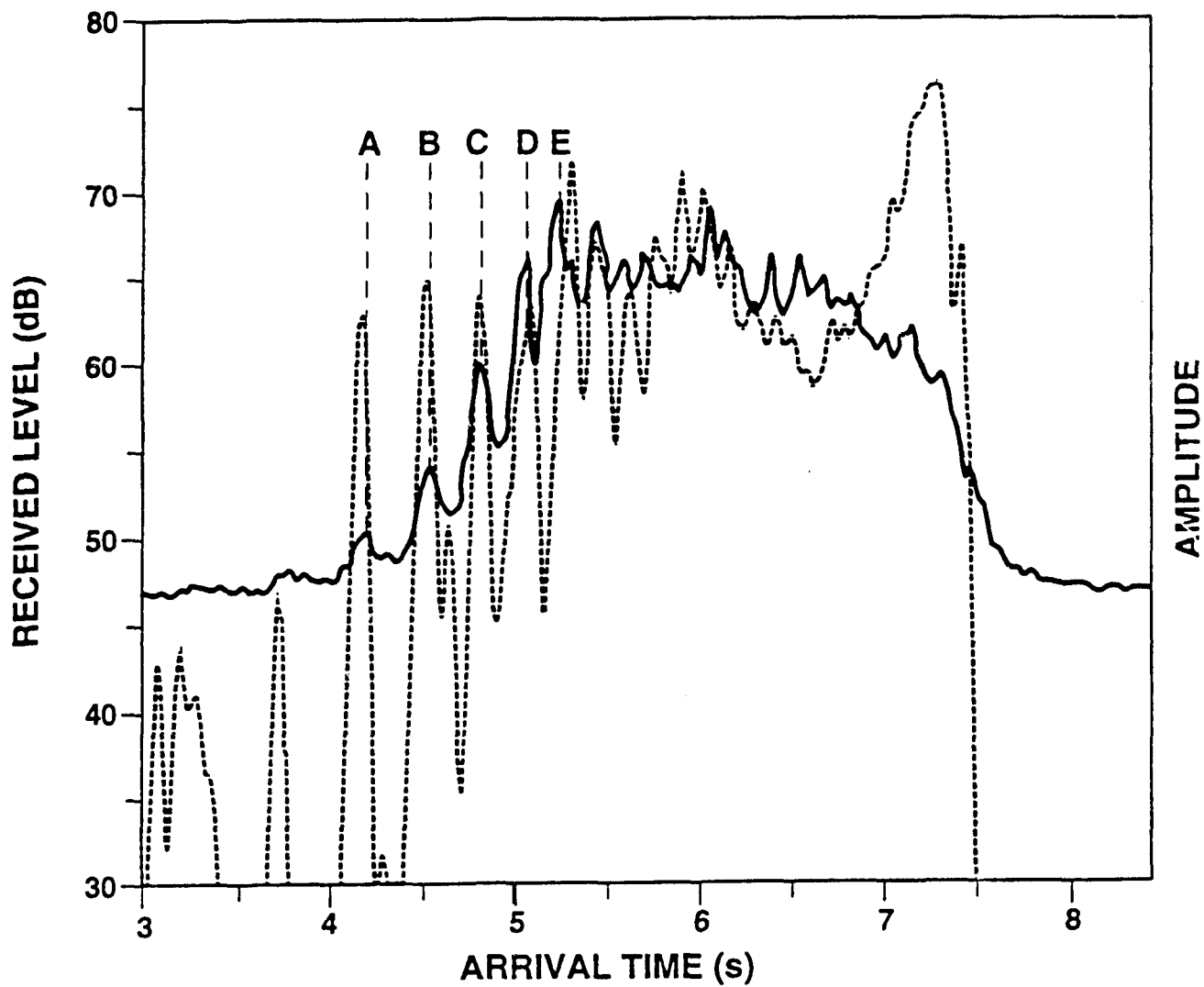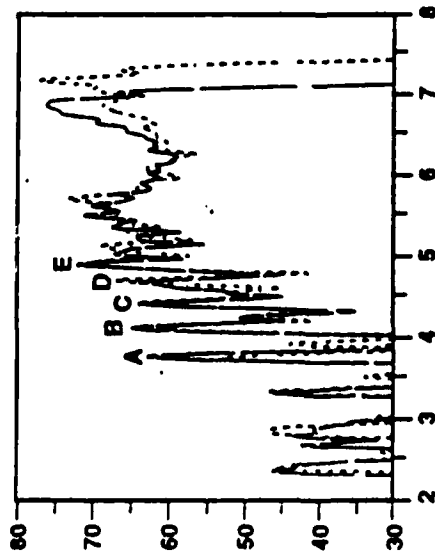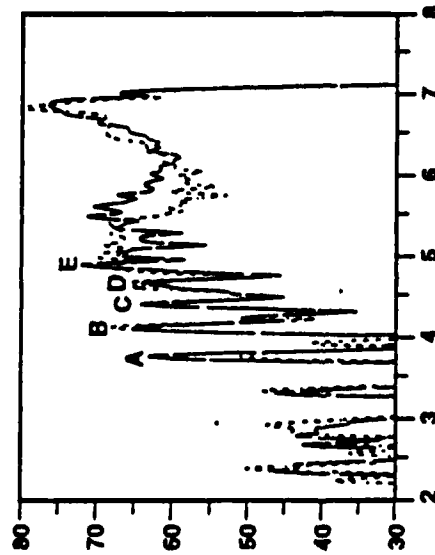
Average Temp. Change (°C)

Travel Time Change (s)

NOV DEC JAN FEB MAR APR MAY JUN

1983

1987-88

1989

3

ARRIVAL TIME (s)

A
B
C
D
E

Nov Dec Jan Feb Mar Apr May Jun
1989 1989 1989

4

SOUND SPEEDS

DEPTH (km)

RANGE (km)

50 m·s⁻¹

WINTER FALL SPRING

ARRIVAL TIME (s)

RECEIVED LEVEL (dB)

7

ARRIVAL TIME (s)

DEPTH OF RAY (m)

RECEIVED LEVEL (dB)

56

UPPER

LOWER

DEPTH (m)

RANGE (km)

LJS-408-03-md

UPPER TURNING DEPTH (m)

SUMMER   FALL   WINTER   SPRING   JUL
CTD

200   300   400

A   B   C   D   E

10

RAY A / RAY B / RAY C / RAY D / RAY E — NEAR SOURCE, NEAR RECEIVER depth (km) vs. RANGE (km) ray-path plots.

13
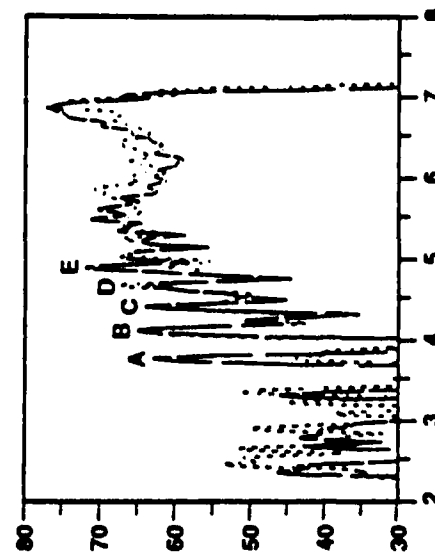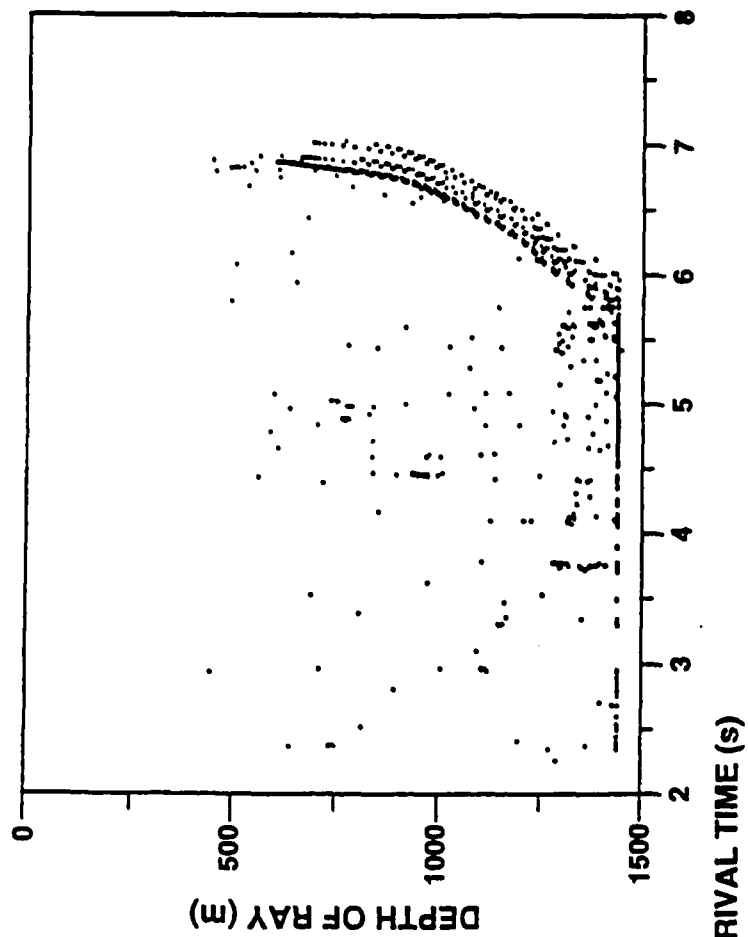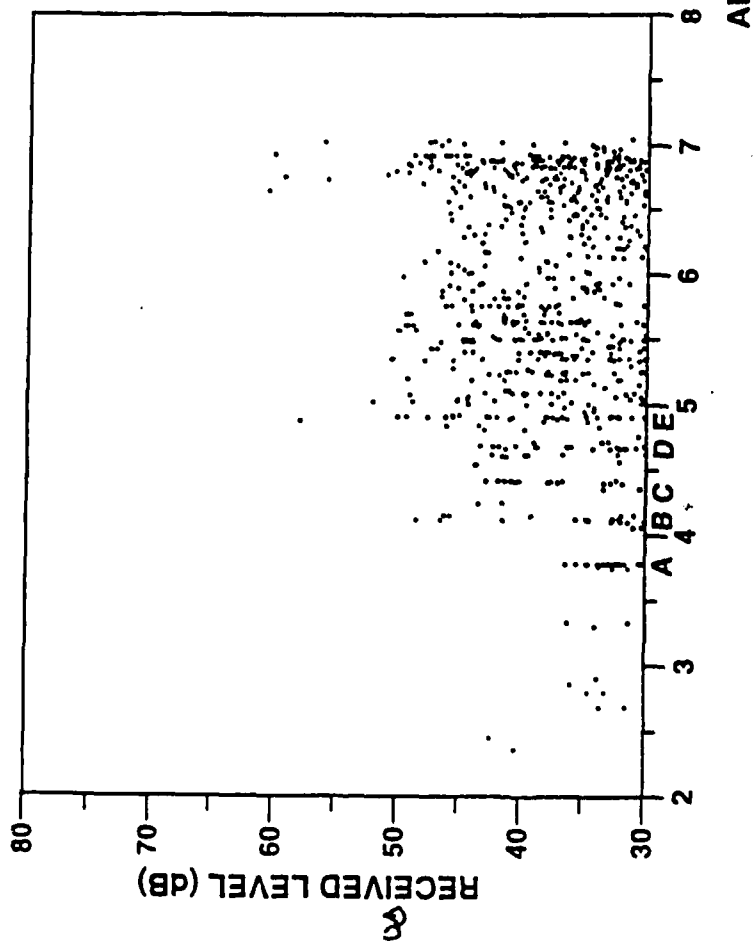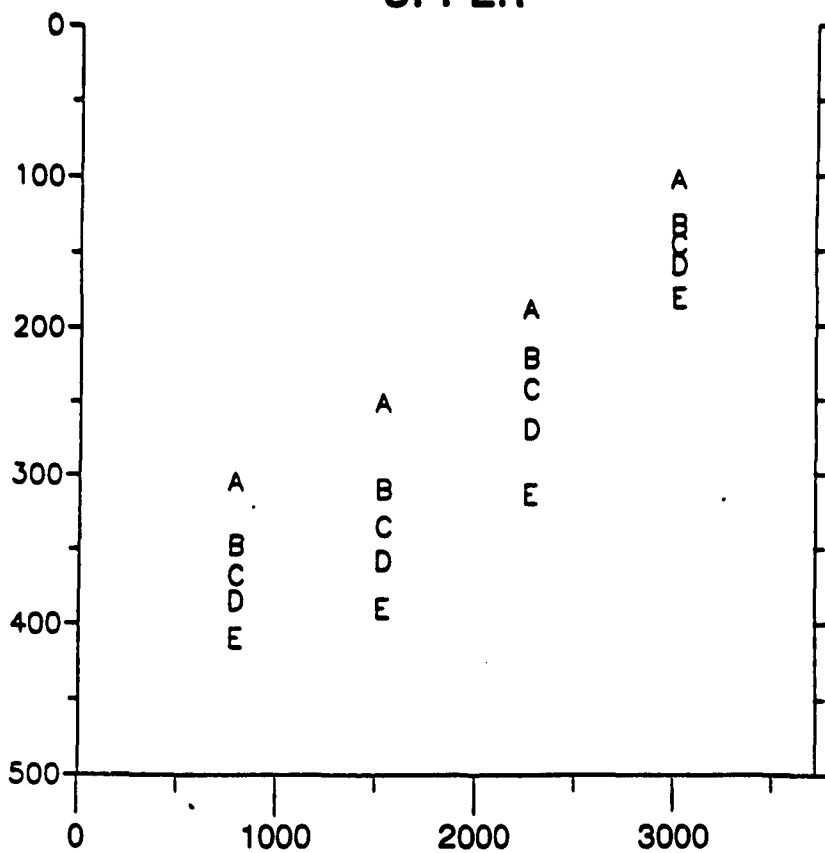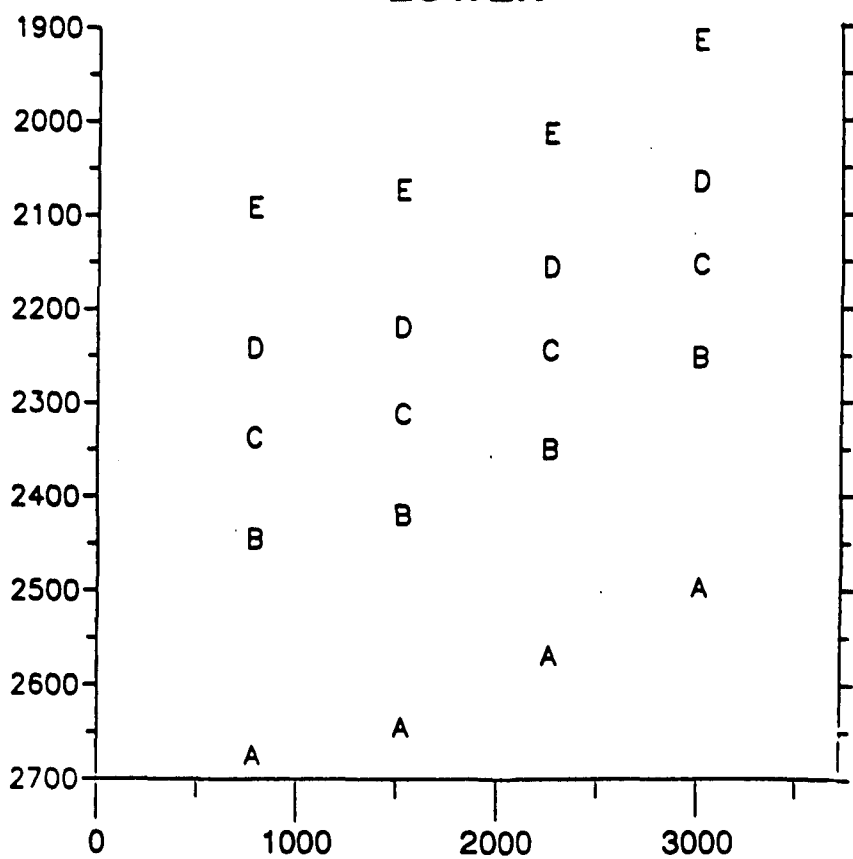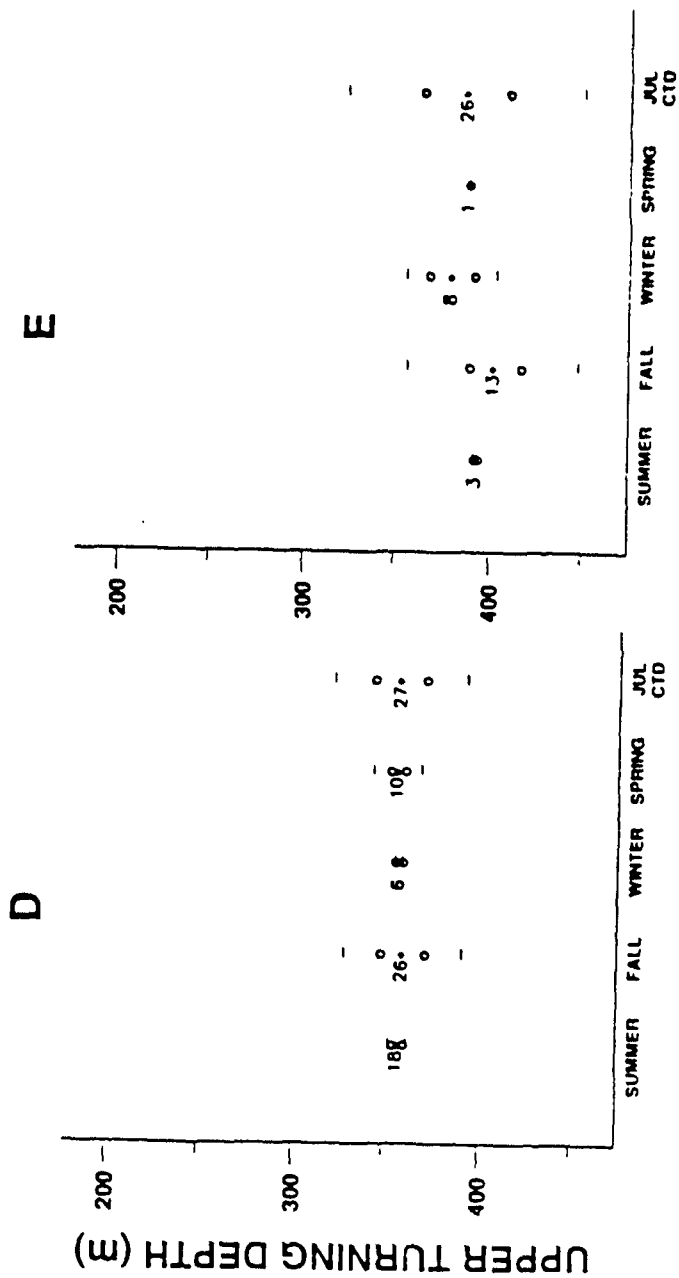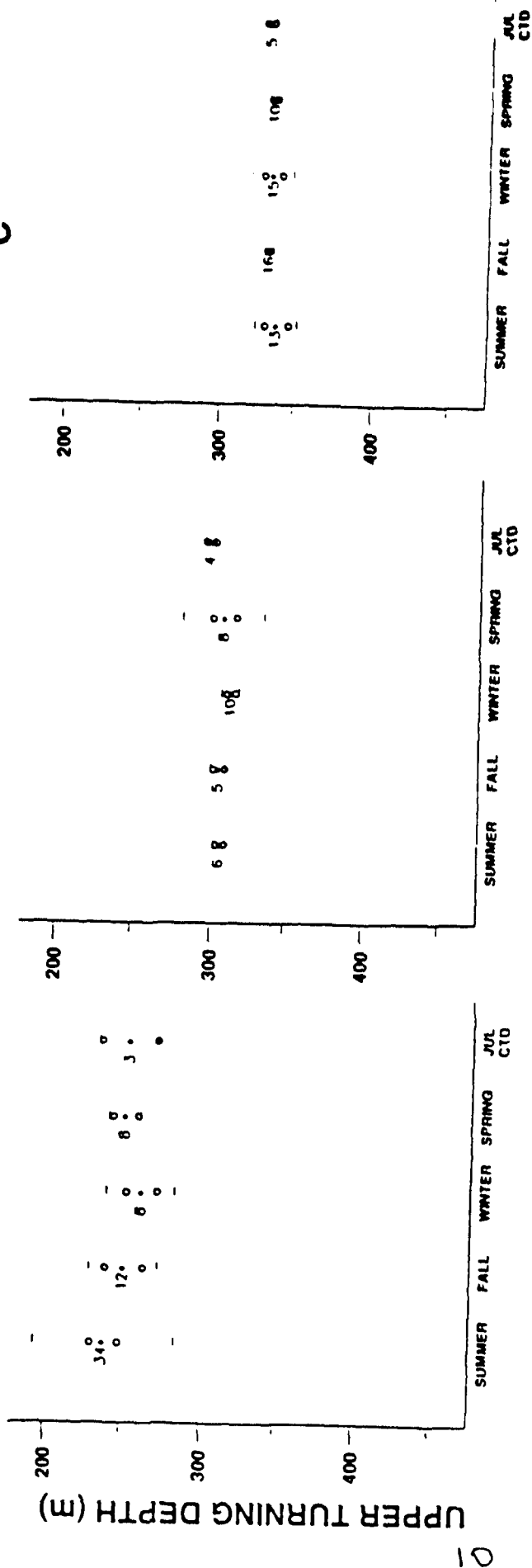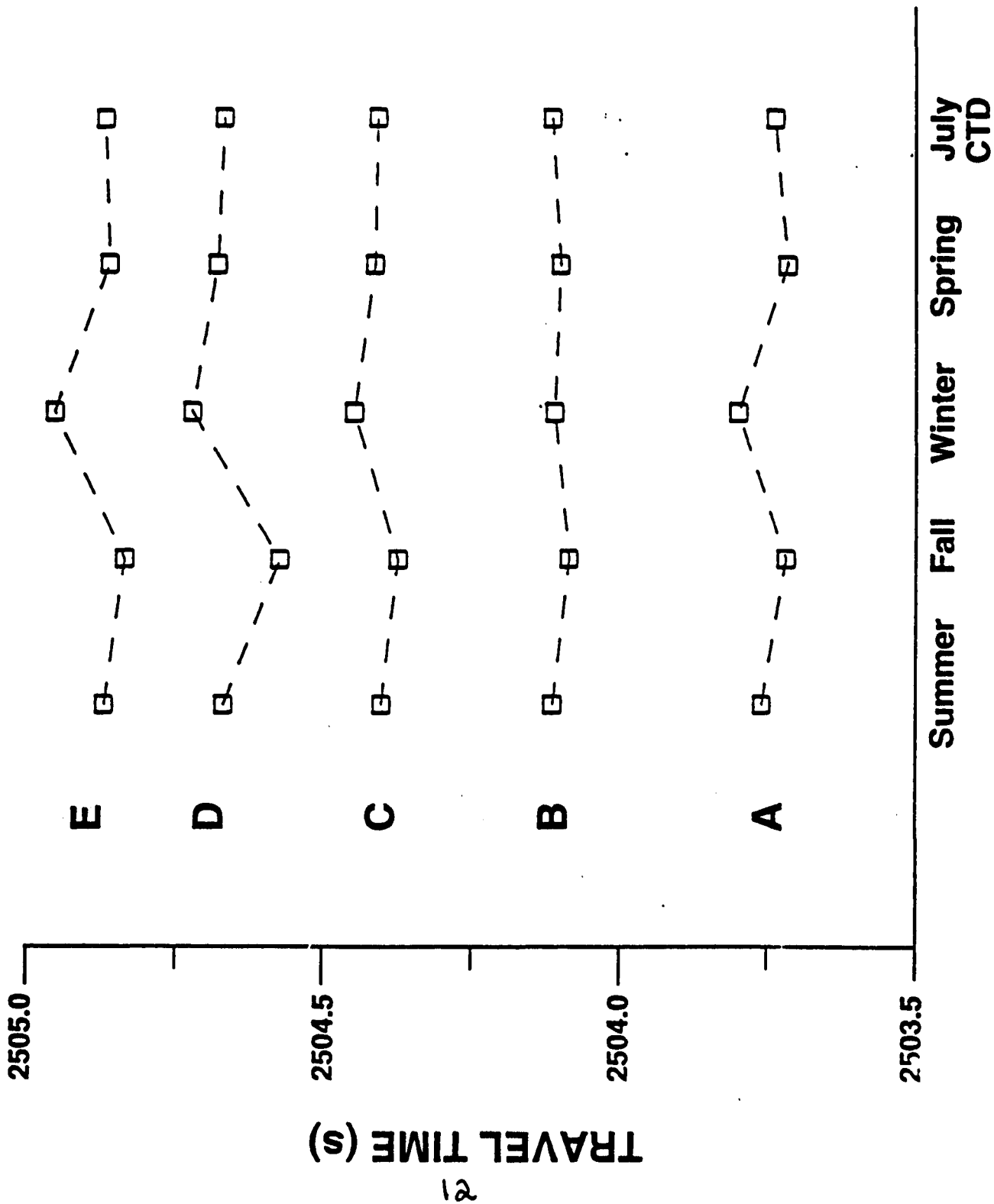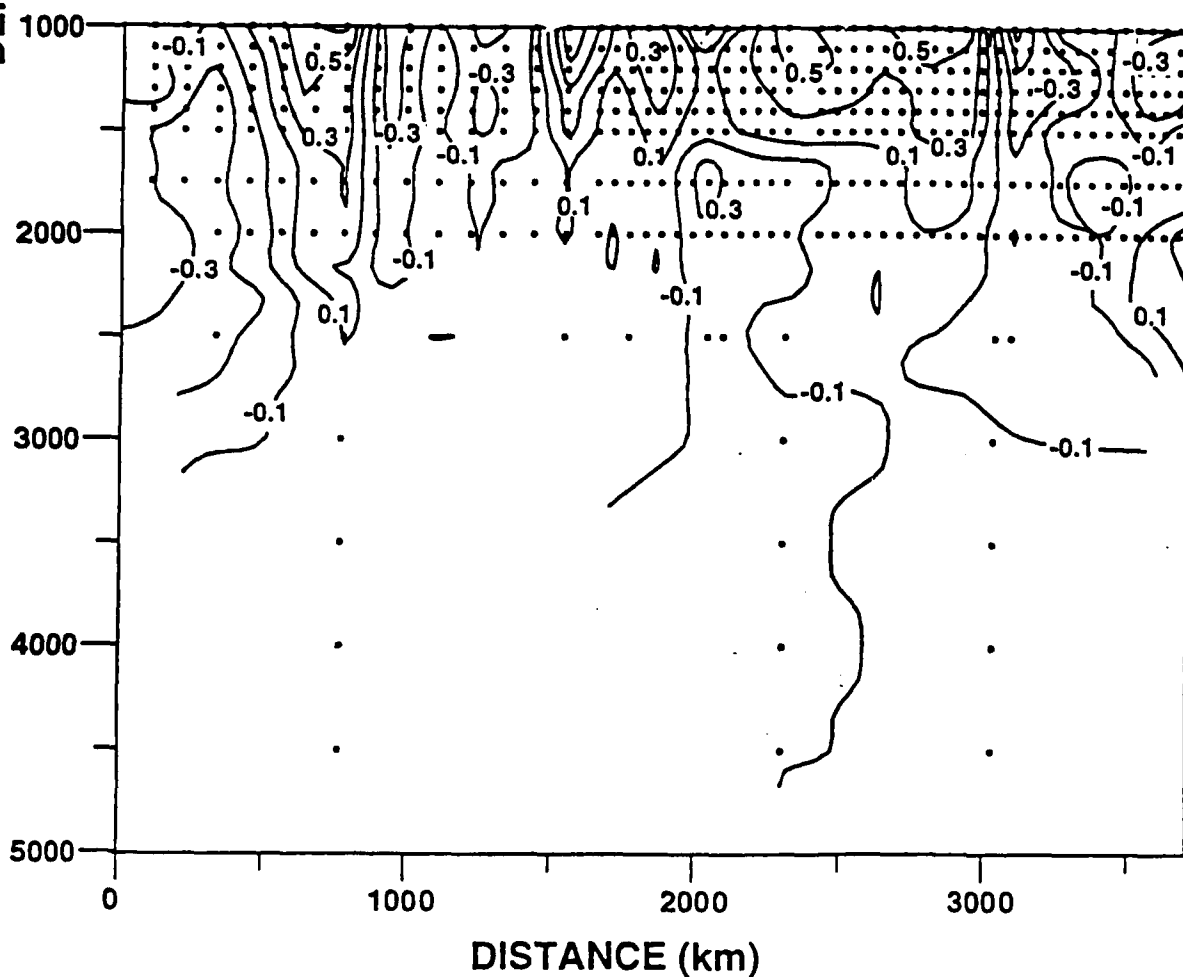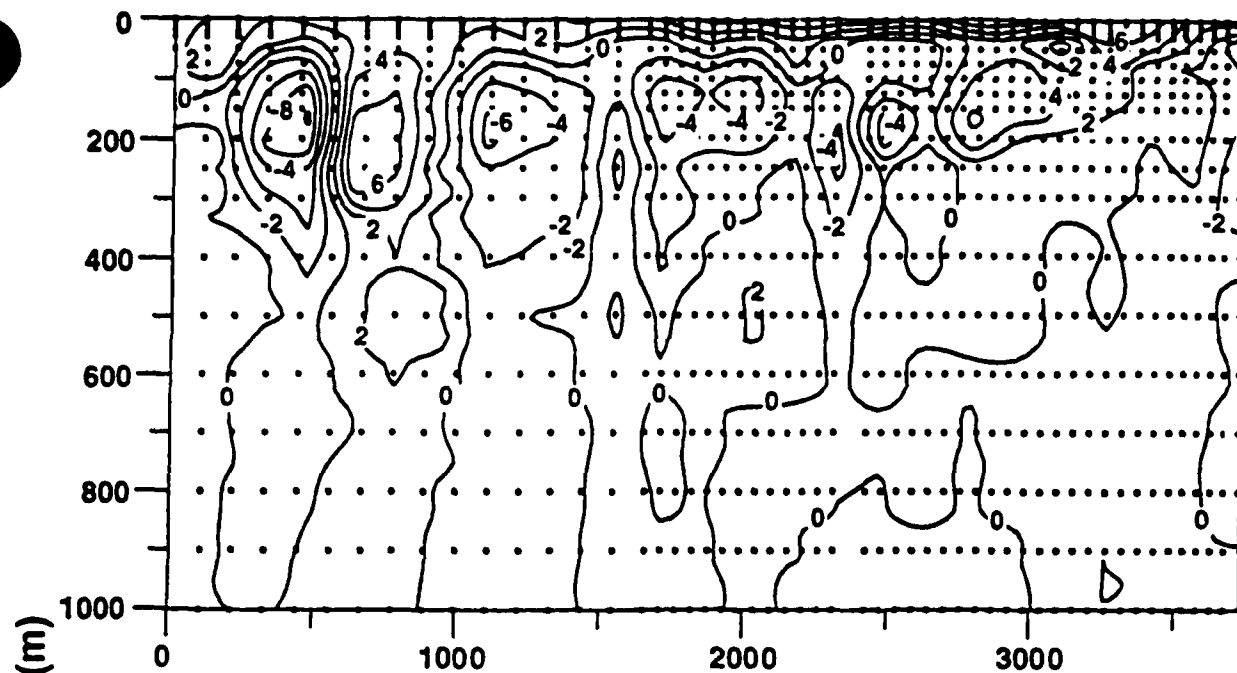
SEASONAL THERMOCLINE

15

RAY A

DEPTH (km)

DISTANCE (km)

16

LEVITUS SPRING

LEVITUS SUMMER

CTD JULY 1988

17
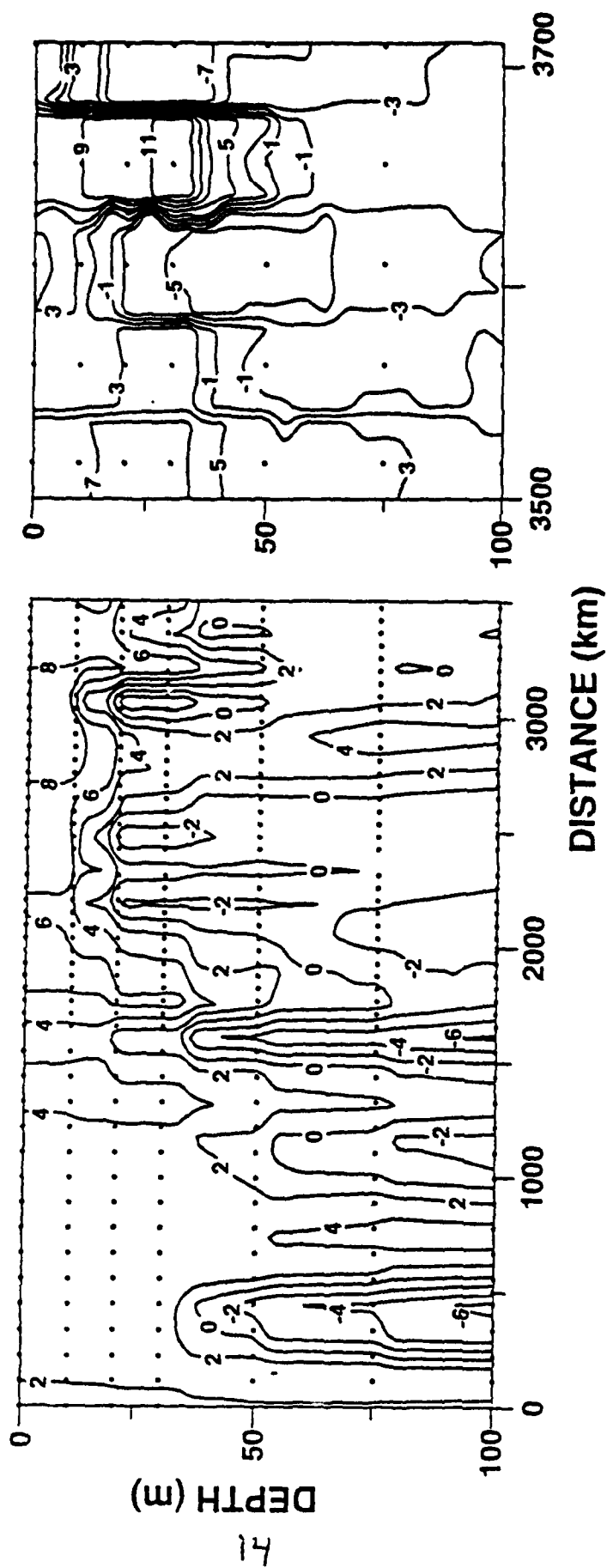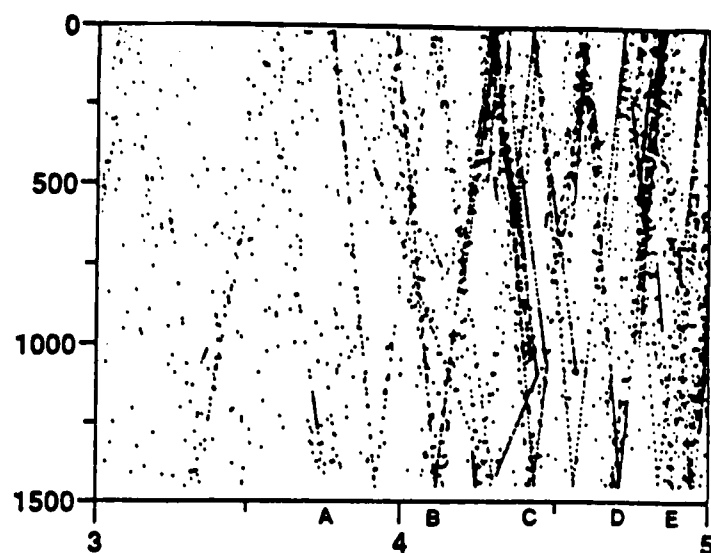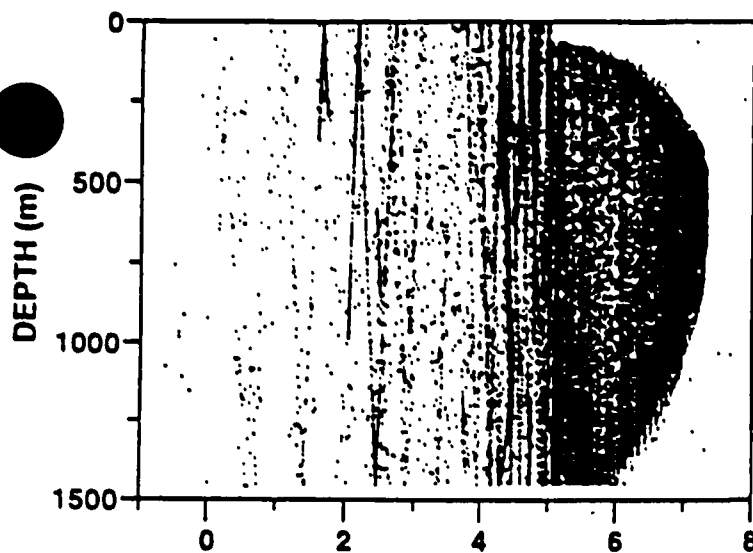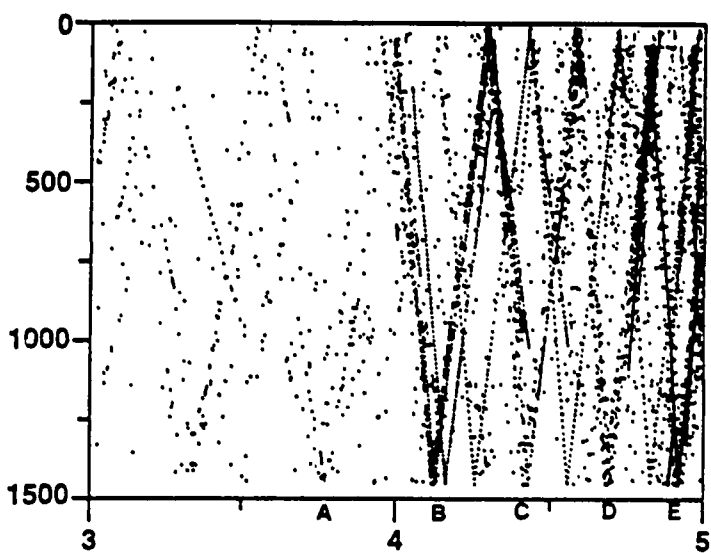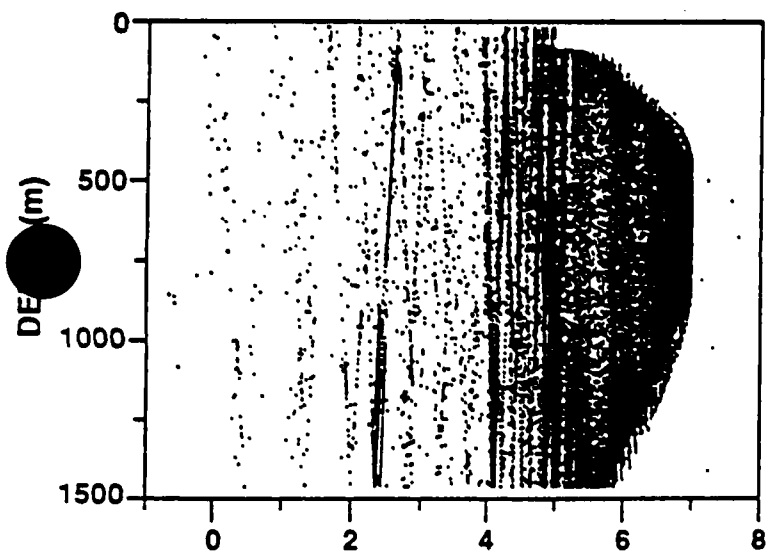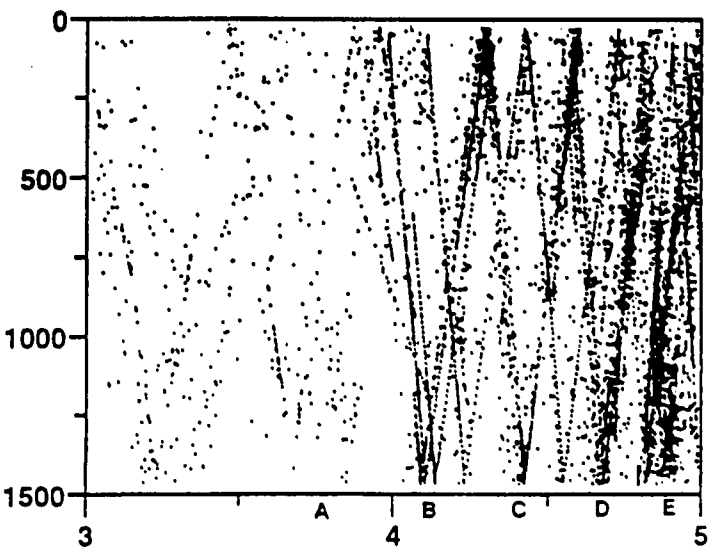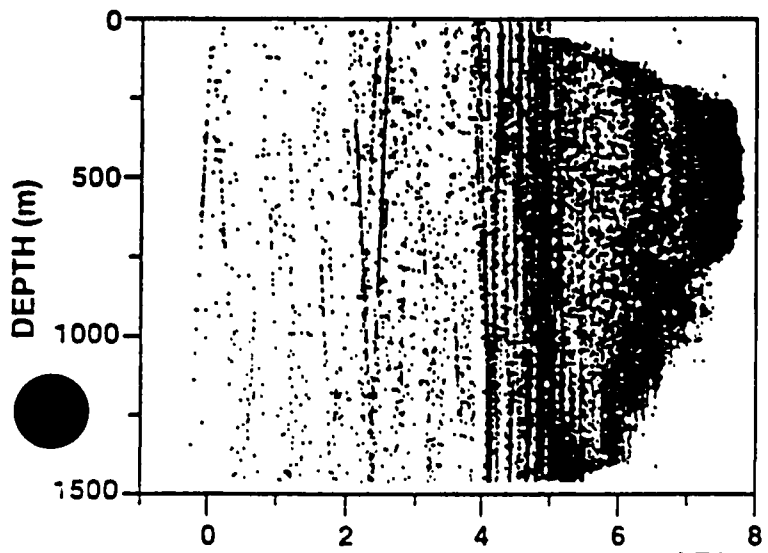
GAMOT QUARTERLY REPORT
THIRD QUARTER 1994

FLORIDA STATE UNIVERSITY
PROFESSOR JAMES J. O'BRIEN

Summary

The FSU Tasks and Deliverables are on schedule.

As part of our contribution to Task B6, we have designed an acoustic tomography assimilation scheme for a reduced-gravity model, but with spatially variable density. An optimal control method is used to assimilate tomographic data into an ocean model with the goal of estimating the time independent density field in the upper northeast Pacific ocean. Coding has been completed on the full model, compilation errors have been removed and preliminary testing has been successful. The implementation is primarily being done by graduate student Mr. Ming Liu.

Task B6

The reduced gravity model of the northeast Pacific (NEP) has been described in our previous reports. For this next stage of research, we shall investigate horizontal variations in t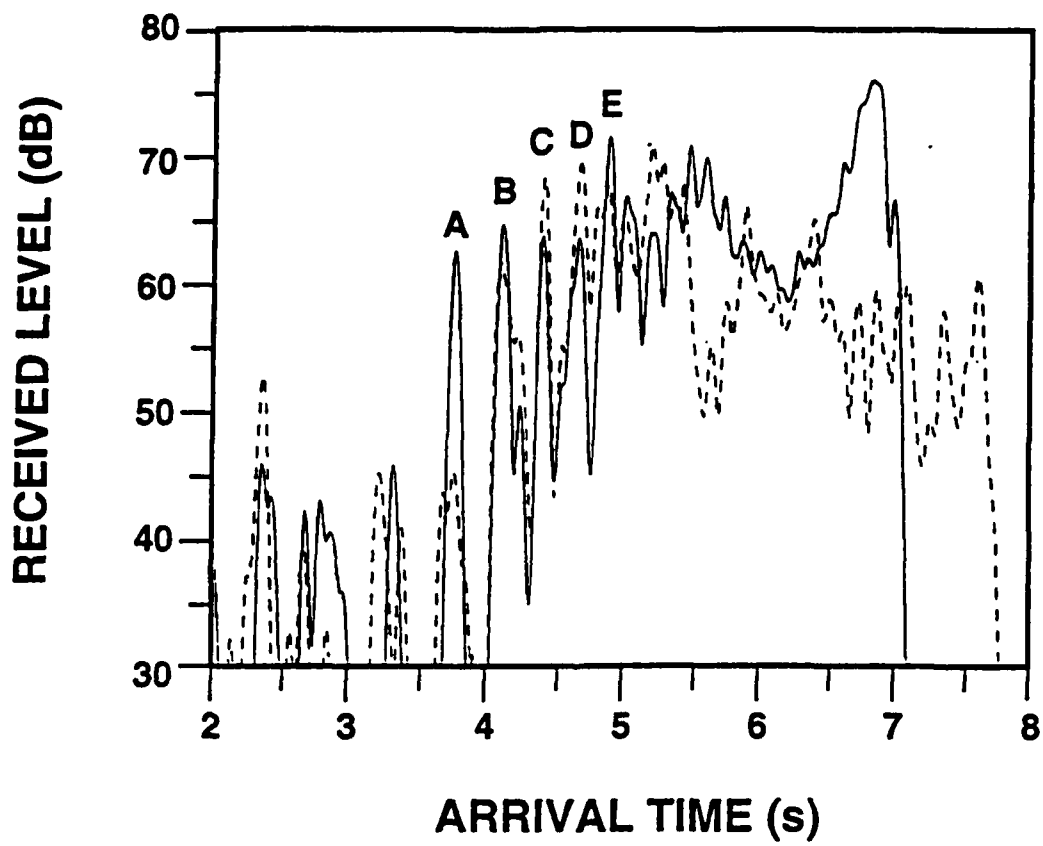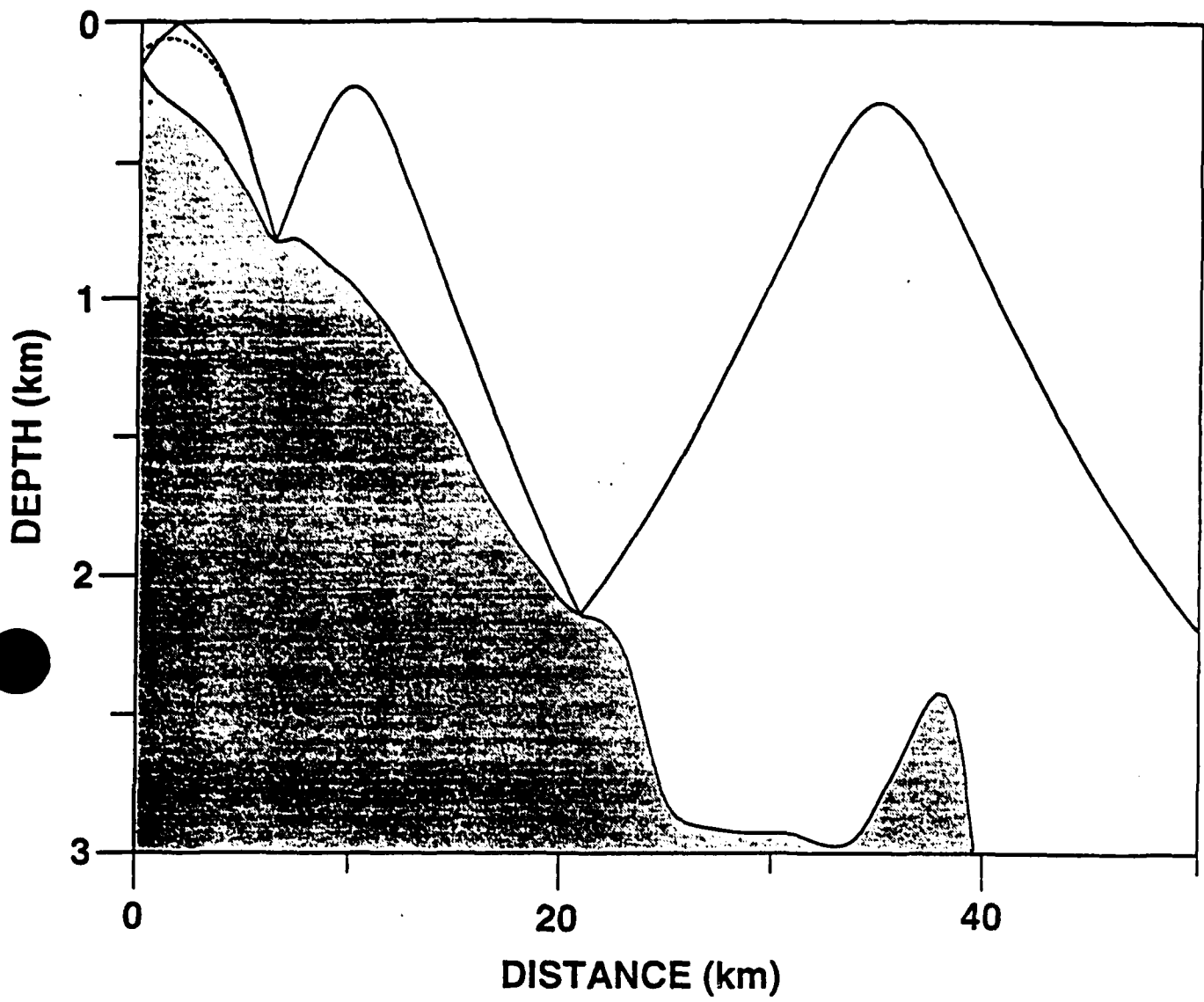he upper layer density $\rho = \rho(\phi, \theta)$ which can be estimated through assimilation of tomographic data using the variational adjoint method. The current goal is to reveal the thermohaline structure not included in the reduced-gravity models. The technical details of the optimal control method were thoroughly documented in the previous report.

The assimilation model is being run as an identical twin experiment. Levitus density data is incorporated into the model, as described previously. Acoustic travel time estimates are then made over various paths (Fig. 1) for the model with the Levitus density field. The density field (Fig. 2) is perturbed (Fig. 3) and the tomographic information is assimilated into the model with the intent of recovering the correct density field.

The iteration procedure (previous report) converges rapidly, requiring about 10 iterations to recover the correct density field. This is indicated by the rapid reduction in the cost function shown in Fig. 4.
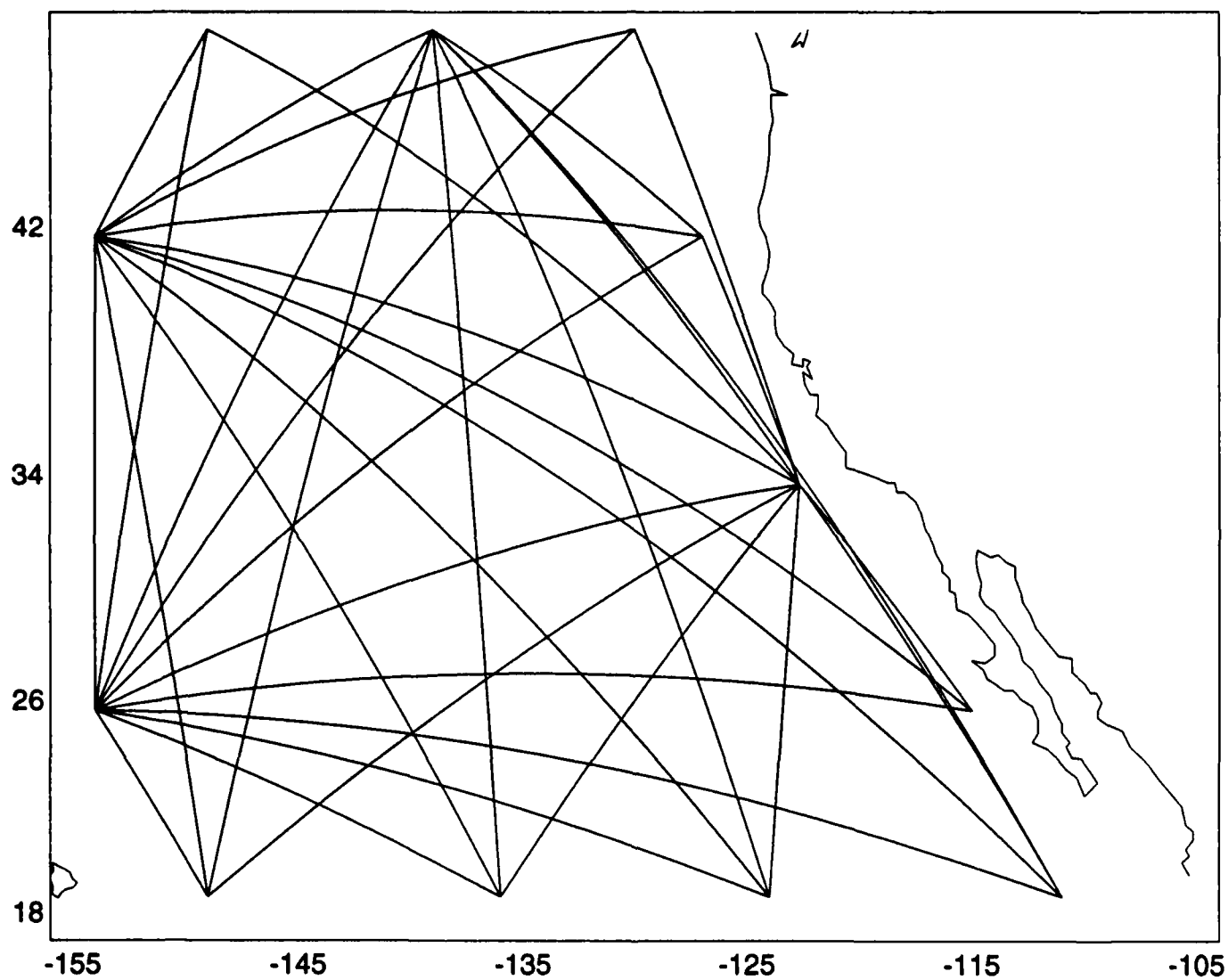
Figure 1: The tomographic paths used in the model.
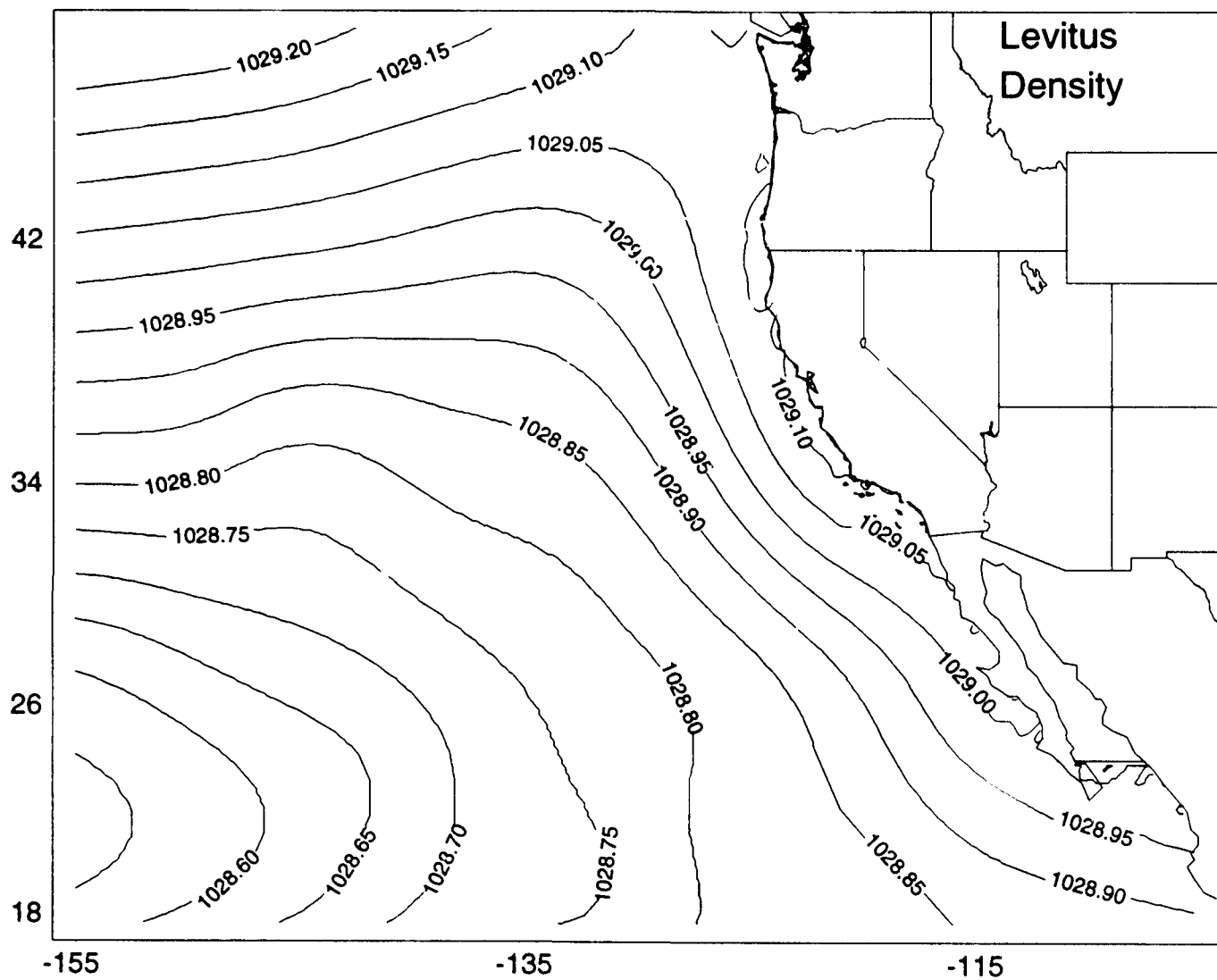
Figure 2: The mean Levitus density field.
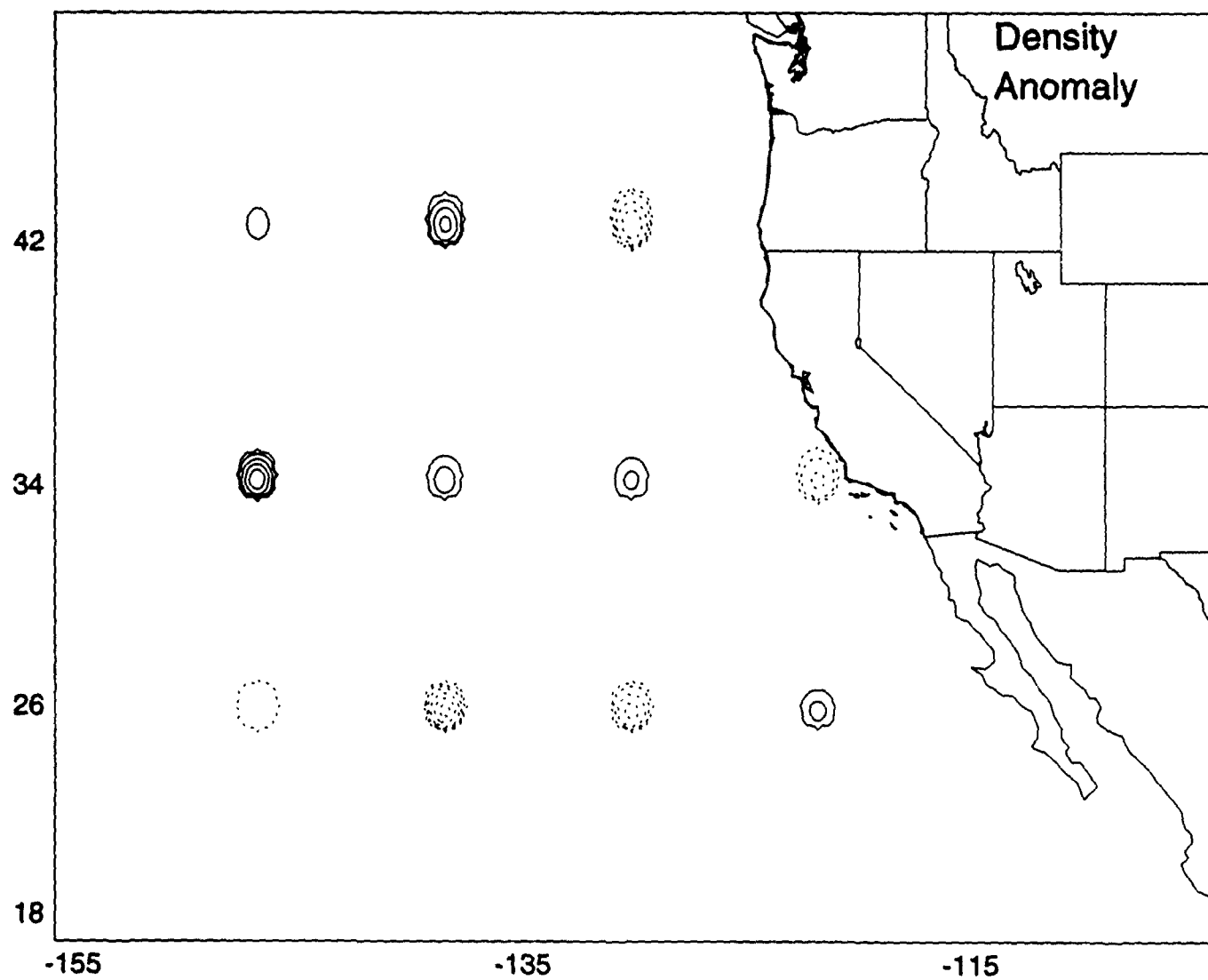
Figure 3: The peturbed density anomaly field. Contour intervals are 0.01 kg/m^3 and dashed lines indicate negative values.
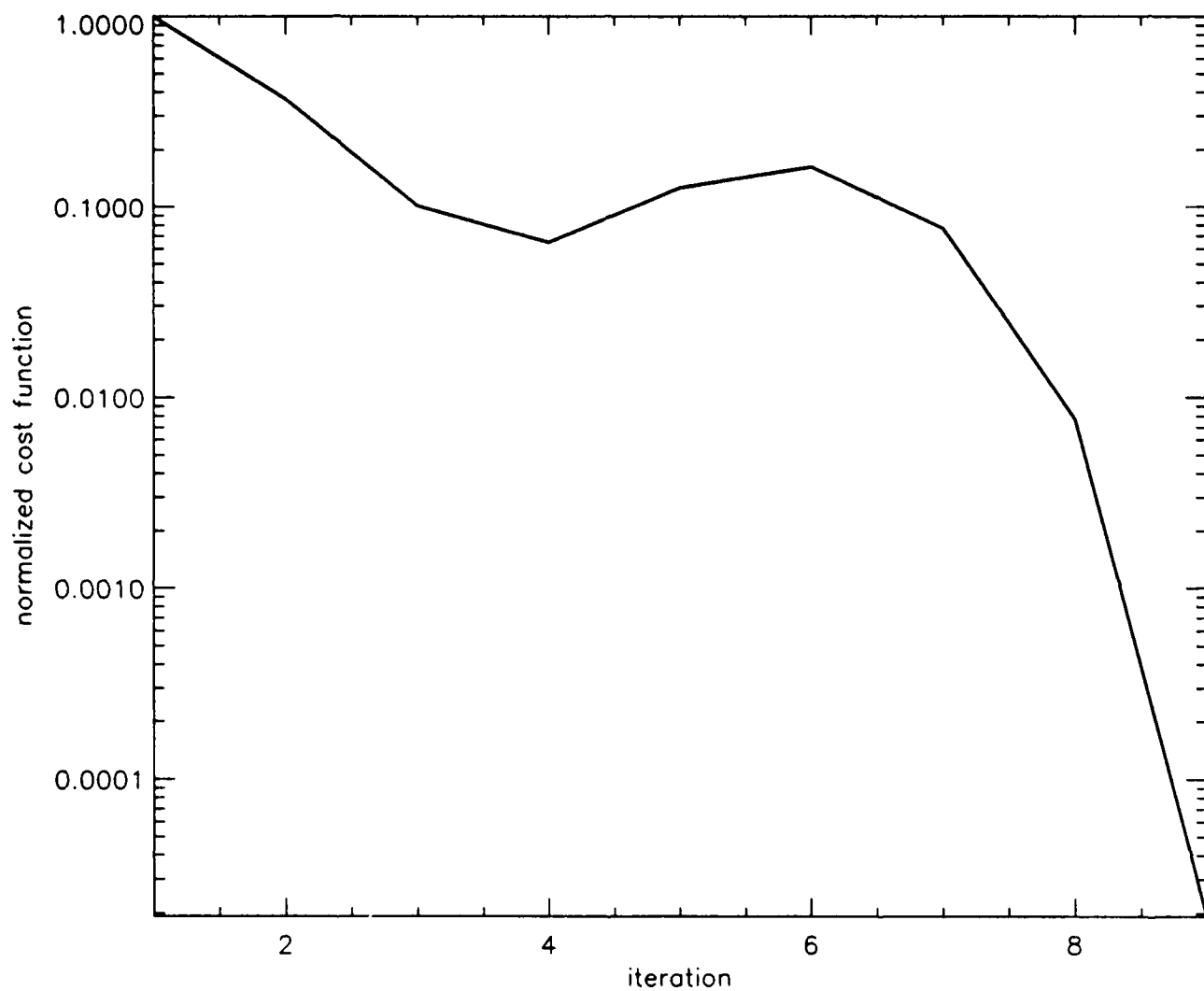
Figure 4: The peturbed density anomaly field. Contour intervals are 0.01 kg/m^3 and dashed lines indicate negative values.

A decadal impact of the 1982-83 El Nino was discovered. A paper on this was published in Nature and it made the cover of the 4 August 94 issue. There were articles about this in numerous newspapers, including the New York Times (8/9/94, p. B7) and Science News devoted the lead article of the 8/6/94 issue to this discovery.

This study showed an anomaly which stretched from Japan to Alaska in 1992-93. It was observed by satellite altimetry, sea surface temperature from satellite IR, and it was simulated by the NRL numerical ocean model. The ocean model showed that this anomaly stemmed from the 1982-83 El Nino and was used to link observations that were widely separated in space and time to the decadal impact of this El Nino. For example, a Rossby wave was tracked along 30N from 160W (Hawaii) to 140E (Japan) in the Geosat altimeter data, a phenomenon also seen in the ocean model. TOPEX altimeter data shows the propagation of the Rossby waves from the 1986-87 and 1992-93 El Ninos along 30N.

The NRL group is investigating 5-year changes in sea surface height observed by satellite altimeter data and simulated by eddy-resolving global and basin-scale ocean models. Both observations and models show these changes (O(10cm)) are strongly zonally banded with meridional wavelengths of roughly 10-20 degrees. In some regions observed and simulated 5-year changes agree fairly well (N. Pacific, N. Atlantic, S. Atlantic). In others they do not (Indian Ocean, S. Pacific, equatorial regions). Observation and simulation of decadal global ocean changes is an emerging capability where acoustic tomography can make a major contribution. Earlier attempts to observe long term changes using conventional observing systems have been too spotty or too fuzzy to permit identification of features like the zonal banding described above or the decadal impact of El Nino.

NRL performed two "identical twin" 1/8 degree eddy-resolving simulations of the Pacific Ocean north of 20S. These were run 1981-93 forced by ECMWF daily winds. They differed only in the initial state and a slight difference in the long term mean wind field. Penn State used these to investigate the effects of the nondeterministic mesoscale eddy field (i.e. the difference between the two simulations) on travel time variability between Hawaii and approximate USN stations from near Mexico to near Alaska. In most cases the difference variability due to mesoscale eddies was less than 10 percent of the total total variability in simulated travel times over 1981-93.

These simulations were also used to simulate the movement of drifting acoustic receivers (SSARS). These results were used in designing an array of drifting acoustic receivers and how this array would change with time over the period of 1 year. Maps of RMS variability of the velocity components averaged over the top 3 layers of the ocean model were computed. The regions of high variability indicate where the SSAR paths would be difficult to predict.

A bibliography of articles pertinent to the northern Pacific Ocean was compiled and made available to GAMOT project members. Ths bibliograpahy contains 170 entries.

Dr. Joe Mccaffrey, Mr. Peter Flynn, and Ms. Jan Dastugue traveled to the Engineering Research Center at Mississippi State University to discuss visualization techniques and to gain hands on training for the software Robert Moorehead's group has developed. The visualization package was brought back to Stennis Space Center and installed on the POPS Silicon Graphics Onyx computer.

TASK B
OCEAN MODELING

Model Validation of Ocean Temperature
Mark A. Johnson, University of Alaska

Our effort is a validation of the GAMOT methodology to derive oceantemperatures, and hence travel times, from the NRL model. This isdone by comparing the computed temperatures with actual temperaturesmeasured by expendable bathythermographs (XBT) at 300m over a broad region of the northeast Pacific for the period 1980 through 1984. Model temperatures and model-derived temperatures are constrained by the historical Levitus temperature data set that includes long-term variability from a variety of sources. Such constraints to historically observed temperature are unacceptable for GAMOT modelling that hopes to look at climate variability. Levitus data is also used by acousticians to compute parameters related to observed or expected travel times. In order to believe the temperatures from the NRL model, and therefore believe the estimates of travel times, we must be able to show that the NRL model can make valid estimates of temperature, since thermodynamics are not one of the model variables. We show below a methodology for meeting this goal.

We assume that ocean temperature at 300m is related to the temperature in the upper kilometer for all scales of variability but particularly for low frequency dynamics. Travel time changes are very sensitive to the temperature in the upper 500 or 1000m, so the temperature at 300m is a reasonable depth to choose for temperature comparisons.

In the last quarterly report we showed significant differences between historical Levitus and observed temperatures that highlighted the need for accurate models to predict seasonal and interannual changes. Such models {\bf cannot} be constrained to a historical mean temperature such as Levitus. A model has to be free to simulate these and longer time scale variability to be useful for global change research. This approach satisfies the SERDP objective of developing forecast systems and models to enhance prediction of environmental events.

We approach this validation in the following manner. The NRL model data between 1980 and 1984 will be used to estimate temperature. Travel time calculation are based on:

$$\sigma C = \eta \frac{dC_p}{dz} \qquad (1)$$

where:

$$\frac{dC(T,S,z)}{dz} = \frac{\delta C}{\delta T}\frac{dT}{dz} + \frac{\delta C}{\delta S}\frac{dS}{dz} + \frac{\delta C}{\delta z} \qquad (2)$$

One can subtract $\frac{\delta c}{\delta z}$ to move it to the l.h.s. Then:

$$\frac{dC_p}{dz} = \frac{dC}{dz} - \frac{\delta C}{dz} \qquad (3)$$

where the last term in (3) in a constant. Now the vertical
gradient of sound speed from the sound speed profiles one derives from
the Levitus daa uses a forward difference:

$$\frac{dC_i}{dz_i} = \frac{C_{i+1} - c_i}{z_{i+1} - z_i} \qquad (4)$$

By analogy, we can compute temperature perturbations at any
depth by:

$$\delta T = \eta \frac{dT}{dz} \qquad (5)$$

where the r.h.s. is computed by multiplying the model interface perturbation
by the vertical gradient in temperature from Levitus. We can add this
perturbation to the absolute temperatures of Levitus to get a total temperature
at any depth, or we can examine the model derived perturbations alone. If we
center the difference shown in (4) to 300m, the computed temperature can be
compared with measured temperatures from XBTs.

We have followed this approach and computed the absolute temperatures
from the NRL model for a subdomain of the northeast Pacific in collaboration
with John Spiesberger and Anatoly Fabrikant at Pennsylvania State
University. These data are now being compared with the gridded XBT data.
We expect to present the results of this comparison at the January GAMOT
meeting at Mississippi State University.

We have used observed temperatures at 300m from XBTs launched between
June 1976 and November 1984 and the model ULT from the FSU model as
well along three geodesic paths to find an empirical relation between ULT
and absolute temperature. Temperatures from the FSU model will be
compared with the NRL model results as well.

A paper analyzing the FSU model for travel time changes over decadel scales
is now complete, written in collaboration with Dr. Steve Meyers at Florida
State University, and is ready for submission. It is:

Meyers, S., M. Johnson, M. Liu, J. O'Brien, and J. Spiesberger, Interdecadal variability in a numerical model of the northeast Pacific ocean, submitted to Geophysical Research Letters, 1994.

NUM	TASK B	Start Date	Finish Date
B.1	OBTAIN EQUATORIAL PAC WIND FIELDS FROM 80-91 AND DRIVE THE EQUATOR MODEL	4/14/93	5/31/93
B.2	EXTRACT THE COASTAL KELVIN SIGNAL FROM THE EQUATOR MODEL AND DRIVE THE MID LATITUDE MODEL	6/1/93	6/30/93
B.3	INTEGRATE THE MODEL SOLUTIONS BETWEEN HAWAII AND WEST COAST RCVRS	6/1/93	6/30/93
B.4	COMPARE WITH OBSERVATIONS AND IDENTIFY VARIABILITY IN ACOUSTIC TRAVEL TIMES	7/1/93	9/1/93
B.5	DESIGN FUTURE EXPERIMENTS	9/15/93	4/10/94
B.6	ADD MODEL COMPLEXITY AND VERTICAL STRUCTURE TO IMPROVE ESTIMATES.OF TRAVEL TIME	4/15/94	9/1/94
B.7	RUN NRL MODELS	9/15/94	4/1/95

NUM	TASK B	Start Date	Finish Date	1993 A M J J A S O N D	1994 J F M A M J J A S O N D	1995 J F M A M J J
B.8	USE REAL DATA TO ASSIMILATE INTO OCEAN MODELS OF THE NORTH PACIFIC	12/11/9:	7/2/95			
B.9	SUBMIT FINAL REPORT	4/15/95	6/30/95			

A Physically Consistent Formulation of Lateral Friction in Shallow Water Equation Ocean Models

Alexander F. Shchepetkin and James J. O'Brien

Center for Ocean Atmosphere Prediction Studies
The Florida State University, 020 Love bld., Tallahassee, FL 32306-3041

August 28, 1994

A B S T R A C T

The use of dissipation in numerical ocean models has two purposes: first, to simulate processes in which the friction is physically relevant; and second, to suppress the accumulation of energy in the smallest resolved scales to prevent numerical instability. This study shows that even for the latter case the form of the friction term must be chosen in a physically consistent way. Ignorance of this requirement may cause severe violation of fundamental physical principles reducing the fidelity of the numerical solution even if the friction is essentially small. Several forms of the lateral friction term commonly used in numerical ocean models are discussed in the context of shallow water equations with nonuniform layer thickness. It is shown that in a numerical model tuned for the minimum possible dissipation, the improper form of the friction term creates finite artificial vorticity sources which do not vanish with increased resolution, even if the viscous coefficient is reduced consistently with resolution.

An alternative numerical implementation of the no-slip boundary conditions for an arbitrary coast line is considered. It was found that the quality of the numerical solution may be considerably improved by discretization of the viscous stress tensor in such a way that the numerical boundary scheme approximates not only the stress tensor to some order of accuracy, but also simulates the truncation error of the numerical scheme used in the interior of the domain. This precorrection procedure ensures error cancellation during subsequent use of the elements of the tensor in the discrete version of the momentum equations, allowing for approximation of the equations without decrease in the order of accuracy near the boundary.

I. Introduction

The ocean exhibits a variety of different phenomena of spatial scales from centimeters to thousands of kilometers, and even the largest modern computers are not powerful enough to resolve all the possible features in the ocean at the same time allowing molecular viscous dissipation to chose which of its small scale process should persist and which should decay. As a consequence, dissipative terms are often parametrized as eddy viscosity, which has become a *tuning* parameter of numerical models rather than a concept which has a clear background in physics. In most cases the influence of dissipation should be as small as possible, so it is natural to pose the following question: Does the particular form of the viscous term have any significance? Before answering this question, let us reformulate it. There is no doubt that in cases when friction is physically relevant, the form of the friction term should be adequate to the phenomenon under consideration. As for the situations when one tries to preserve inherent conservation properties of the fluid motion in a numerical experiment, there is no role of viscous dissipation other than removing energy from the smallest, and therefore underresolved, scales in order to prevent an ocean model from being numerically unstable. What should be done in order to perform this role without, or with as small as possible, discrepancy to the phenomenon of particular interest?

An example of an efficient "purely technological" solution to the problem may be illustrated by the approach adopted in spectral simulations of freely decaying two-dimensional turbulence. This is the scale selective friction or hyperviscosity,

$$-\nu(-\nabla^2)^\alpha \mathbf{u},$$

where $\alpha = 2, 4, \ldots$. The motivation is the following: In real geophysical fluid motions enstrophy (and also some fraction of energy) cascades into small scales and is dissipated by molecular viscosity. In a computational model nothing can be smaller than the grid size, so let friction be almost equal to zero everywhere except in the smallest scales the model resolves. It was pointed out (e.g., Farge and Sadornay, 1989) that in the context of shallow-water equations, the ratio of energy dissipation to enstrophy dissipation becomes smaller as the parameter α increases. This motivates the use of large values of α when the primary purpose of the model is to simulate a *nondissipative* system. A typical value of α is chosen to be from 6 to 8, while the hyper-Reynolds number defined as $\mathcal{R}e = \mathcal{U}\mathcal{L}^{2\alpha-1}/\nu$ is about $10^{+18}\ldots10^{+20}$. This Reynolds number, however, has no physical meaning. It makes more

2

sense to think about dissipation in terms of relative damping of the Nyquist wavenumber Fourier components per some characteristic time scale, say eddy turn-over time. One can construct an *energy conserving dissipative* operator (*Sadornay & Basdevant, 1985*), which dissipates enstrophy only.

Even though hyperviscosity effectively solves the numerical problem, it is of very limited applicability. First, hyperviscosity has no clear physical background and when friction is physically relevant something else should be used instead of, or along with, the hyperviscous dissipation. Second, from a mathematical point of view, hyperviscosity brings higher order derivatives into the system, and therefore it requires an additional *non-physical* set of boundary conditions. It is practically difficult to implement these sophisticated high order differential operators, though it is possible, and doing so would lead to an inefficient numerical model because it spends a large fraction of the computations to calculate these dissipation terms. Spectral simulation in a doubly periodic domain is the lucky exclusion from this rule.

Practical ocean modelers traditionally use more or less physically realistic parametrization of dissipation. Thus, as a rule, the form of viscous term is similar to molecular viscosity, except for the absolute value of the friction coefficient, which is often chosen for numerical reasons. Scale analysis is the most commonly used tool to decide which terms should be retained and which should be disregarded. Scale analysis is often performed without retaining the symmetries or conservation properties of the original equations. At the same time, perfect property conserving (e.g., mass, potential vorticity, enstrophy conserving) numerical schemes have been designed for geophysical applications. In these schemes everything is taken into account except friction. There is an excuse: friction is a dissipative term, so nothing has to be conserved by friction. But is it always the case? If so, nothing else has to be discussed. If, however, the friction term has to obey some fundamental physical conservation laws (despite its dissipative nature), why should we use perfect numerical schemes with imperfect friction in the same numerical model?

II. The nature of dissipation.

The physically consistent form of dissipation was discussed in the literature (e.g. Obukhov, 1962; Bleck and Boudra, 1981; Hayens and McIntyre, 1990; Gent and McWilliams, 1992; Gent, 1993; Schär and Smith, 1993). From the physical point of view, one should distinguish several different phenomena associated with dissipation. Among them, horizontal

3

viscous dissipation is the only one which is necessary in any ocean model for numerical reasons, and therefore it deserves special consideration in the context of the present paper. The other terms will not be discussed, however, they may be included in the numerical model later. We choose the framework of high resolution shallow water layered ocean models, applied to process study physics, including vortex dynamics and coastal oceanography.

At the first glance, the representation of horizontal friction in layered models is a trivial issue. According to the well known procedure, shallow water equations may be derived by vertical integration of the primitive equations. The latter are obtained from the Navier-Stokes equations through scale analysis, neglecting the vertical acceleration versus the acceleration of gravity. Therefore, it should be possible to derive the form of the friction term by the same procedure. However, it does not work (e.g., P.Gent, 1993). We will see soon that this form of friction contradicts fundamental physical principles such as the momentum conservation law.

The reason why this derivation fails is the fact that the scale analysis of the Navier-Stokes equation is done without taking into account their inherent symmetries and constraints which may be derived from these equations. These properties were considered theoretically in the context of continuously stratified fluid with the presence of dissipative forces and diffusion long ago, but this study was practically ignored by numerical modelers up to recent times (e.g., Obukhov, 1962; see also Hayens and McIntyre, 1987, for the review). Special attention was paid to the potential vorticity conservation theorem, which was generalized to the case of nonadvective (i.e., dissipative) fluxes. It was shown that there is no flux of the potential vorticity through an isentropic surface even if there is mass flux across this surface (Hayens and McIntyre, 1990). Due to dissipative fluxes the isentropic surfaces do not correspond to the material surfaces in the general case. In the present paper, however, we shall restrict our study to the case when density interfaces are material surfaces. Therefore, all layer interfaces, the free surface and bottom surface are assumed to be impermeable for the dissipative fluxes.

Isopycnal diffusion of a passive scalar was discussed by Gent and McWilliams, 1990, in the context of a three-dimensional density-coordinate system. In their approach the cross-isopycnal diffusive flux was assumed to be zero. This theory may be modified to the case of layered system by formal substitution of h/ρ instead of $\partial h/\partial \rho$. It should be pointed out that isopycnic coordinate systems are curvilinear in general case, therefore a careful

4

consideration of diffusion of a vector quantity (velocity) is needed to take into account all geometrical terms associated with the curvilinear coordinates. It can be easily shown that a standard approximation applied to the set of primitive equations, when horizontal and vertical diffusion coefficients are independent leads to a physically inconsistent interpretation of diffusion. Isopycnal and cross-isopycnal (diapycnal) diffusion terms should be introduced instead.

One can formulate the fundamental properties of the dissipation for the shallow water equations. Regardless of the particular parametrization of the friction coefficient, the following are required:

(i) In the transport form (conservation form) of the momentum equations, the lateral friction term must have the form of the divergence of a tensor. This means that the integral of this term over some two-dimensional domain can be converted to a boundary integral of the viscid momentum flux through the boundary. If the friction term cannot be presented in this form, it means that there is a volume part of integral; i.e., momentum is created by friction *inside the domain*, violating the momentum conservation principle. It should be pointed out that the momentum flux in the shallow water equations is already an integrated quantity. So, the two-dimensional integral is equivalent to the integral of the viscid momentum flux over three-dimensional domain bounded by two isopycnic surfaces.

(ii) This tensor must be symmetric. If the tensor is not symmetric, given some fluid element measured by $dxdy$, as seen from above, it is possible to see that the torque created by the viscous stress applied to the element is equal to the product of the difference of the off-diagonal elements of the tensor and the area of the element, $dx \cdot dy$. According to the angular momentum conservation law, this torque is equal to the rate of change of the angular momentum of the fluid element, which is equal to the product of the moment of inertia of the element and the angular acceleration. As the moment of inertia is proportional to the area of the element squared, while the torque is proportional only to the area, the angular acceleration goes to infinity when the area goes to zero. In terms of fluid mechanics this would mean an infinitely large source of vorticity due to the friction.

(iii) The friction must be dissipative, i.e. in the kinetic energy equation the friction is composed of the term which has the form of divergence of a vector and the negatively definite term in the right hand side. Again, integral of the friction term over some domain may be expressed as a boundary integral and a negatively definite volume part, which

5

means that energy is dissipated inside the domain.

(iv) The friction depends on the symmetric part of the local deformation tensor. Dependence of the antisymmetric part as well as the velocities or transports would mean that the viscous stress is not invariant under coordinate transformations such as going to uniformly rotating or moving with a constant velocity coordinate frame. As a consequence, the viscous stress identically vanishes for the velocity field like solid-body motion or solid-shell rotation of a infinitely thin layer on the surface of a sphere.

As a comment to (iv), it is interesting to note that the two-dimensional Laplace operator of a vector field on the surface of a sphere cannot be derived from three-dimensional operator by neglecting all terms with radial component of the vector and derivatives with respect the radius. This derivation would lead to a wrong geometrical term. Even though this term is always small in the geophysical applications, one can easily verify that as a consequence of this derivation, the solid-shell rotation would be subjected to uniform spindown instead of being a stationary solution.

If (i) and (ii) are satisfied, it is possible to show that the dissipation term in the absolute vorticity equation has the form of the divergence of a vector (recall that vorticity is a scalar quantity in two dimensions). This means that absolute vorticity (which can be interpreted as *conient* of potential vorticity in layer H) is not destroyed or created in the *interior* of the fluid by friction, but the net rate of change of absolute vorticity inside the domain is equal to the net flux of vorticity through the boundary. Thus, the potential vorticity and the absolute vorticity equations may be written as,

$$H\frac{D}{Dt}\left(\frac{\zeta+f}{H}\right) = \frac{D}{Dt}(\zeta+f) + \frac{\partial u_\alpha}{\partial x_\alpha} = \epsilon_{\alpha\beta}\frac{\partial}{\partial x_\alpha}\left(\frac{1}{H}\frac{\partial\sigma_{\beta\gamma}}{\partial x_\gamma}\right) = \frac{\partial}{\partial x_\alpha}\left(\frac{1}{H}\frac{\partial}{\partial x_\gamma}\left(\epsilon_{\alpha\beta}\sigma_{\beta\gamma}\right)\right),$$

where $\zeta = \epsilon_{\alpha\beta}\partial u_\beta/\partial x_\alpha$ is relative vorticity; f is local Coriolis parameter; $\sigma_{\alpha\beta} = \sigma_{\beta\alpha}$ is the viscous stress tensor; $\epsilon_{12} = 1$, $\epsilon_{21} = -1$, $\epsilon_{11} = \epsilon_{22} = 0$; and summation rule for repeated indices over the range $1, 2$ is assumed. Consequences of this equation were studied by Schär, 1993. It was shown that in addition to the usual (Laplacian) diffusion of vorticity it yields two additional fluxes, which depend on mutual orientation of the gradients of layer thickness and vorticity as well as the gradients of layer thickness and velocity divergence. We should emphasize the system of three-dimensional nonhydrostatic Navier-Stokes equations yields a similar property of the dissipation term in the vorticity

6

equation, while the primitive equations do not retain this property. It is interesting to note that in three dimensions this issue requires special physical consideration, Obukhov, 1962, but in the context of shallow water it is a formal consequence of the tensor form of the friction term.

III. Friction in numerical ocean models.

The failure to obtain a physically consistent friction term from the set of three-dimensional primitive equations, or, at least, absence of simple straightforward way to do so, motivates development of a phenomenological approach to the dissipation term in shallow water theory. This is similar to the classical formulation of the viscosity term in two- and three-dimensional hydrodynamics, e.g. Landau and Lifshitz. In the context of shallow water theory this approach was discussed by Schär and Smith, 1993. Following this idea, we express the dissipation term in the momentum equations as divergence of viscous stress tensor,

$$\sigma_{\alpha\beta} = A_1 H \left(\frac{\partial u_\alpha}{\partial x_\beta} + \frac{\partial u_\beta}{\partial x_\alpha} - \delta_{\alpha\beta} \frac{\partial u_\mu}{\partial x_\mu} \right) + A_2 H \delta_{\alpha\beta} \frac{\partial u_\mu}{\partial x_\mu} , \tag{1}$$

and will prove that it has properties (i-iv) postulated above.

Three other versions of the friction term are frequently used for numerical ocean models:

$$AH\Delta\mathbf{u} \tag{2.1}$$

$$\text{div}(AH \text{ gradu}) \tag{2.2}$$

$$A\Delta\mathbf{U} \tag{2.3}$$

where Δ is the two-dimensional Laplace operator of a two-dimensional vector.

In the case of uniform layer thickness and nondivergent flow the difference between all four versions disappears and all of them have properties (i)-(iv), which makes the simplest possible version, Laplacian of velocity, physically correct. This situation is identical to the two-dimensional hydrodynamics. The main difference of shallow water equations from the two-dimensional hydrodynamics is the fact that the flow is divergent.

In the general case, however, none of the three versions of (2) satisfies all four requirements (i)-(iv). Formal vertical integration of the three-dimensional primitive equations

7

with depth-independent horizontal velocities leads to the version of (2.1). This term is consistent with (iii) and (iv), but not with (i) and (ii). The (2.2) is in agreement with (i), (iii) and (iv), but violates (ii); while (2.3) does not satisfy (ii), (iii) and (iv).

For a flow close to the quasigeostrophic regime, the disturbance of layer thickness is small. In these types of flows the largest gradients of the layer thickness are associated with coherent structures and are advected with the fluid particles. Consequently, for a given fluid particle the layer thickness tends to be conserved as long as the coherent structure remains the same. The characteristic time scale of the structural change of the flow is related to the time scale associated with interaction of different coherent structures rather than advection of particles within the same coherent structure. This time scale is relatively large, which makes the flow practically nondivergent. The divergence of the velocity field is of order of $\mathcal{R}o \cdot \mathcal{H}/\mathcal{L} \ll 1$ relative to the deformation rate, so Laplacian of velocity becomes a reasonable approximation for the friction term. $\mathcal{R}o \ll 1$ is the Rossby number and $\mathcal{H}/\mathcal{L} \ll 1$ is the ratio of the vertical and horizontal scales. Indeed, this estimation gives an even better justification for the use of this form of friction than the range of applicability of the quasigeostrophic theory itself. However, this kind of friction is not applicable to the case where the variation of the layer thickness is not small, even if the fluid is nearly at rest, e.g. the barotropic flow over a sloping bottom, or bottom layer of the multilayer stratified system. In both situations the divergence of the velocity field is of order of $\mathcal{O}(|\nabla H|)$ of the value of deformation rate.

It is interesting to note that in the context of a non-rotating environment and vorticity-free flow, i.e. $\partial u_\alpha / \partial x_\beta = \partial u_\beta / \partial x_\alpha$, the version (2.2) of the friction term can be interpreted as the divergence of a symmetric tensor and is consistent with all four requirements (i)-(iv). Moreover, if no vorticity is created *on the boundary* or brought *through the boundary* (e.g. in the case of appropriate influx boundary condition), the flow *remains vorticity free* even though it is a viscid flow. However, to realize this situation one needs a very special configuration of stress free boundaries or consider a to boundless fluid.

In the present study we use the trace free version of the friction stress tensor of the form (1) with $A_2 \equiv 0$. This approach does not require this restriction and can be easily extended to the general form. The question of the importance of the second term in (1) needs some additional consideration. Schär and Smith, 1993, dropped it with the argument that the isotropic part of the stress tensor has already been accounted for in the

pressure term in the momentum equation, so there is no need of an additional isotropic term. However, it is easy to see that these two terms are responsible for essentially different effects. The dependence of pressure from the divergence of velocities provides a mechanism for propagation of gravitational waves, while the second viscous term is responsible for their dissipation.

As seen from the discussion above, friction terms used in numerical models do not always agree with the postulates formulated in part II. Thus, for example, the asymmetry of the viscous stress tensor, as it is admitted in (ii) cannot be *physically small*. However, because the size of the fluid element cannot be smaller than the grid size Δx, in a numerical model tuned to the minimum possible dissipation, the *artificial* vorticity source, mentioned in (ii), aliases as a finite source. This is because for the second order finite difference approximation the amplitude of the numerical noise decreases as $(\Delta x)^2$, the viscous dissipation used for suppression of the noise is reduced in the same way. Thus, the artificial source of vorticity remains finite. When simulation of a physically complex situation (say, an ocean model with realistic wind forcing, realistic coastline and realistic bottom topography) is performed, this artificial effect may be masked out by other effects. We shall demonstrate that in situations when the correct representation of eddy dynamics is important, this effect may produce considerable distortion of the potential vorticity field, even if friction is small.

In the numerical experiment described below, we use three versions of viscous friction: the trace-free version of (1) and the versions (2.2) and (2.3). Operator (2.2) was used (*incidentally?*) by Schär and Smith, 1993, after the discussion of the physically consistent version of friction (see appendix to Schär and Smith, 1993, for the description of details of the numerical model they developed). In both cases the friction coefficients were equal to each other and were chosen to be as small as possible, but sufficiently large to maintain the numerical stability of the model. The Reynolds number for the experiments described below (based on the domain size) is roughly 12000, grid resolution is 301 × 301. We simulate a barotropic shallow water layer with steep topography. The concentric dashed circles on Fig. 1 represent a gaussian "sea mountain". The height of the mountain equals 90% of the layer depth away from the mountain. We use a shallow water equation model, which can be used for both compressible (with free surface) and incompressible (rigid lid approximation) flows. Centered second order finite difference on Arakawa C-grid in

9

space and fully implicit second order Crank-Nickolson in time numerical scheme is used to discretize the momentum equations and the continuity equation. We initialize a dipole away from the mountain, by specifying the desirable potential vorticity field and resolving the coupled nonlinear elliptic problem to obtain the transport streamfunction (the initial state is assumed to be nondivergent) and initial layer thickness, see APPENDIX A for the details. This initial condition allows a smooth start without exciting strong surface gravity waves. For our experiments we specify a uniform potential vorticity field everywhere, except for the dipole, which consists of two eddies of equal intensity (in terms of relative vorticity). Both eddies are originally circular and have roughly uniform potential vorticity distribution within their cores with steep potential vorticity fronts on the edges of the cores. These experiments are performed on the f-plane. In the absence of the sea mountain the dipole propagates along a straight line with minor structural readjustment to a steady moving pattern, practically without loss of intensity and filamentation. Results of the numerical integration are shown in Fig.1.

The evolution of the potential vorticity field for the case of trace-free version of friction operator (1) is shown on Fig. 1a. The dipole approaches to the mountain, interacts with it, turns, leaves it and moves away along the straight line in the direction approximately 170^0 to the right from the direction of the original propagation. After the interaction, the original shape of the dipole is restored and there is a small tail of vorticity behind it, which slowly disappears being advected by the background flow and eventually dissipated by friction. It should be pointed out that even if there is no local potential vorticity anomaly, the water is never at rest. When the dipole is far away from the mountain (before or after interaction), there is weak clockwise circulation of water above the mountain. This is necessary to compensate the f/H term in the potential vorticity in order to keep it uniform. The circulation becomes visible by the slow advection of the vorticity filament left after the dipole leaves the mountain. Since the velocity field associated with this flow does not correspond to the solid body motion, the friction causes some modification of the flow, so eventually the potential vorticity field will not be uniform near the top of the mountain even for the case of the physically consistent friction term. In the experiments presented here the friction coefficient is kept sufficiently small, so the characterictic time scale of this modification is much larger than the interaction time. Thus, we should not expect departure from the uniform potential vorticity field near the top of the mountains

10

in the experiment with friction term (1). Note that during the whole interaction process, the values of the minimum and the maximum of the potential vorticity anomalies inside the cores remain the same, and the only visible consequence of dissipation is the smoothing of the vorticity fronts on the edges of the vortex cores.

The content of Fig. 1b is the same as 1b, but the friction term given by (2.2). The behavior of the potential vorticity field is approximately the same, but an artificial generation of potential vorticity is seen on the top of the mountain. Note, that before the dipole approaches the top of the mountain, the spot of negative vorticity has been created. The dipole picks the spot and carries it away from the mountain, so that no potential vorticity anomaly is seen on the top of the mountain after the dipole left the top. But eventually a new spot develops and linear growth of the potential vorticity anomaly is seen on the top of the mountain.

There is an artificial generation of potential vorticity if friction operator (2.3) is used, Fig. 1c.

Difference between the potential vorticity fields on Fig. 1b and Fig. 1a is shown on Fig. 1d. Fig. 1e represent the difference between Fig. 1c and Fig. 1a. Contour interval on Fig. 1c and 1d is 10 times finer than on Fig.1a, 1b and 1c. White areas inside the most dark pattern correspond to the region where the difference between the potential vorticity anomalies is bigger than 20%.

Comparison of Figs. 1a, 1b and 1c shows that there are two consequences of the artificial sources of vorticity: First, the residual flow on the top of the mountain. Second, the deflection angle of the dipole is slightly changed. The later effect is very small and it cannot be seen on Figs. 1a, 1b and 1c. But it explains relatively large difference of the potential vorticity fields near the dipole on Figs. 1c and 1d at $t = 2.00$. It is interesting to note that this change has opposite sign for the dissipation terms (2.2) and (2.3).

From this experiment we see that if the friction term (1) is used, the result is very similar to that obtained in the inviscid theory. The friction operator we used provides effective damping of the numerical noise without additional effects. We have investigated all three dissipation operators (2) for the case of compressible (with free surface) and incompressible (with rigid lid) barotropic shallow water flows. The numerical model we used provides a

11

possibility of gradual transformation from the compressible to incompressible case. The second may be obtained as the limit of the first when the acceleration of gravity goes to infinity. In this case, the ratio of the elevation of free surface to the layer thickness becomes infinitely small. This ratio may be interpreted as a natural measure of compressibility of the flow. In "the most compressible case" we have considered the maximum value of this parameter may be of order of 0.5, when the dipole reaches the top of the mountain.

It was found, that the friction operator (1) does not produce an artificial source of vorticity. Among the three versions of friction terms (2), (2.2) is the best choice. For (2.2), the artificial generation of vorticity depends on the compressibility. This gives a tolerable solution for the incompressible case, but a departure from incompressible flow causes a dramatic increase of the artificial generation of vorticity.

IV. Boundary conditions in numerical ocean models.

We have discussed physical and numerical consequences of dissipation in the interior of the basin. Besides its physical role, dissipation controls the stability of numerical models. Numerical instability often appears first not inside the model basin, but on the boundary. The necessity to eliminate this instability requires a larger dissipation coefficient. As a rule, this leads to a global increase of dissipation, so that interesting features of the fluid motion may also be suppressed.

Slip-free boundary conditions are often implemented as reflection boundary conditions. On a staggered Arakawa C-grid, the velocity component normal to the boundary is explicitly set to zero, while the tangential velocity is reflected with respect to the wall. Then the interior discretization scheme is applied. This approach has two main shortcomings: First, one can easily see (APPENDIX B) that it leads to an underestimation of the viscous term near the boundary. Secondly, the reflection rule conflicts with no normal component boundary condition on convex corners of the coast line. The no-flux boundary condition always overrides the reflection and it can be shown that the friction term is approximated in the points in front of the corner with the same truncation error as in interior. If the coastal line has a region with a row of corner points next to each other, this place behaves as a source of numerical distortion, because terms are approximated with different accuracy in adjacent points. In this chapter we describe an alternative implementation of no-slip boundary conditions, which is free of the above disadvantages.

We may formulate the shallow water equations in geophysical spherical coordinates as follows:

$$\frac{\partial V_\lambda}{\partial t} + \nabla_\lambda P_{\lambda\lambda} + \nabla_\phi P_{\lambda\phi} - \frac{2\tan\phi}{a}P_{\lambda\phi} - fV_\phi = -\mathcal{P}_\lambda + \mathcal{F}_\lambda$$

$$\frac{\partial V_\phi}{\partial t} + \nabla_\lambda P_{\lambda\phi} + \nabla_\phi P_{\phi\phi} + \frac{\tan\phi}{a}(P_{\lambda\lambda} - P_{\phi\phi}) + fV_\lambda = -\mathcal{P}_\phi + \mathcal{F}_\phi \qquad (3)$$

$$\frac{\partial h}{\partial t} + \nabla_\lambda V_\lambda + \nabla_\phi V_\phi - \frac{\tan\phi}{a}V_\phi = 0$$

where λ, ϕ are longitude and latitude, the differential operators ∇_λ and ∇_ϕ and their commutation rule are defined as follows:

$$\nabla_\lambda = \frac{1}{a\cos\phi}\frac{\partial}{\partial\lambda} \qquad \nabla_\phi = \frac{1}{a}\frac{\partial}{\partial\phi} \qquad \text{so that:} \qquad \nabla_\phi\nabla_\lambda = \nabla_\lambda\nabla_\phi + \frac{\tan\phi}{a}\nabla_\lambda$$

h is the layer thickness, V_λ, V_ϕ are transports in the longitudinal and meridional directions, $f = 2\Omega\sin\phi$ is the Coriolis parameter. $\mathcal{P}_\lambda$, and $\mathcal{P}_\phi$ are the pressure gradient terms. $\mathcal{F}_\lambda$, and $\mathcal{F}_\phi$ are the external forces: wind stress, effect of the bottom topography, etc. **P** is the symmetric tensor of the momentum flux density:

$$P_{\lambda\lambda} = \frac{V_\lambda V_\lambda}{h} - Ah\sigma_{\lambda\lambda}, \qquad P_{\phi\phi} = \frac{V_\phi V_\phi}{h} - Ah\sigma_{\phi\phi},$$

$$P_{\lambda\phi} \equiv P_{\phi\lambda} = \frac{V_\lambda V_\phi}{h} - Ah\sigma_{\lambda\phi}. \qquad (4)$$

A is the horizontal (strictly speaking, isopycnic) friction coefficient and $\sigma_{\alpha\beta}$ is the deformation tensor. This tensor is symmetric and trace-free so

$$\sigma_{\lambda\lambda} = -\sigma_{\phi\phi} = \nabla_\lambda v_\lambda - \nabla_\phi v_\phi - \frac{\tan\phi}{a}v_\phi$$

$$\sigma_{\phi\lambda} = \sigma_{\lambda\phi} = \nabla_\lambda v_\phi + \nabla_\phi v_\lambda + \frac{\tan\phi}{a}v_\lambda \qquad (5)$$

As the present approach may be applied for different problems, we do not specify any particular form of the pressure gradient term. Equations (3) may be used in context of a barotropic single layer model or may refer to some isopycnic layer in a multilayer model. The form of the dissipation terms does not depend on the application. Physically,

13

the use of the spherical coordinates is not important for the consideration of boundaries. However, the geometrical terms in the spherical coordinate momentum equations inhibit some numerical algorithms which may be successfully used for Cartesian coordinates. In particular, we will show that in most cases land boundary conditions cannot be formulated as a reflection rule for some quantities.

We use a staggered Arakawa C-grid to discretize all equations. In our elementary stencil $V_{\phi_{j,k}}$ is located half-grid to the *south* relative to the $h_{j,k}$, and $V_{\lambda_{j,k}}$ is half-grid *east* from the $h_{j,k}$. The grid intervals $\Delta\lambda$ and $\Delta\phi$ are the distances between *alike* points, for instance, $V_{\lambda_{j,k}}$ and $V_{\lambda_{j+1,k}}$. Centered differences are used to approximate spatial derivatives of all fields.

If the diagonal elements of the tensor $\mathbf{P}$ are specified at h-points, and off-diagonal at the vorticity points (hereafter referred as q-point) staggered half-grid east and half-grid south from the respective h-point), the discretization of (3) is straightforward:

$$
\frac{\partial V_{\lambda_{j,k}}}{\partial t} = -\frac{1}{a\cos\phi_k}\frac{P_{\lambda\lambda_{j+1,k}} - P_{\lambda\lambda_{j,k}}}{\Delta\lambda} - \frac{1}{a}\frac{P_{\lambda\phi_{j,k+1}} - P_{\lambda\phi_{j,k}}}{\Delta\phi}
$$

$$
+ \frac{2\tan\phi_k}{a}\frac{P_{\lambda\phi_{j,k+1}} + P_{\lambda\phi_{j,k}}}{2}
$$

$$
+ 2\Omega\sin\phi_k\frac{1}{4}\left(V_{\phi_{j,k}} + V_{\phi_{j-1,k}} + V_{\phi_{j,k-1}} + V_{\phi_{j-1,k-1}}\right) - \mathcal{P}_{\lambda_{j,k}} + \mathcal{F}_{\lambda_{j,k}}
$$

$$
\frac{\partial V_{\phi_{j,k}}}{\partial t} = -\frac{1}{a\cos\phi_{k-\frac{1}{2}}}\frac{P_{\lambda\phi_{j,k}} - P_{\lambda\phi_{j-1,k}}}{\Delta\lambda} - \frac{1}{a}\frac{P_{\phi\phi_{j,k}} - P_{\phi\phi_{j,k-1}}}{\Delta\phi}
$$

$$
- \frac{\tan\phi_{k-\frac{1}{2}}}{a}\left[\frac{P_{\lambda\lambda_{j,k}} + P_{\lambda\lambda_{j,k-1}}}{2} - \frac{P_{\phi\phi_{j,k}} + P_{\phi\phi_{j,k-1}}}{2}\right] \tag{6}
$$

$$
- 2\Omega\sin\phi_{k-\frac{1}{2}}\frac{1}{4}\left(V_{\lambda_{j,k}} + V_{\lambda_{j-1,k}} + V_{\lambda_{j,k-1}} + V_{\lambda_{j-1,k-1}}\right) - \mathcal{P}_{\phi_{j,k}} + \mathcal{F}_{\phi_{j,k}}
$$

$$
\frac{\partial h_{j,k}}{\partial t} = -\frac{1}{a\cos\phi_k}\frac{V_{\lambda_{j+1,k}} - V_{\lambda_{j,k}}}{\Delta\lambda} - \frac{1}{a}\frac{V_{\phi_{j,k+1}} - V_{\phi_{j,k}}}{\Delta\phi}
$$

$$
+ \frac{\tan\phi_k}{a}\frac{V_{\phi_{j,k+1}} + V_{\phi_{j,k}}}{2}
$$

where ϕ_k is defined at $u-$ or $h-$points, while $\phi_{k-\frac{1}{2}}$ is the value of ϕ at $v-$point.

14

Since,

$$h\nabla\mathbf{v} \equiv h\nabla\left(\frac{\mathbf{V}}{h}\right) = \nabla\mathbf{V} - \mathbf{V}\frac{\nabla h}{h}\ ,$$

the components of the sress tensor $\mathbf{P}$ are discretized as follows:

$$P_{\lambda\lambda j,k} \approx \frac{\left(V_{\lambda j,k} + V_{\lambda j-1,k}\right)^2}{4h_{j,k}} - A\Sigma_{j,k}$$

$$P_{\phi\phi j,k} \approx \frac{\left(V_{\phi j,k} + V_{\phi j,k+1}\right)^2}{4h_{j,k}} + A\Sigma_{j,k}\ ,$$

$(7,a)$

where

$$\Sigma_{j,k} = \frac{V_{\lambda j,k} - V_{\lambda j-1,k}}{a\Delta\lambda\cos\phi_k} - \frac{V_{\phi j,k+1} - V_{\phi j,k}}{a\Delta\phi} - \frac{\tan\phi_k}{a}\frac{V_{\phi j,k+1} + V_{\phi j,k}}{2}$$

$$- \frac{V_{\lambda j,k} + V_{\lambda j-1,k}}{2}\frac{h_{j+1,k} - h_{j-1,k}}{2h_{j,k}a\Delta\lambda\cos\phi_k} + \frac{V_{\phi j,k+1} + V_{\phi j,k}}{2}\frac{h_{j,k+1} - h_{j,k-1}}{2h_{j,k}a\Delta\phi}\ ,$$

$(7,b)$

and

$$P_{\lambda\phi j,k} = \frac{\left(V_{\lambda j,k} + V_{\lambda j,k-1}\right)\left(V_{\phi j,k} + V_{\phi j+1,k}\right)}{h_{j,k} + h_{j+1,k} + h_{j,k-1} + h_{j+1,k-1}} - A\Xi_{j,k}\ ,$$

$(7,c)$

where

$$\Xi_{j,k} = \frac{V_{\phi j+1,k} - V_{\phi j,k}}{a\Delta\lambda\cos\phi_{k-\frac{1}{2}}} + \frac{V_{\lambda j,k} - V_{\lambda j,k-1}}{a\Delta\phi} + \frac{\tan\phi_{k-\frac{1}{2}}}{a}\frac{V_{\lambda j,k} + V_{\lambda j,k-1}}{2}$$

$$- \frac{V_{\phi j+1,k} + V_{\phi j,k}}{2}\frac{1}{a\Delta\lambda\cos\phi_{k-\frac{1}{2}}}\frac{h_{j+1,k} - h_{j,k} + h_{j+1,k-1} - h_{j,k-1}}{h_{j,k} + h_{j+1,k} + h_{j,k-1} + h_{j+1,k-1}}$$

$(7,d)$

$$- \frac{V_{\lambda j,k} + V_{\lambda j,k-1}}{2}\frac{1}{a\Delta\phi_{k-\frac{1}{2}}}\frac{h_{j+1,k} - h_{j+1,k-1} + h_{j,k} - h_{j,k-1}}{h_{j,k} + h_{j+1,k} + h_{j,k-1} + h_{j+1,k-1}}.$$

The discrete equations (6) are valid everywhere, including the points near the boundaries. However, expressions (7,a)-(7,d) are applicable for interior grid points of the domain only. Thus, a special discretization of the stress tensor $P_{\alpha\beta}$ is needed on and near the boundaries.

Before discussing the discrete version of the land boundary conditions, we should note that equations (6) along with (7,a-d) give a second order of accuracy $\mathcal{O}((a\Delta\lambda\cos\phi)^2 + (a\Delta\phi)^2)$, approximation for the system of equations (3). Equations (7,a)-(7,c) give the second order of accuracy approximations for $P_{\alpha\beta}$. After substitution of these expressions into (6), the last one should give the first order of accuracy approximation of (3) because of division by $a\Delta\lambda\cos\phi$ and $a\Delta\phi$ in (6). The reason why there is no actual loss of the order of accuracy is the *error cancellation* due to the centered difference scheme. Errors of interpolation and finite difference errors of approximation of $P_{\alpha\beta}$, calculated in two adjacent grid points according to (7), may be estimated as the second derivatives of some functions times quadratic expressions of $\Delta\lambda$ and $\Delta\phi$. For the centered difference scheme, these errors will cancel each other and the residual error occurs only in the next order of accuracy. This means that for the boundary points when one-sided finite difference approximations are used to calculate derivatives, these approximations must be designed in such a way, that they simulate not only the derivative of the function, but *also the truncation error* of this derivative as it would be if it is approximated by the centered difference scheme. If this rule is always satisfied, the result will be the complete second order of accuracy approximation for the equations (3) and their boundary conditions.

This idea may be illustrated by the following example: If $f(x)$-is some function of coordinate x, $f_j = f(x_j)$, $\Delta x = x_{j+1} - x_j$ and the centered difference scheme is used to approximate the derivative of f,

$$\left.\frac{\partial f}{\partial x}\right|_{x_j} \approx \frac{f_{j+1} - f_{j-1}}{2\Delta x},$$

it is easy to see that

$$\frac{f_{j+1} - f_{j-1}}{2\Delta x} = \frac{\partial f}{\partial x} + \frac{1}{6}\frac{\partial^3 f}{\partial x^3}(\Delta x)^2 + \mathcal{O}((\Delta x)^4)\,,$$

and therefore, when using one-sided finite difference approximation for the derivative of f, it should be done as follows:

$$\left.\frac{\partial f}{\partial x}\right|_{x_j} \approx \left.\frac{\partial f}{\partial x}\right|_{x_j} + \frac{1}{6}\left.\frac{\partial^3 f}{\partial x^3}\right|_{x_j}(\Delta x)^2 = \frac{4f_j - 7f_{j-1} + 4f_{j-2} - f_{j-3}}{2\Delta x} + \mathcal{O}((\Delta x)^3)$$

16

This may be also rewritten as:

$$\frac{\partial f}{\partial x}\bigg|_{x_j} = \frac{f_{j+1}^* - f_{j-1}}{2\Delta x} \,, \qquad \text{where} \qquad f_{j+1}^* = 4f_j - 6f_{j-1} + 4f_{j-2} - f_{j-3} \,.$$

The right expression is nothing but the fourth order extrapolation for f_{j+1}.

All land boundary points are classified into eight groups: four in longitudinal and meridional directions ("90 degree"), i.e. north, east, south and west coasts *of the ocean*; the other four are diagonal ("45 degree") boundaries, northwest, northeast, southest and southwest coasts *of the ocean*. These names are given by direction of a vector normal to the coast line and pointed *from water to land*. No-slip boundary conditions are implied on all solid boundaries. In the configuration adopted here, meridional boundaries pass through V_λ-points; zonal pass through V_ϕ-points, while all diagonal boundaries are the straight lines going through both V_λ- and V_ϕ-points. As the diagonal components of the tensor **P** are defined at h-points, they are never needed to be calculated on the boundary. However, they cannot be calculated by (7,a) near the coast, because the value of h on the adjacent land point is needed. This value may be extrapolated and then this element is calculated according to (7,a)-(7,b). This also may be done explicitly, for example, to calculate the $P_{\lambda\lambda j,k}$ element near the eastern land boundary, where $h_{j+1,k}$ belongs to the land, and $V_{\lambda j,k} = 0$ due to the solid wall boundary condition, the following formula may be used:

$$
\begin{aligned}
P_{\lambda\lambda j,k} = &\frac{\left(V_{\lambda j-1,k}\right)^2}{4h_{j,k}} \\
&- A\left[\frac{-V_{\lambda j-1,k}}{a\Delta\lambda\cos\phi_k} - \frac{V_{\phi j,k+1} - V_{\phi j,k}}{a\Delta\phi} - \frac{\tan\phi_k}{a}\frac{V_{\phi j,k+1} + V_{\phi j,k}}{2}\right.\\
&\qquad - \frac{V_{\lambda j-1,k}}{2}\frac{4h_{j,k} - 7h_{j-1,k} + 4h_{j-2,k} - h_{j-3,k}}{2h_{j,k}a\Delta\lambda\cos\phi_k}\\
&\qquad \left. + \frac{V_{\phi j,k+1} + V_{\phi j,k}}{2}\frac{h_{j,k+1} - h_{j,k-1}}{2h_{j,k}a\Delta\phi}\right]
\end{aligned}
\tag{8}
$$

where $h_{j+1,k}$ has been avoided, and this is consistent with (7,a) in the sense discussed above.

17

The internal stencil is used for the nonlinear terms and derivatives of the transport to compute the diagonal elements on an h-points which are close to the 45-degree boundaries. However, one sided finite differences should be applied to approximate derivatives of the layer thickness in both directions.

Off-diagonal elements are needed to be calculated on the boundaries. As both velocities are equal on the boundary, the nonlinear term and both terms with derivatives of the layer thickness and the sphericity term vanish. The only terms to be computed are:

$$P_{\lambda\phi} = -A\nabla_\lambda V_\phi \qquad \text{on the western and eastern coasts of the ocean,}$$

$$P_{\lambda\phi} = -A\nabla_\phi V_\lambda \qquad \text{on the northern and southern coasts of the ocean.}$$

In the interior of the domain the centered difference expression is used to estimate $\nabla_\lambda V_\phi$ at the q-points:

$$\nabla_\lambda V_\phi \bigg|_{j+\frac{1}{2},k} \approx \frac{V_{\phi\, j+1,k} - V_{\phi\, j,k}}{a\Delta\lambda \cos\phi_{k-\frac{1}{2}}} = \frac{1}{a\cos\phi}\left[\frac{\partial V_\phi}{\partial\lambda}\bigg|_{j+\frac{1}{2},k} + \frac{1}{6}\frac{\partial^3 V_\phi}{\partial\lambda^3}\bigg|_{j+\frac{1}{2},k}\left(\frac{\Delta\lambda}{2}\right)^2 \right.$$
$$\left. + \mathcal{O}((\Delta\lambda)^4)\right]$$

The one-sided finite difference expression for $\nabla_\lambda V_\phi$, which gives the same truncation error in the second order of accuracy is the following:

$$\nabla_\lambda V_\phi \bigg|_{j+\frac{1}{2},k} \approx \frac{-4V_{\phi\, j,k} + V_{\phi\, j-1,k} - \frac{1}{5}V_{\phi\, j-2,k}}{a\Delta\lambda \cos\phi_{k-\frac{1}{2}}}$$
$$= \frac{1}{a\cos\phi}\left[\frac{\partial V_\phi}{\partial\lambda}\bigg|_{j+\frac{1}{2},k} + \frac{1}{6}\frac{\partial^3 V_\phi}{\partial\lambda^3}\bigg|_{j+\frac{1}{2},k}\left(\frac{\Delta\lambda}{2}\right)^2 + \mathcal{O}((\Delta\lambda)^3)\right] . \tag{9}$$

The no-slip boundary condition $V_{\phi\, j+\frac{1}{2},k} = 0$ was used to obtain (9). Equation (9) can be rewritten as a reflection condition for the transport:

$$V_{\phi\, j+1,k}^* = -3V_{\phi\, j,k} + V_{\phi\, j-1,k} - \frac{1}{5}V_{\phi\, j-2,k} ,$$

18

which is the fourth order extrapolation based on the values of the function at points $j+\frac{1}{2}, k$; j, k; $j-1, k$; $j-2, k$, with the condition that $V_{\phi_{j+\frac{1}{2}}} = 0$. The centered difference rule (7,c)-(7,d) is formally applicable now to calculate the derivative of V_ϕ on the boundary. Despite $V_{\phi_{j+1,k}^*} + V_{\phi_{j,k}} \neq 0$, no error will be made in the calculation of the nonlinear term because the other component of the transport vanishes anyway. If the simple reflection rule will be applied to h on the boundary, $h_{j+1,k}^* = h_{j,k}$, $h_{j+1,k-1}^* = h_{j,k-1}$, no error will be made in the term with derivatives of h, it will vanish, as it is supposed to be when the velocity is equal to zero. However, there is no way to correctly calculate the term due to the spherical geometry on the northern and southern solid boundaries. Therefore, this boundary condition may be formulated as a reflection rule only in Cartesian coordinates.

A fourth order two-dimensional extrapolation of h to the nearest land boundary is applied to compute the off-diagonal elements near the "45-degree" boundaries. For example, on the northeast coast:

$$
\begin{aligned}
h_{j,k}^* = h_{j-1,k} + h_{j,k-1} + h_{j-1,k-1} - 2h_{j-2,k} - 2h_{j,k-2} + h_{j-2,k-2} \\
+ h_{j-3,k-2} + h_{j-2,k-3} - h_{j-3,k-3}
\end{aligned}
\tag{10}
$$

Sometimes it is necessary to extrapolate value of the layer thickness to the same land h-point from two or more directions. This happens if the coast line has a very sharp feature, such as a peninsula represented by only one grid point surrounded by water from three sides, or, if it has an island, represented by only one grid point. Thus, this boundary condition cannot be formulated in terms of an appropriate reflection rule.

In the conclusion of this section, we shall compare two ocean models with different versions of the numerical formulation of the no-slip boundary conditions on a realistic form of coastline. Both models are $1^1/_2$ layer reduced gravity models. In this example instability of Kelvin wave propagating along the western US coast is simulated. As there is no forcing other than remote input of the Kelvin wave in this case, we should expect that the maximum speed occurs near the coast. Therefore, the numerical stability of the models mostly depends upon the representation of the boundary conditions. The first model is using the traditional reflection boundary conditions, while the second approach discussed above. In both cases the models were tuned to have the minimum possible dissipation necessary for numerical stability in each case. It turned out that the traditional model lacks

19

friction near the sharp corners of the boundary, where the instability develops primarily. As a result, this model needs an approximately 6 times larger friction coefficient than the second model, as a result we see much more mesoscale activity in the second model, Fig.2a, 2b.

Summary

We have discussed different forms of dissipation terms used in numerical ocean modeling, focusing our attention to the dual purpose of the p sence of dissipation in numerical models.

The physically consistent form of the dissipation term allow water equations cannot be derived from the dissipation term in the primitive equatic. As an alternative, we have chosen an phenomenological approach. We have formulated the viscous dissipation term, which preserves the integral constraints derived in the general theory of stratified fluids. Particularly, we discussed the influence of different forms of dissipation on the vorticity and potential vorticity budget.

If friction is needed for numerical reasons, the dissipation term should be parametrized in a physically consistent way. Violation of this rule may cause severe distortion of the numerical solution, despite the smallness of the friction coefficient.

A new approach of the numerical implementation of the no-slip boundary condition for a realistic coast line was developed. In this approach we have discretized the momentum equation preserving their intrinsic tensor structure both in the interior of the domain and on the boundaries. Thus, instead of discretizing boundary conditions for velocities, we discretize the components of the stress tensor on the boundaries. This discretization is designed to approximate not only the components of the stress tensor on the boundaries, but also the truncation error of the numerical scheme used in the interior of the domain.

It was demonstrated that this approach provides a more accurate approximation of the equations of motion near the boundary, which reduces the undesirable effects of dissipation and obtains a more valuable numerical solution.

headed by Dr. John Harrison. Special thanks to Dr. Detlev Müller, Dr. Steve Meyers and Dr. Mark Johnson for their comments and fruitful discussion.

APPENDIX A
Generation of the initial state for the shallow water flow

Assume that the flow is initially nondivergent, therefore the transports U and V can be expressed in terms of the streamfunction Ψ,

$$U = -\frac{\partial \Psi}{\partial y}, \quad V = \frac{\partial \Psi}{\partial x}, \quad \text{so that} \quad \frac{\partial U}{\partial x} + \frac{\partial V}{\partial y} \equiv 0.$$

The potential vorticity field is given by

$$\frac{\zeta + f}{H} = \frac{1}{H}\left[\frac{\partial}{\partial x}\left(\frac{1}{H}\frac{\partial \Psi}{\partial x}\right) + \frac{\partial}{\partial y}\left(\frac{1}{H}\frac{\partial \Psi}{\partial y}\right) + f\right] = \mathcal{Q}, \quad (A.1)$$

where $\mathcal{Q}$ is a specified function.

Taking the divergence of the momentum equations and using the property that the flow is nondivergent, one can easily see that

$$\frac{\partial^2}{\partial x^2}\left(\frac{U^2}{H}\right) + 2\frac{\partial^2}{\partial x \partial y}\left(\frac{UV}{H}\right) + \frac{\partial^2}{\partial y^2}\left(\frac{V^2}{H}\right) - f\left(\frac{\partial V}{\partial x} - \frac{\partial U}{\partial y}\right) =$$

$$= \frac{\partial^2}{\partial x^2}\left[\frac{1}{H}\left(\frac{\partial \Psi}{\partial x}\right)^2\right] - 2\frac{\partial^2}{\partial x \partial y}\left(\frac{1}{H}\frac{\partial \Psi}{\partial x}\frac{\partial \Psi}{\partial y}\right) + \frac{\partial^2}{\partial y^2}\left[\frac{1}{H}\left(\frac{\partial \Psi}{\partial y}\right)^2\right] - f\nabla^2 \Psi = \quad (A.2)$$

$$= \rho g\left[\frac{\partial}{\partial x}\left(H\frac{\partial(H-D)}{\partial x}\right) + \frac{\partial}{\partial y}\left(H\frac{\partial(H-D)}{\partial y}\right)\right],$$

where $D = D(x,y)$ is the depth of the basin, consequently $\eta \equiv H - D$ is the sea surface elevation.

Equation (A.1) and the last two lines of (A.2) form a coupled nonlinear elliptic problem for Ψ and H. Strictly speaking, this problem has multiple solutions due to nonlinearity. In the case when $g \to \infty$, the equations become uncoupled and linear, because $H \equiv D$. This is the incompressible state. We assume that the free surface elevation is small, $\eta < D$, and the solution we are looking for can be continuously transformed to the incompressible solution as $g \to \infty$. In this case the following algorithm may be proposed to solve the problem

21

(A.1)-(A.2): As the first approximation $H = D$ and the streamfunction Ψ is determined by solving the elliptic equation (A.1). Dirichlet boundary conditions are imposed for a closed domain. Then, for known Ψ and H the left hand side of equation (A.2) is calculated, and the surface elevation η is computed by solving the elliptic problem with Neumann boundary conditions. This solution is defined up to an arbitrary constant. The mean should be calculated and removed from the η field to preserve the total mass. After that the layer thickness is corrected

$$H^* = \alpha(D + \eta) + (1 - \alpha)H,$$

where H^* it the new approximation for the layer thickness, and the weight parameter $\alpha = 0.4...0.7$ is introduced to avoid overshooting. The new value of the layer thickness is substituted into equation (A.1) and the procedure repeats. Finally, after the procedure converges, it gives the Ψ and η fields, which produces the desirable potential vorticity field and the pressure field, which balances the Coriolis and centrifugal forces. It should be pointed out that the friction term has been ignored, therefore one should expect generation of boundary layers on the side boundaries. However, this problem is of minor significance because the original potential vorticity is specified in such a way that the flow near the boundary is very weak.

APPENDIX B
On the accuracy of the reflection boundary condition

Consider implementation of the no-slip boundary condition on a north-south wall. In this case, the coastal line goes through u-points and the u-component is set to zero, while the v-component is to be reflected. Suppose $v_{j,k}$ is the last v-point in the interior and $v_{j+1,k}$ belongs to the land. According to the reflection rule, the value of the v-component in the land point adjacent to the coastline is prescribed as $v^*_{j+1,k} = -v_{j,k}$ so that linear interpolation of the velocity component to the coast line always yields zero. The standard finite difference scheme is the approximation for the second derivative in the last interior point $v_{j,k}$ as follows:

$$\left.\frac{\partial^2 v}{\partial x^2}\right|_{j,k} = \frac{v^*_{j+1,k} - 2v_{j,k} + v_{j-1,k}}{\Delta x^2} = \frac{-3v_{j,k} + v_{j-1,k}}{\Delta x^2}, \qquad (B.1)$$

where Cartesian coordinates are used for simplicity.

Obviously,

$$v_{j+\frac{1}{2},k} = v_{j,k} + \left.\frac{\partial v}{\partial x}\right|_{j,k}\frac{\Delta x}{2} + \frac{1}{2}\left.\frac{\partial^2 v}{\partial x^2}\right|_{j,k}\left(\frac{\Delta x}{2}\right)^2 + \frac{1}{6}\left.\frac{\partial^3 v}{\partial x^3}\right|_{j,k}\left(\frac{\Delta x}{2}\right)^3 + \dots \quad ,$$

and

$$v_{j-1,k} = v_{j,k} - \left.\frac{\partial v}{\partial x}\right|_{j,k}\Delta x + \frac{1}{2}\left.\frac{\partial^2 v}{\partial x^2}\right|_{j,k}(\Delta x)^2 - \frac{1}{6}\left.\frac{\partial^3 v}{\partial x^3}\right|_{j,k}(\Delta x)^3 + \dots \quad ,$$

and, therefore,

$$\frac{2v_{j+\frac{1}{2},k} + v_{j-1,k} - 3v_{j,k}}{(\Delta x)^2} = \frac{5}{8}\left.\frac{\partial^2 v}{\partial x^2}\right|_{j,k} - \frac{7}{48}\left.\frac{\partial^3 v}{\partial x^3}\right|_{j,k}\Delta x + \dots \quad .$$

Taking into account that $v_{j+\frac{1}{2},k} = 0$ because this is the value of the v-component on the boundary, one can easily see that expression (B.1) approximates $\left(^5/_8\right)\left(\partial^2 v/\partial x^2\big|_{j,k}\right)$ instead of $\partial^2 v/\partial x^2\big|_{j,k}$. Thus the second derivative of v-component is underestimated in the points nearmost to the boundary.

REFERENCES:

Bleck, R and D. Boudra, 1981, Initial testing of the numerical ocean circulation model using a hybrid (quasi-isopycnic) vertical coordinate, *Journ. Phys. Ocean.*, **11**, 755-770.

Farge, M. and R.Sadornay, 1989, Wave-vortex dynamics in rotating shallow water, *Journ. Fluid Mech.*, **206**, 433-462.

Gent, P, 1993, The Energetically Consistent Shallow Water Equations, *Journ. Atmosph. Sci.*, **50**, 1323-1325

Gent, P.R. and J.C.McWilliams, 1990, Isopycnal Mixing in Ocean Circulation Models, *Journ. Phys. Ocean.*, **20**, 150-155.

Haynes, P.H. and M.McIntyre, 1987, On the evolution of vorticity and potential vorticity in the presence of diabatic heating and frictional or other forces, *Journ. Atmosph. Sci.*, **44**, 828-841.

Haynes, P.H. and M.McIntyre, 1990, On the conservation and impermeability theorems for potential vorticity, *Journ. Atmosph. Sci.*, **47**, 2021-2031.

Landau, L.D., Lifshitz, E.M., Theoretical Physics, v. VI, Hydrodynamics. /Moscow, *Nauka*, 1988.

Obukhov, A.M., 1962, On the dynamics of a stratified fluid. *Dokl. Akad. Nauk SSSR*, **145**(6), 1239-1242; English Transl. in *Soviet Physics, Dokl.* **7**, 682-684.

Sadornay, R., Basdevant, C., 1985, Parametrization of subgrid scale barotropic and baroclinic eddies in quasigeostrophic models: the anticipated potential vorticity method, *Journ. Atmosph. Sci.*, **42**, 1353-1363.

Shcär and Smith, 1993, Shallow water flow past isolated topography. Part I: Vortex production and wake, *Journ. Atmosph. Sci.*, **50**, 1401-1412.

Figure Captions

Fig. 1a. Dipole interacts with sea-mountain. Potential vorticity field is shown. Concentric dashed circles represent the sea-mountain. Friction term (1) is used.

Fig. 1b. The same ase Fig. 1a, but friction term given by (2.2).

Fig. 1c. The same ase Fig. 1a, but friction term given by (2.3).

Fig. 1d. Difference between the potential vorticity fields on Fig. 1b and Fig. 1a.

Fig. 1e. Difference between Fig. 1c and Fig. 1a.

Fig. 2. Comparison of the two models. Layer thickness and velocity field are shown. a: Method of reflections is used to implement the boundary conditions. b: The new implementation of no-slip boundary conditions is used.

t=0.80　　　　　　　　　t=1.00

t=0.35　　　　　　　　　t=1.30

t=0.00　　　Fig. 1a　　　t=2.00

t=0.80

t=1.00

t=0.35

t=1.30

t=0.00

Fig. 1b

t=2.00

t=0.80

t=1.00

t=0.35

t=1.30

t=0.00

t=2.00

Fig. 1c

t=0.80

t=1.00

t=0.35

t=1.30

t=0.00

t=2.00

Fig. 1d

t=0.80 t=1.00

t=0.35 t=1.30

t=0.00 Fig. 1e t=2.00

a) Reflection boundaries

b) New method

h(m)

200

180

160

140

120

100

80

Contour interval 5 m

40 cm/sec
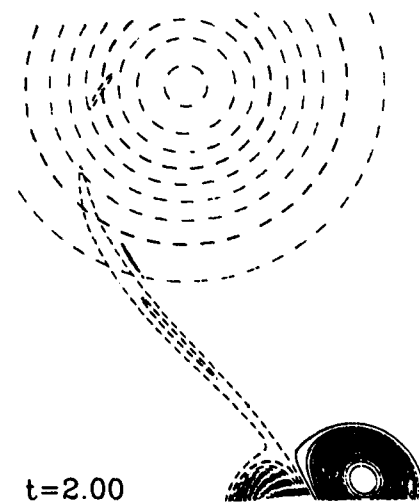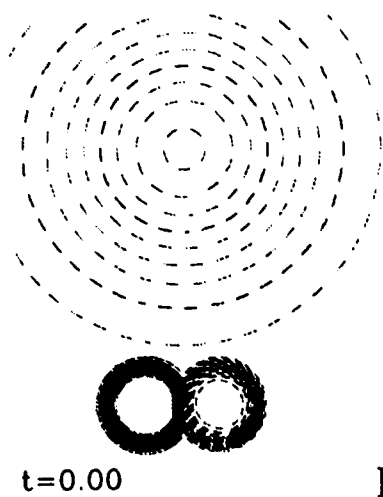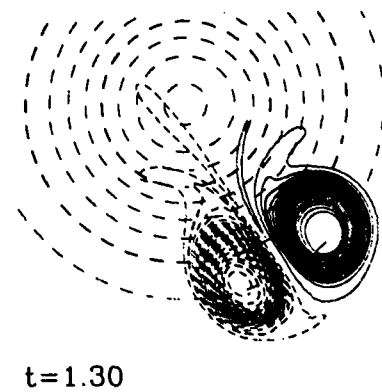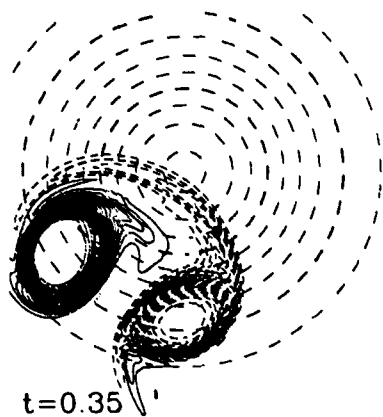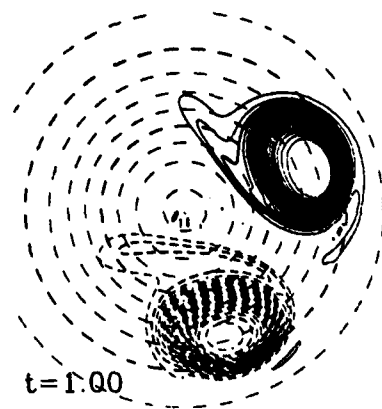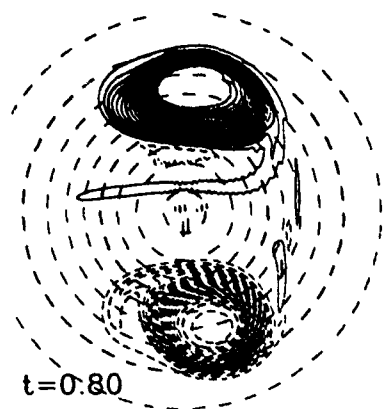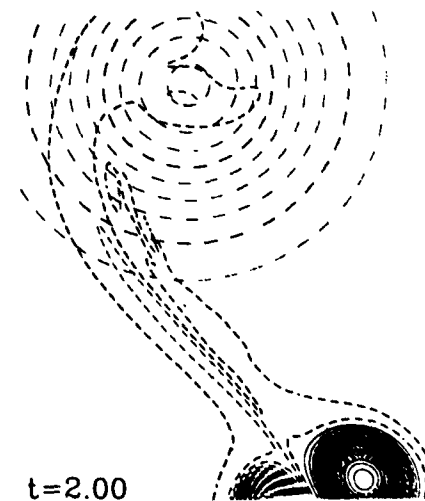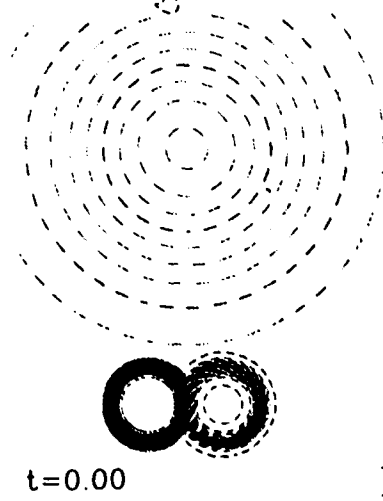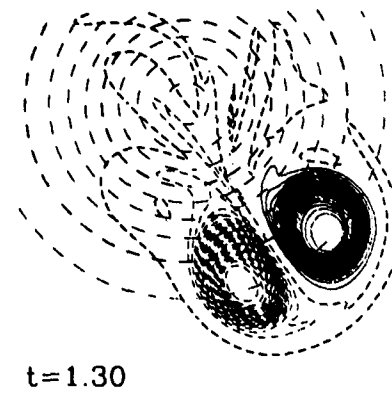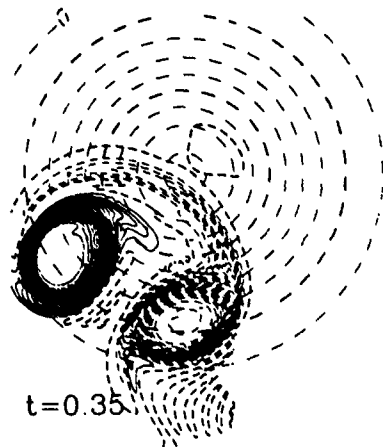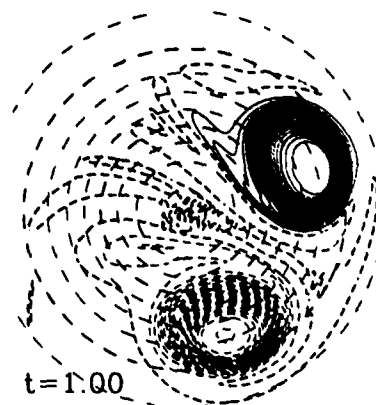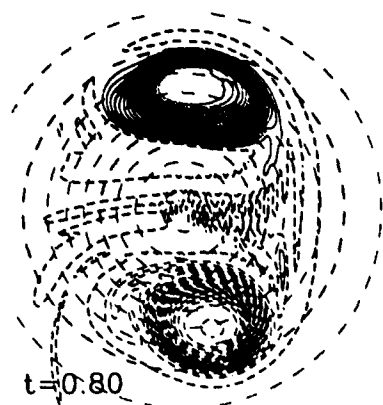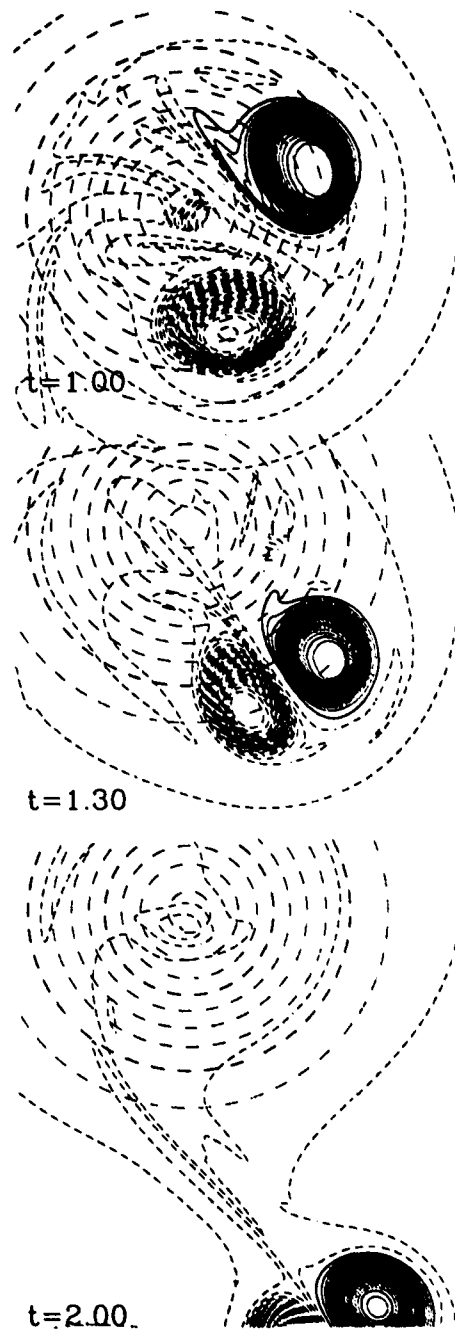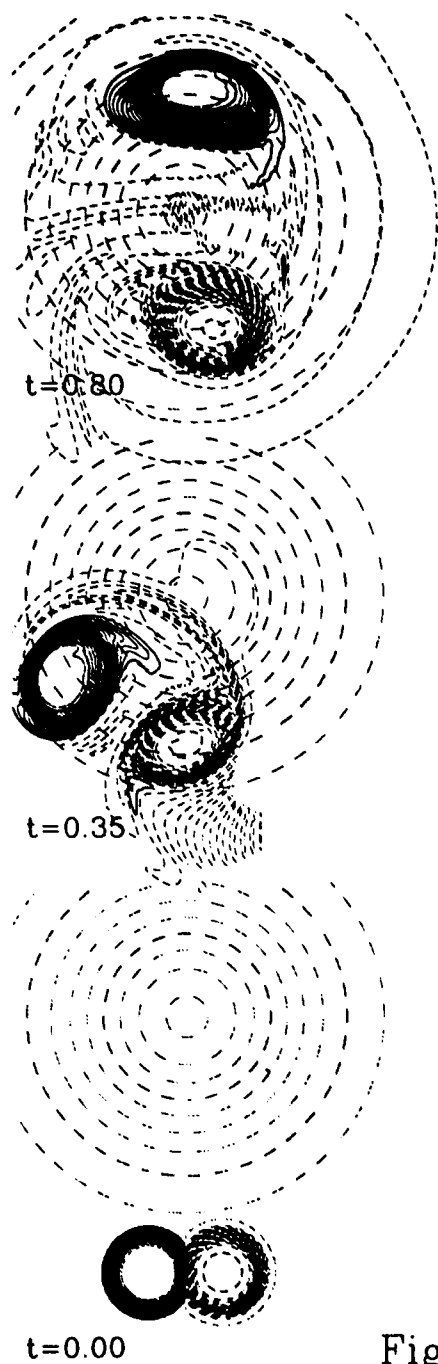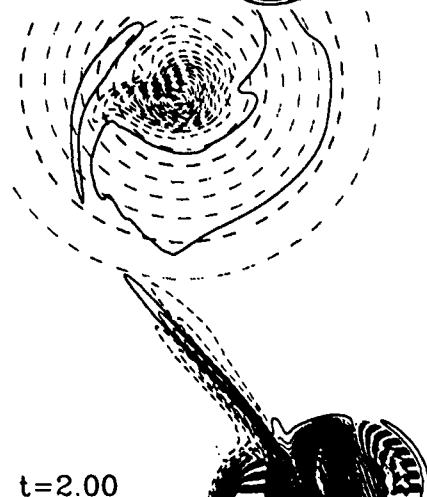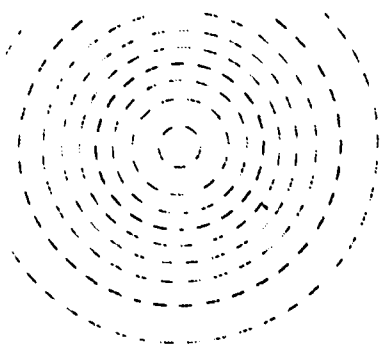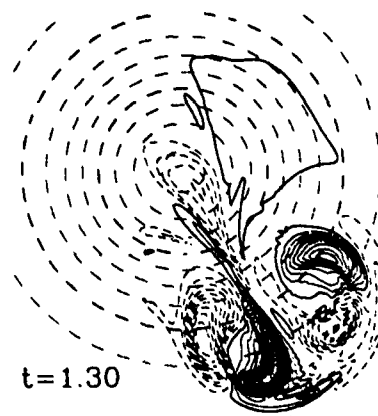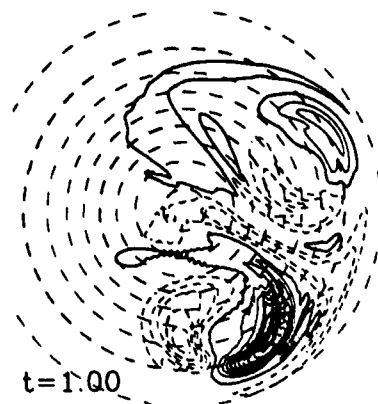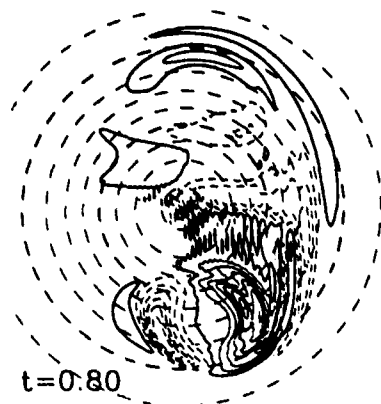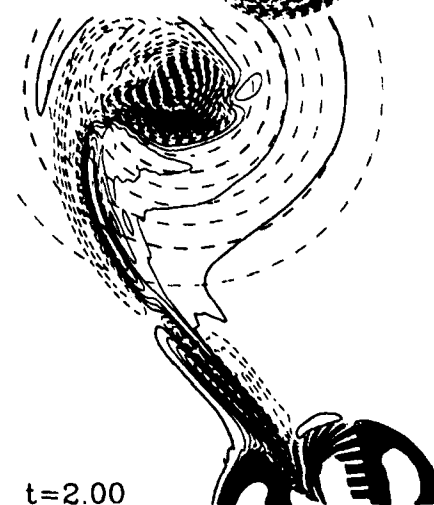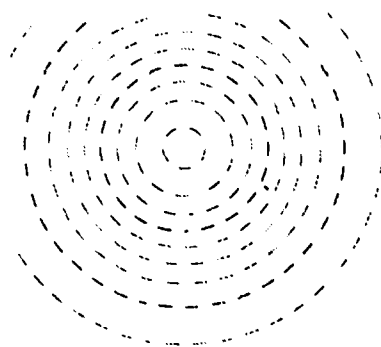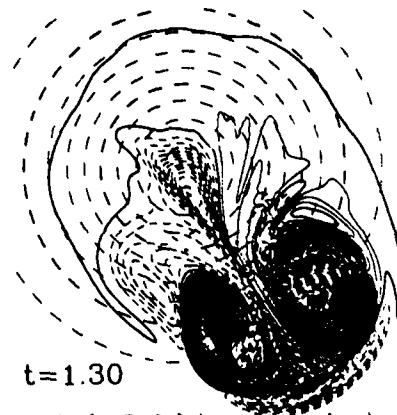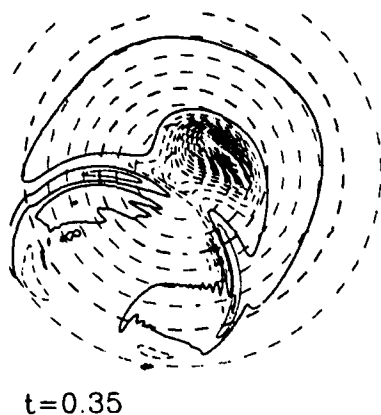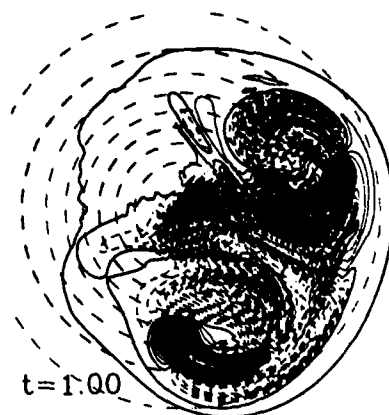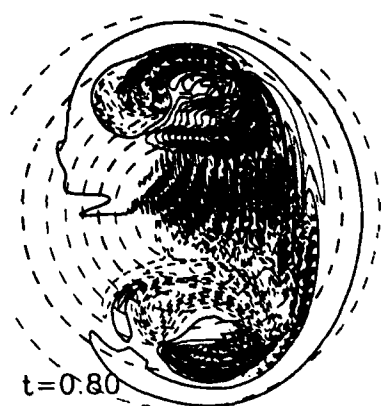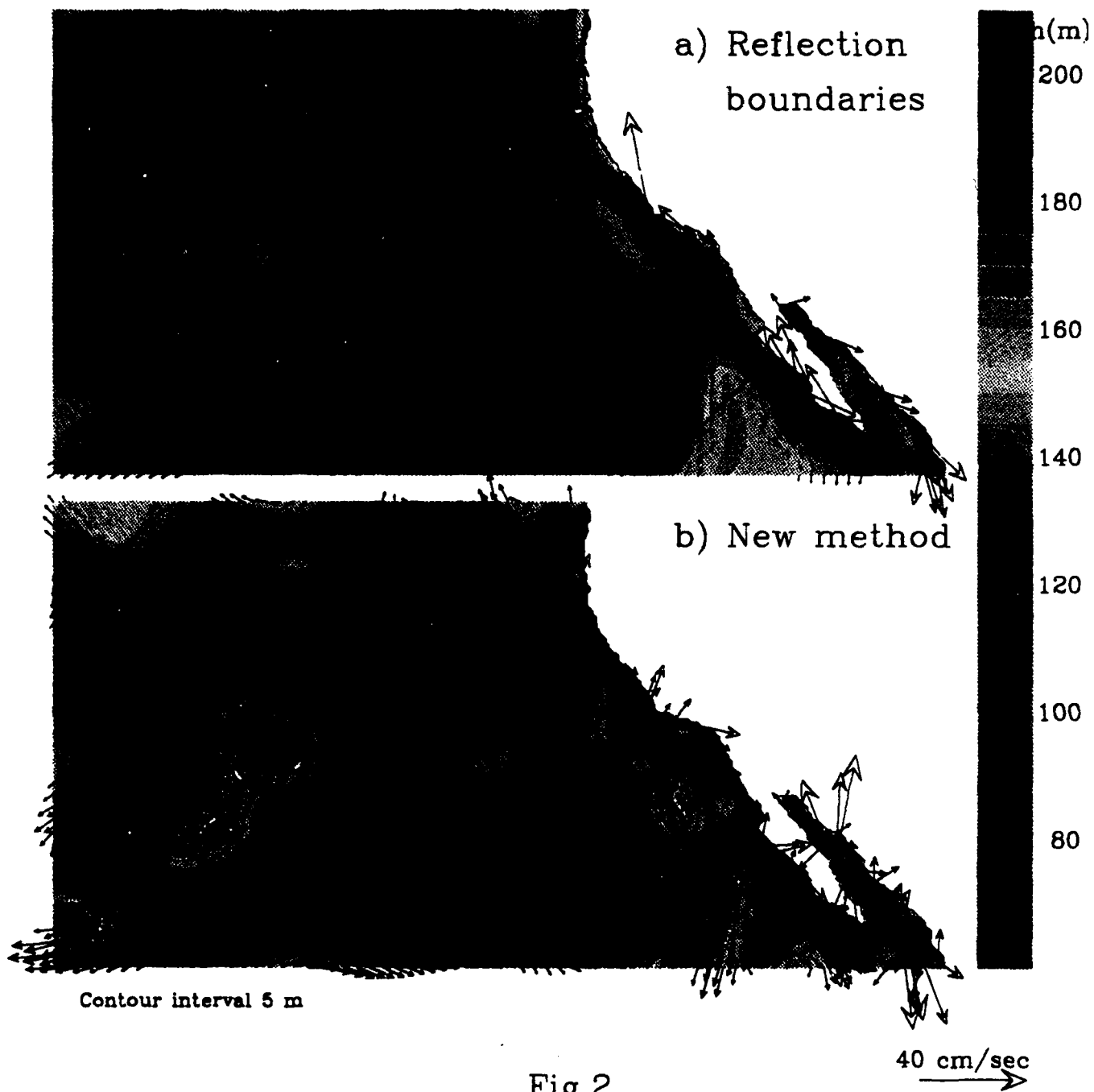
Fig.2

TASK C: SSAR DEVELOPMENT

AUTEC TEST CRUISE #2

The second at-sea test of the SSAR system was conducted at the AUTEC Range at Andros Island in the Bahamas from August 18-27. The cruise report describing the field activities is included as Appendix A. The purpose of the test was to verify the SSAR's ability to receive and process 70 Hz M-sequence signals and to compare the results of a surface-suspended acoustic array with an identical array moored on a subsurface mooring. To conduct this test, a Snubber SSAR was deployed with its normal processing system plus a hard disk to record the raw data. The lower portion of a second SSAR was deployed on a subsurface mooring, again with a hard disk for raw data storage. A ship-lowered source then transmitted a total of seven, 7-minute long, 70 Hz M-sequence signals. All data were successfully collected with excellent SNRs. Processing of these data is ongoing. A data summary will be included in the next quarterly report. Figures C-1 through C-4 are examples of the acoustic data.

A second objective of the AUTEC cruise was to repeat the USBL tests performed on the first AUTEC cruise. The USBL array was modified slightly to improve SNR and the WATT pinger was mounted so that it would not cause high frequency wobbles at the array. A series of USBL calibrations were run relative to the AUTEC Range acoustic tracking system on August 26. All data were successfully recorded, but no analysis has yet been performed. Results of this test will be included in the next quarterly report.

ATLANTIC TEST CRUISE

In August ARPA suggested that WHOI deploy an SSAR buoy to monitor a pair of underwater explosions that were scheduled for October 3 and 4, 1994 off the coast of Portugal. These explosions were to be conducted by the Combo Group at the Dublin Institute of Advanced Studies in Ireland for the purpose of studying the earth's interior. It was suggested that we take advantage of this cruise to test the long range performance of the SSAR using a ship-lowered 70 Hz source similar to the short range tests conducted in August at the AUTEC Range. After analyzing the acoustic paths between Portugal and the East Coast, it was decided to conduct the cruise out of West Palm Beach using the AUTEC vessel, the Rover, which could both deploy the SSARs and the 70 Hz source. (Figure C-5 shows the bottom topography for a great circle path between Portugal and West Palm Beach). The cruise plan and cruise report are included in the report as Appendices B and C.

The cruise began on October 1. SSAR #1, modified to record low frequency signals from the underwater explosions, was deployed on October 2 about 250 nautical miles offshore West Palm Beach. SSAR #2, set up in the normal way to record and process 70 Hz M-sequence signals, was deployed on October 6 about 160 nautical miles east of Andros Island. The 70 Hz source was deployed at ranges of about 60, 120, and 190 miles from SSAR #2 on October 6 and 7 and a total of 12 transmissions were made. SSAR #1 was recovered on October 7 and SSAR #2 was recovered on October 8. Due to circumstances

beyond our control, the underwater explosions were not deployed so we arranged several SUSS charge drops on October 7 prior to SSAR # 1 retrieval. The data from this recent cruise is being evaluated and will be discussed in the next quarterly report.

FABRICATION AND TESTING

Fabrication of the operational SSARs in continuing. This task has been delayed by the preparations for and conduct of the Atlantic and Pacific tests, but we anticipate completion of the task by the end of the year. Figures C-6 through C-9 show various elements of the SSAR system). All of the components are either in house or have been ordered and will be delivered shortly. Tests of the coil cord assemblies for use in the Snubber and Standard hoses are ongoing. The initial test was terminated at 3 million cycles with no damage apparent to the coil cord. The coil cord design was used on the October test cruise and post-cruise examination of the coil cords showed damage to some of the conductors. A modified design with a stronger tension element is being ordered for the operational units.

The Atlantic Test Cruise also provided an opportunity to compare several techniques of attaching the hydrophones to the acoustic array strength member. Analysis of these data is not complete, but a simple urethane block mounting arrangement appeared to offer the best noise rejection and least mechanical complexity. Further evaluations will be performed during the Pacific test deployments.

The Design and Test Report has been re-scheduled for delivery at the end of December. This change was necessitated by the requirements for the AUTEC, Atlantic, and Pacific test cruises.

OTHER TASKS

Preparations are underway for the Pacific Test Cruise. The Pacific Test Cruise Plan is included as Appendix D. Three SSARs are being readied for this test with the shipment from WHOI planned for November 2. Processing and analysis of data collected on the AUTEC and Atlantic test cruises is ongoing and results will be included in the next quarterly report. We are also working closely with ARPA on program definition for FY95.

The low power receiver design task has started and a preliminary design is complete. A prototype of the analog to digital converter portion of the low-power receiver has been constructed and tested. It uses a 24 bit sigma-delta converter which is optically isolated from the buffer portion of the system in order to reduce noise at the front-end. Several designs for the input stage before the A/D are being considered. The requirements are that it be very low-noise and have integral high-pass filtering. An existing design is being modified for this purpose and final testing of the front-end should be complete in a few weeks.

The next stage of development is fabrication of PC boards for the buffer section of the receiver. We expect that the hardware will be completed and performance testing done by the end of January.

LIST OF FIGURES AND TABLES

APPENDICES

Figure C-1: Time series signal recorded by the drifting
SSAR during the August 1994 AUTEC test cruise.
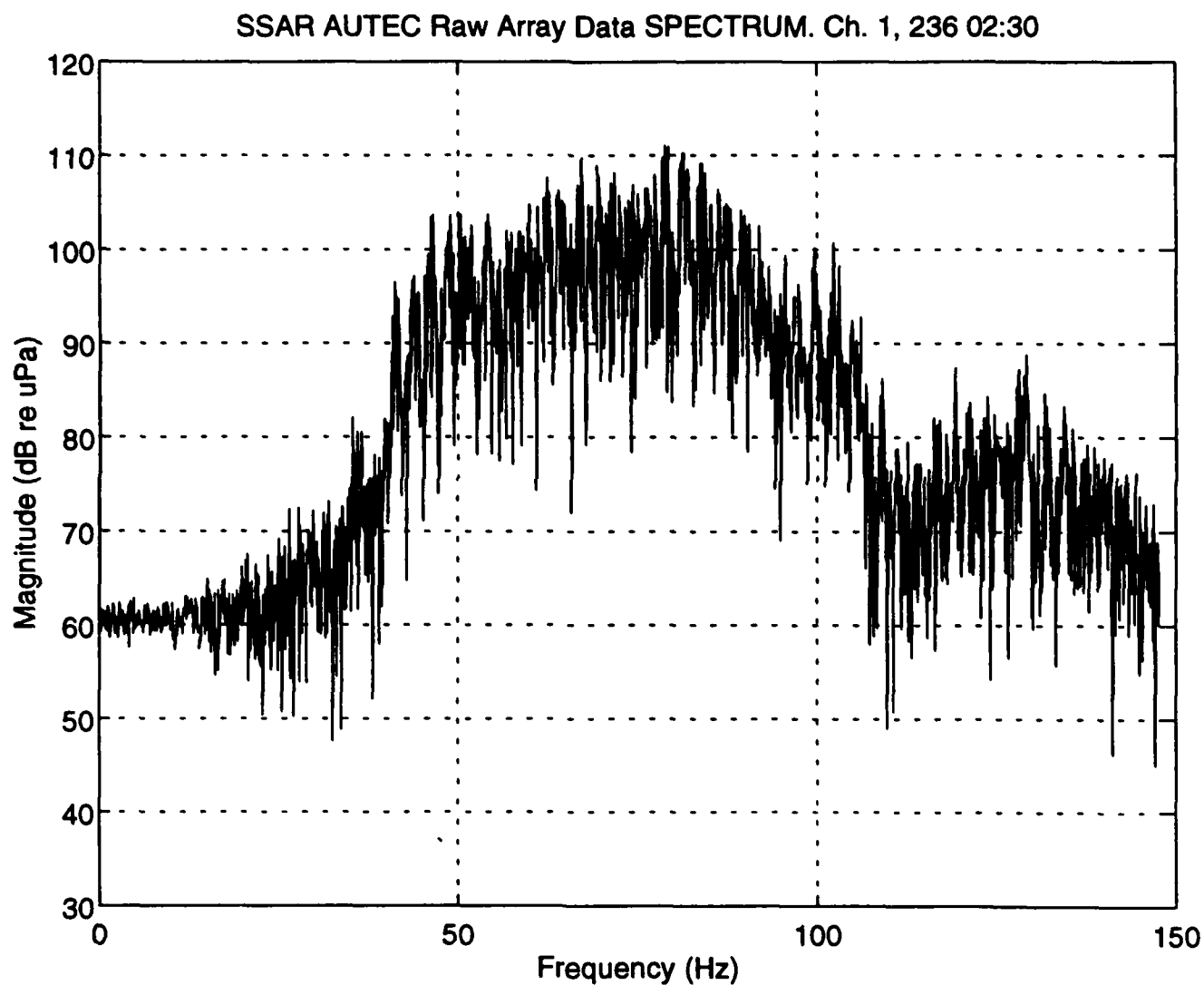
Figure C-2: Spectrum of 70 Hz signal recorded by the drifting SSAR during the August 1994 AUTEC test cruise.
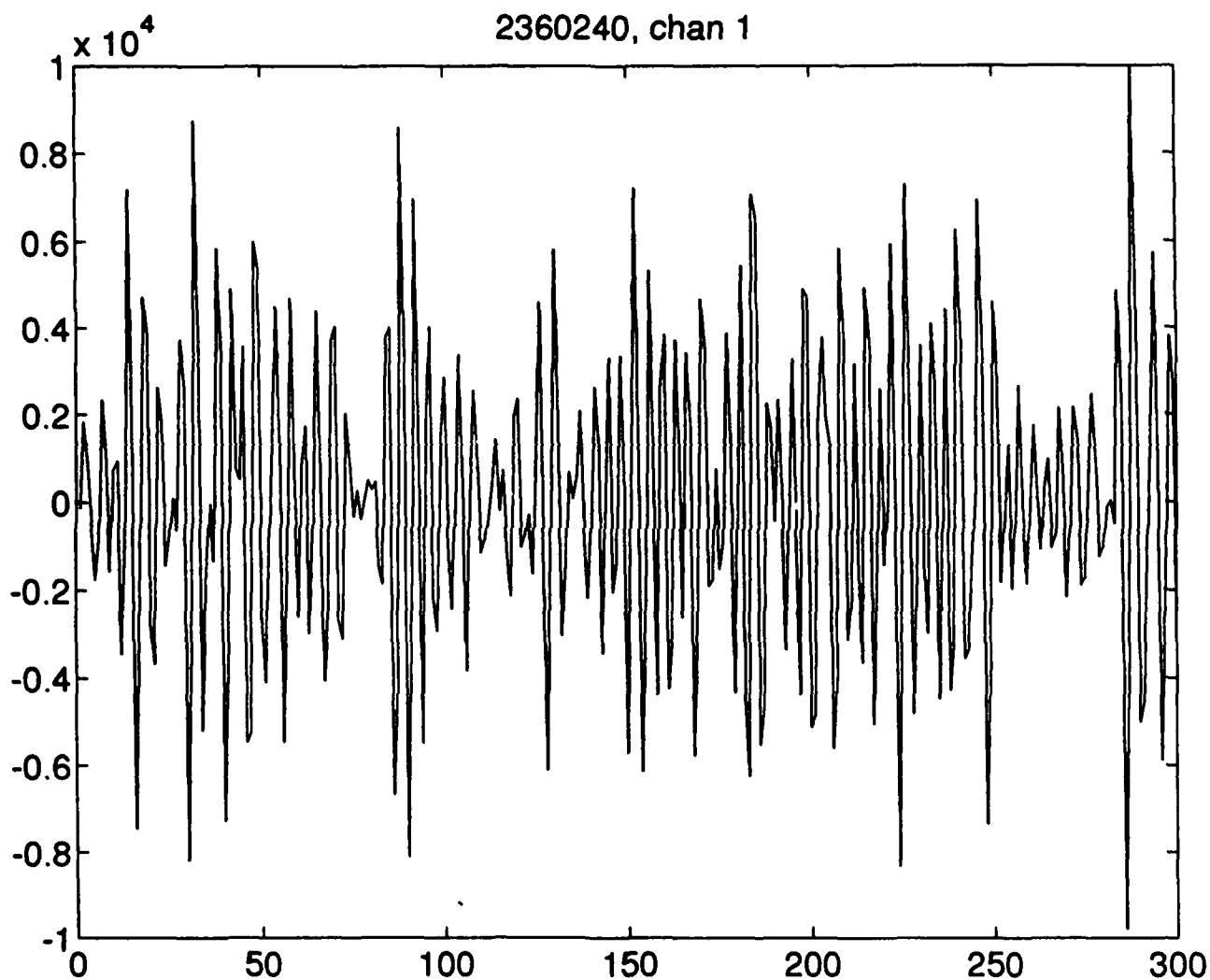
Figure C-3: Time series signal recorded by the moored SSAR
acoustic array. X-axis is samples where the
sample rate is 300 samples/sec. Y-axis can be
compared to Figure C-1 by dividing magnitude
by 1.31×10^4

2360240, chan 1
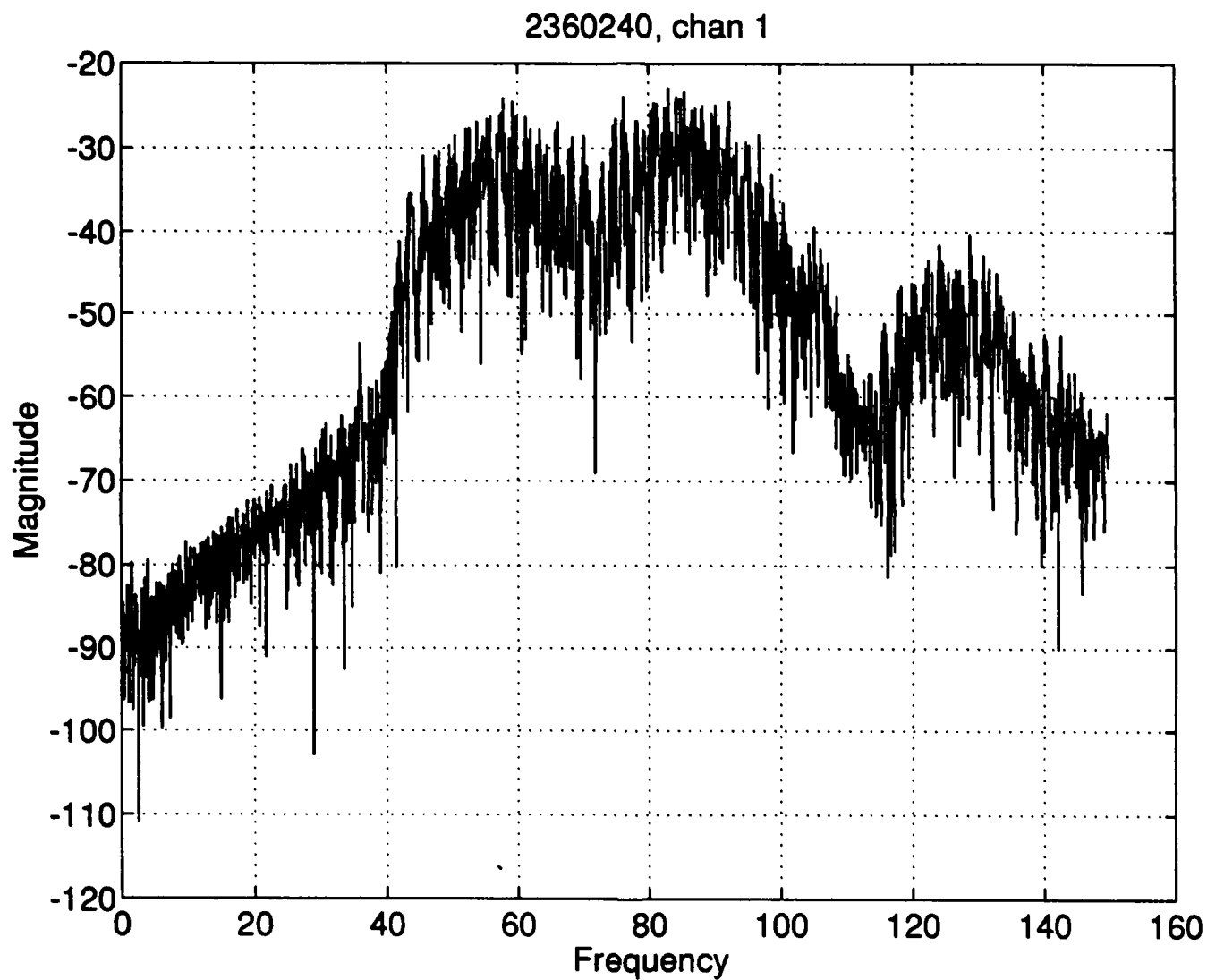
Figure C-4: Spectrum of 70 Hz signal recorded by the moored SSAR acoustic array. Note that Y-axis magnitude can be compared directly with Figure C-2 by adding 135 dB.
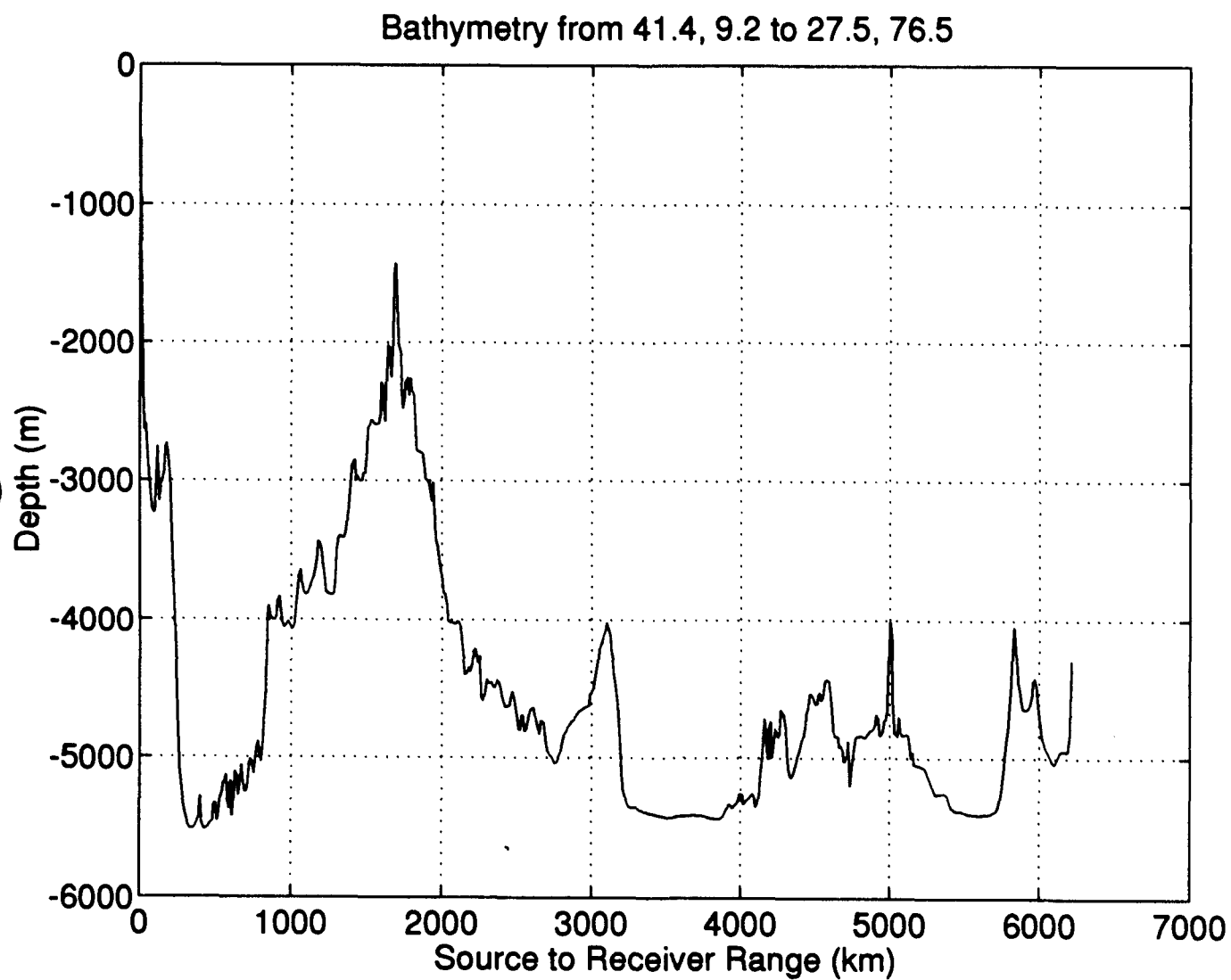
Figure C-5: Bottom topography between Portugal (explosion site) and West Palm Beach (SSAR deployment area).
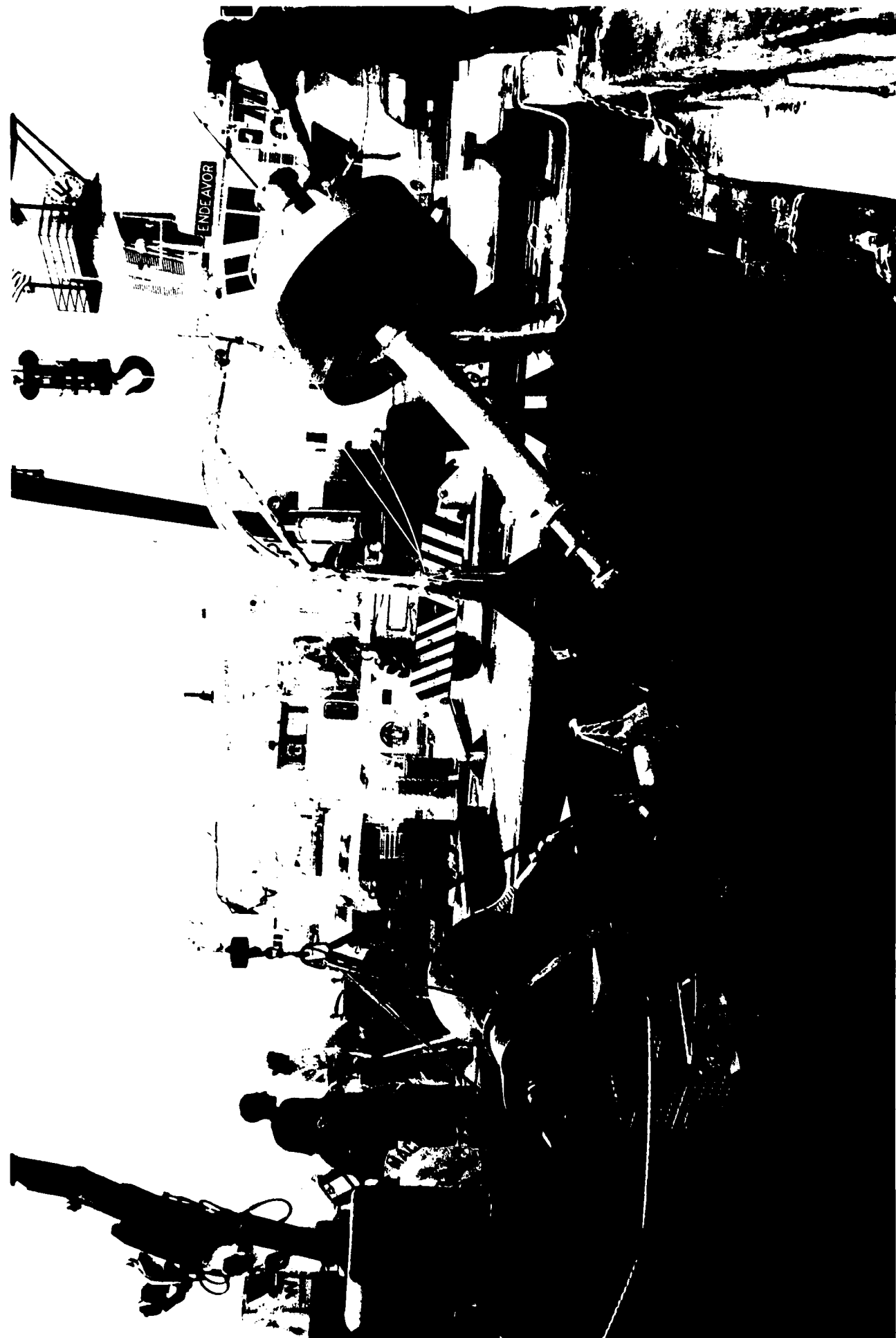
Figure C-6
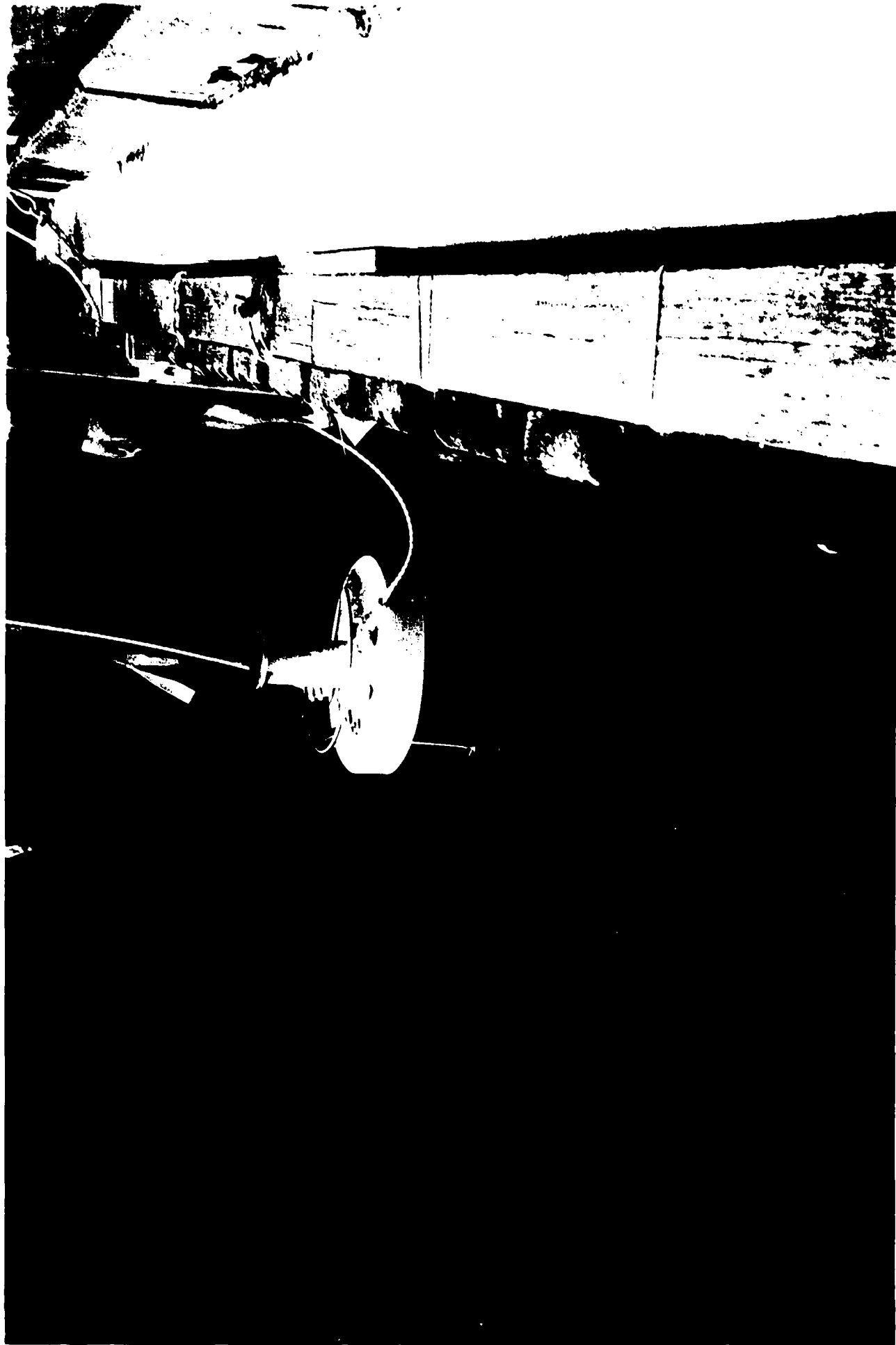
Figure C-7:   Shows SSAR Buoy during Wet test.   Only a portion of normal tension is applied to the buoy as shown.

Figure C-8

Figure C-9

APPENDIX A

Cruise Report for AUTEC SSAR Experiments
August 18 to August 27
Woods Hole Oceanographic Institution
AUTEC Test Number: 003W003

Thursday August 18

John Kemp and Neil McPhee arrive at Andros Island and begin mobilization.

Friday August 19

Tom Austin and Lee Freitag arrive Andros Island.

0900 meeting at CC building with technical support staff and R/V Range Rover crew. Test parameters and schedule confirmed. Pinger frequencies, tracking schedule and MAXI-SATS setup discussed. Real-time tracking display will be available using the PARGOS system aboard the vessel.

Schedule for ship time will be broken into three legs: (1) deployment of fixed array north of weapons range W3/W4 mooring, (2) complete test of SSAR running all system components on an accelerated, half-hour schedule (3) test of USBL tracking system running continuously. After (2) is accomplished the fixed array mooring will be retreived. The continuous USBL test will be done on the northern (W1/W2) range so the fixed array will be pulled to avoid a second trip (2 and a half hours) to the southern range.

The moored array is to be put in on Saturday so that it can be placed over the stern. After the MAXI-SATS is installed and wired the stern cannot be used for mooring deployment. Scheduled departure is 1400 with return before midnight.

Friday PM

Computers and equipment unpacked and set up for system testing. Mooring equipment and other gear unpacked from container.

Mooring array and electronics testing is first priority. System is configured for a half-hour schedule. On the hour and thirty minutes past the hour the system will wake-up and collect 10 minutes of data from the array (6 channels at 300 Hz, 16 bits per sample). Data is moved to hard-disk following the sampling period. Disk size is 1 Gbyte. Total data collection per day is 48 periods times 2 Mbyte or 96 Mbytes total. System capacity is thus 10 days.

Array tap est is performed. All elements OK. Array mounting configuration is as from the manufacturer (C & M Technology) with one exception. Tom Austin suspects that the PVC tube holding the hydrophone element may squeak if tension is changed on the cable. While

the mooring should experience little or no tension change, one of the mounts is changed so that the PVC tube is attached using an elastic bandage adjacent to the part of the cable that is wrapped with tape.

Electronics package for fixed array is setup to run all night on the final schedule.

Bruce Einfalt from PSU arrives on 6 PM flight from WPB.

Saturday August 20

Final loading of the R/V Range Rover for fixed array deployment is completed. Electronics are loaded into pressure case and purged. Battery check: main 15.5 V, tomo 22.12 V no load.

At 0230 the Range Rover departs for W3/W4 mooring area with John Kemp and Neil McPhee to place the mooring approximately one mile from the site where the source will transmit.

Checkout of tomography DSP code: the system crashes under certain circumstances. Data sent to PSU appears to process fine on their development system but causes the target system to crash. The problem is fixed after upgrading the DSP code to the most recent PSU version and loading a new (reversed) replica vector. The old replica vector had been from an earlier version of the software delivered a few weeks previously from PSU.

Tomography processing system is tested end-to-end with the m-sequence generator tied through an attenuator into the analog front-end of the tomography receiver. Processing on the DSP takes 626 seconds. Final checks are done by running the same data on the development PC and on the PSU Sun workstation. All processing yields the same results.

R/V Range Rover returns around midnight after placing fixed array without any problem. Placement of WATT pinger (below the array) is 589 meters below the surface.

Sunday August 21

A portion of the deck changes on the Range Rover are done to accomodate the MAXI-SATS source off the stern and the SSAR deployment off the side.

The next phase of the experiment will begin Tuesday at 1500 with the Range Rover underway to W3/W4 Deep Moor.

A new m-sequence generator from Michigan with internal oscillator has been brought down by PSU. This will be used as the primary source and the older unit kept as a backup. Front panel parameter settings include: frequency 75 Hz, Phase 17, seq law 2033, cycles 002, PHS modulation.

Interfaced and tested as with older unit.

Signal generator start synch is a low-going transition of a pulse two cycles long (0.0267 seconds).

The computer system which is to be used to record the start time of the m-sequence generator is tested using a GPS antenna mounted on the roof of the lab. The system is essentially a SSAR topside computer with a small program that watches for the synch pulse on the m-sequence generator and then records the GPS time. A counter running at 32 kHz is reset every second by the 1 PPS signal from the GPS. This is used to keep high resolution time between the one second GPS pulses. This will be installed in the MAXI-SATS van and will run during source transmissions.

Final time delay estimates for USBL done. Total distance from pinger to receive array is 535.8 meters. Average sound speed from XBT done on Saturday at W3/W4 site is 1530 meters/seconds over the path from the surface to the USBL receiver.

Source id numbers for the experiment are set to 1 for the first half-hour transmission and 0 for the second. Two ids are required because the system is not normally run on less than a one hour schedule.

Carter Ackerman from PSU arrives.

Monday August 22

Final loading of Range Rover completed. Deck configuration includes six bunk berthing van, range user shack, SATS van and winch, inverter system and battery trailer, backup rubber-tired generator, Pengo winch for mooring work and Hiab crane aft of starboard deck opening for handling SSAR components.

New m-sequence generator is installed in MAXI-SATS van and tested with source.

Buoy placed outside with system electronics installed. Monitor cable run inside and a test cable connected between the buoy and the bottom electronics package in the lab. Argos and GPS tested.

Compass calibration done using rotating fixture brought from WHOI. Test is done in area between labs and port office at least 50 yards from the nearest structure. Data is taken at 10 degree increments and stored for use in a look-up correction table.

Tuesday August 23

Final source configuration file has sound speed set to 1530, lat 24.3205, long 282.3988.

1500   R/V Range Rover departs for mooring site.

System is operating during transmit. As the vessel moves south
the SSAR correctly estimates the distance to the mooring using the
GPS receiver and adjusts the data collection time based on the
computed travel time. All components appear to be operating correctly.

1755   On-site about 2000 yards from the Deep Moor. Seas are about 1-2 feet.
Wind light 5-7 knots.

1815   Buoy and snubber hose over the side.

1910   All E/M cable out. Connecting subsea case and acoustic array.

1930   Bottom computer boots up at 23:27:40 GMT on command from surface verifying
the connection between top and bottom through hose and E/M cable.

1952   Bottom electronics case, array and WATT pinger are all over the side.
The 200 lb weight is dropped.

Range coords for buoy: 7446, -15004 (yards)

Argos update received from buoy.

Buoy drift is to the south east at 0.1 to 0.2 knots.

2045   Range Rover tied up to W3/W4 mooring. Buoy is visible on radar
at 1.8 nmi, bearing 088. Seas very calm.

Source deployed over the stern with WATT pinger.

2100   SATS is ready so first source transmission begins.

2115   Final rigging for quiet ship completed. Entire ship is powered
down (including the head) or running on the inverters. The
vessel is amazingly quiet. Due to currents and low wind the ship
is not pulling at the mooring but sitting alongside it.

Source transmissions take place on the half-hour and hour for
seven minutes each. The m-sequence generator is started 27 seconds
before hand and then reset at time zero. Precise start time is
recorded by the GPS timing system. GPS log files are 2360049.log and
2360121.log

2340   Range FINIX called.

2400   Final transmission. Buoy is about 5000 yards from the vessel.

Wednesday August 24

0100   Engines back on, SATS on deck, preparing for SSAR recovery.

0330   SSAR on deck, recovery complete. Acoustic array below bottom pressure
case has required about 1.5 hours to pull since it cannot be put
on the winch.

Decision is made to wait for first light to begin fixed array recovery.

Data files on buoy hard disk examined. All files from experiment are
present. Down-loaded set from 2230 (0230 GMT). Very strong m-sequence
signal present, signal to noise ratio is very high. Buoy and bottom
electronics are turned off after several other data sets are
examined and appear fine.

0630   First light

0700   On station at moored array location.

0715   Release fired. Subsurface float up.

0727   Glass balls at the surface.

0737   Glass balls recovered.

0810   Pulling in acoustic array.

0818   Pressure case on deck.

0833   Subsurface float on board.

1100   At AUTEC base.

Wednesday PM

Moored array data is checked. One set downloaded from electronics package is from source transmission period, one from no-signal time (midnight on Monday). Ambient noise is less than 70 dB re uPa in no-signal data. Signal to noise ratio in other data is very high though spectrum differs from SSAR array slightly.

SSAR is configured for continuous track test for final testing of USBL system. System will run at 2 seconds rep rate and run about 90 seconds before pausing to write data to disk.

Examined USBL data from Tuesday experiment. Noticed lowered SNR during some data collection periods (less than 20-25 dB). After looking at raw waveform data it appears that some signal cancellation is occuring in the PSK signal. This occurs at some geometries. Of three data sets examined the cancellation is present in two. This phenomena was not observed during the first AUTEC test and is assumed to be caused by reflections at the buoy from the WATT pinger pressure case and the buoy pressure case. The WATT pinger was mounted 90 degrees from a line projected through the USBL pinger and the SSAR buoy pressure case.

In order to make sure that the pinger signals are correct for the second test the decision is made to mount the pinger down at the end of the pressure housing right above the hose flange.

Thursday August 25

A mounting bracket for the pinger is fabricated. It holds the pinger off the centerline of the buoy about 18 inches.

Final dockside testing reveals a problem in the signal processing for the USBL system. The delay caused by having to fabricate the pinger mount and the uncertainty about the source of the processing problem lead to the decision to perform the test on Friday. The test is to be done at the W1/W2 area which is one hour from the base.

Processing problem is found to be a demodulation frequency setting. The system is fixed and retested.

Carter Ackerman and Bruce Einfalt depart Andros Island.

Friday August 26

0600   Prepare for departure

0700   Under way to 24 41' 18", 77 36' 48"

0800   On site. Perform drift check.

0830   1 mile from range center, bearing 275 from vessel
        Buoy over the side.
0825   Track confirmed on buoy. Vessel is drifting at about 0.9 knots

0900   E/M cable is out, preparing for bottom pressure case launch.
        Check of comms from bottom to surface done.

0920   Pressure case in

0927   WATT Pinger and weight in. WATT is 5m below bottom pressure case.

0940   Moving closer to get Argos updates to check operation.

0945   Drift of SSAR is to the northeast.
        No Argos updates observed.
1000   Manoever for buoy pickup.

1020   Buoy on deck for checkout. Topside running ok, no data coming from
        bottom.
1030   Hose and subsurface float on deck.

1052   Bottom case on deck.

1100   System is stopped. Possible disk problem with turn-on, turn-off
        sequence. Simplified sequence and restarted system. Pulled electronics
        from case to do tests. Unsure of source of problem the disk is setup
        to be left on for the duration of the test.

1415   Buoy is out and bottom case ready to be deployed. However, acknowledgements
        from buoy to bottom case are not present. While the only comms for
        this test are the pinger triggers and this does not require the
        buoy to do anything, Neil McPhee goes out in the Avon to reset the
        topside system before the bottom case is launched. No change is
        observed but the decision is made to launch the bottom pressure case
        anyway since there is a high probability that the pinger triggers are
        working and we are just missing the feedback.

1445   Subsea case, WATT pinger and weight are launched.

1500   Range track started. Avon sent out to pull the buoy in order to get
        larger offsets from bottom to surface than otherwise will be present
        due to currents.

1505   Avon pulling buoy out to greater than 50 meters. Angle of buoy is up to
        30 degrees.

1506   Slowing Avon down, buoy tilt now about 15 degrees. Range track data
        observed on PARGOS is somewhat noisy.

1515   About one-half circle complete.

1525   Let buoy free. The system settles back very quickly.

1530   FINIX. Range tracking stopped.
        Seas 3 feet, occasional waves to 5 feet.

1545   Recovery started. When buoy is pulled on board the pinger is found to
        be running at the programmed rate which means the system is operating
        correctly.

1615   Subsea case on deck.

1625   WATT pinger on board.

1626   Weight on board.

1630   Connected to bottom case for checkout. All data present. SNR looks
        very high (22 dB), case pitch and roll relatively mild.

1730   Dockside. Tom Austin departs.

2000   All gear in range user shack packed and moved to shore lab. Heavy
        gear to be moved in the morning. Hose drained to facilitate packing
        and moving.

Saturday August 27

Deck gear and buoy removed from Range Rover. Container packed. Air shipment (5 pieces)
packed and taken to shipping dept. Range data collected from CC building.

1700   John Kemp, Neil McPhee and Lee Freitag depart Andros Island.

APPENDIX B

<u>Atlantic Test Cruise Plan</u>

At-Sea Schedule for Monitoring Underwater Explosions and Performing Source Test

September 29th

WHOI science party travels to WPB

September 30th

1000   R/V Ranger arrives in WPB

      WHOI equipment arrives via truck at WPB

      Loading commences of buoys, Pengo, Hiab and van.

October 1st

0700   Finish loading R/V Ranger

1200   Depart dock

October 2nd

1200   On-site at 27 30' North, 76 30' West

1300   Deploy SSAR configured to listen to explosion

1500   Standby to check Argos data for proper buoy operation

1800   Deploy SSAR configured to listen to MAXI-SATS

2100   Deploy MAXI-SATS for sound check

2400   Check Argos data to verify SSAR operation
      Begin steaming to first transmission point

October 3rd

Note: 3 hours is reserved at each point for deploying the source to 350 ft, transmitting 3 sequences 30 minutes apart and taking a 6000' XBT.

0600   60 mile transmission

0900   Begin transit to 2nd point.

1500   120 mile transmission

1800   Begin transmit to 3rd point.

2400   180 mile transmission

October 4th

0300   Begin transit to 4th point

0900   240 mile transmission

1200   Begin return journey to pickup SSARs

October 5th

0000   Repeat 120 mile transmission

0300   Underway again to retrieval point

1500   Find and retrieve SSARs

October 6th

0000   Underway back to Andros Island

1600   At Andros Island

1700   Heavy lift offloads winches, buoys and van from R/V Ranger

October 7th

0700   Finish offloading if necessary.
       Pack container for shipment.

       Container leaves Andros on barge.
       WHOI personnel depart Andros for WPB.

October 8th

Contingency day at sea in case explosions are delayed through the morning of the 7th.

October 9th

Contingency day dockside for unloading R/V Ranger in case of delay noted above.

APPENDIX C

<u>SSAR Atlantic Test Cruise Report</u>
<u>Leg 1: September 28 to October 4</u>

Woods Hole Oceanographic Institution

Thursday Sept. 29

Alex Bocconcelli, Neil McPhee, Skip Gleason and Lee Freitag travel to
West Palm Beach. John Kemp arrives to assist in loading R/V Ranger.

Friday Sept. 30

1000   R/V Ranger clears customs at Port of West Palm Beach.

1200   WHOI equipment van, Pengo winch and Hiab crane are on board.
        Unpacking, setup and tie-down begin.

1230   Computers and shot buoy are setup in the test shack and running.

PM   Shot buoy array assembled with 2 each hydrophones with 1, 5 and
        10 Hz high-pass cutoff. Top 3 elements are mounted in plastic
        housings and attached with urethane isolation blocks. Bottom 3
        are also in housings but attached with Sorbothane wrapped around
        the array cable as isolation. Mecca-type connectors are reinforced
        with self-vulcanizing tape. Tap test performed, all elements OK.

        Welding on Hiab is half done.

        Departure time set for 1500 to 1800 hours October 1 (original
        transit time estimate was 24 hours, 18 hours is transit time
        estimated by the captain at 14 knots).

Saturday Oct. 1

0700   Shot buoy system bench tests OK.

0830   Vessel moved to allow rigging on A-frame.

        Maristar-M Maritime Mobile Earth Station (Scientific Atlanta
        model 9821) is not working and will not be fixed before the
        vessel leaves the dock.

1000   Welder arrives to finish crane and winch.

GPS antenna radome on shot buoy taken apart for visual inspection
(had not performed as well as an identical unit at the same
location). Found missing o-ring. While no damage is visible, the
unit is swapped and the o-ring replaced.

Occasional heavy rain showers

1230   Top and bottom shot buoys loaded. Battery voltage in bottom unit
is 15.12 for main, 21.24 for analog.

1500   Welder done.

1600   John Kemp notices that chassis on a power supply is hot. Measure
120 V AC from one leg to ground, and 240 from the other to ground.
This is probably why the computer UPS reports site wiring problem.
The ship's engineer turns off some other equipment on the same bus
and the problem goes away.

1730   Power problem returns when the same breaker is turned back on. This
will have to stay on since part of the galley is on this circuit.
Installed an isolation transformer in front of the UPS which allows
it to work.

1800   Depart Port of West Palm Beach.

1930   Message from Dan Frye via AUTEC HF radio about 48 hour COMBO delay.

1945   Call Dan via cell phone from bridge to discuss situation. Decision
is to continue.

Sunday October 2

0700   Lost one engine and generator during switchover. Speed was
about 14 knots, now will be 7-8 knots.

Estimated arrival time on site is about 1400 hours. Original plan
called for arrival at 1200 hours.

0800   Final system checkouts. Shot buoy topside disk has 192 Mbytes.
Top SSAR buoy topside battery is 14.67 volts, disk space 206 Mbytes.

Bottom electronics for shot requires about 52 Mbytes per day, about
500 Mbytes are available (about 10 days).

Noticed problem last night with SSAR bottomside electronics. Total
disk space reported was incorrect and at least once the drive was
not available when accessed. Suspect vibration from engine (pressure
case is on deck directly over the engine). Move case forward next
to SATS van and pad with foam. Much less vibration is present.
Problem does not occur again and no problems are reported by disk
check program.

1111   Position reported by buoy GPS receiver is 28 20.477 N, 283 4.67 E,
course 58 deg, speed 8 knots.

1144   Final checkout with acoustic array connected to bottom pressure
case. All elements are working but have different standard deviations.
Channel 2 (the third element from the top) is the one selected to
send a small time series (5000 pts, 16.7 sec) to the surface after
each hourly run.

1400   On station at 28 deg 30 N, 76 deg 30 W. Preparations for deployment
begin. Buoy and bottom pressure cases purged.

Seas are 4-6 feet, winds about 15 knots.

1446   Bottom system running fine, 490 Mbytes free on disk. Shuts down
normally.

1510   Buoy over the side and released with hose.

1515   Subsea float over the side and the wire is fair leaded from stern
winch let go. Cable payout begins.

1600   Bottom pressure case in place on stern and ready for deployment.
Buoy has updated Argos ID at 1943 GMT. Telonics time reset to GMT.

1630   E/M cable has been connected. Top woke up bottom system on schedule.
1645   Bottom finished processing.

1705   Array let out by hand and weight dropped.

1730   Back at buoy to pull it to check time-series data from the bottom.
Buoy secure on deck with system hanging below. Subsurface float
comes nearly to the surface when the ship runs forward at 1-2 knots.
Changed one timeout period in surface control file to make sure
it stays on long enough under all circumstances to receive bottom
data.

1745 Data run complete. Time series from array phone 3 uploaded from buoy. Spectrum shows ship noise signals at 12 and 24 Hz. Peaks are about +/- 2200 counts. Energy is time varying.

Stats summary (see appendix for conversion details):

Phone:	1	2	3	4	5	6	
Cutoff:	1	5	10	1	5	10	(Hz)
MAX:	232	142	18	255	54	95	(counts/128)
STD:	31	32	7	127	24	48	(counts/64)

Looking at channels 1 to 3, channel 1 (1 Hz) has a higher std than 2, which in turn is higher than 3. This makes sense since the lower channels would have more acoustic and heave noise. Trends in channels 4-6 are less clear.

With no time series data from the other hydrophones at the bottom unit it is difficult to tell from the max and std values if the unit is operating correctly. However, with the ship directly overhead the noise performance is uncertain.

1830 Ran system a second time and uploaded data. Very similar to previous set.

1930 Observed one more system run but did not stop topside system to upload time-series but let it shut down normally.

1955 Ready to let buoy go.

2000 Buoy released. Pulls back through water fairly fast.

Location: 28 deg 31.16 N
               76 deg 27.99 W

Start course due north to get away from buoy.
Hold ship quiet from 2030 to 2050

2115 Back near buoy to get Argos data summary.

Phone:	1	2	3	4	5	6	
Cutoff:	1	5	10	1	5	10	(Hz)
MAX:	173	103	20	151	78	38	(counts/128)
STD:	4	0	1	255	0	0	(counts/64)

Standard deviations of 0 indicate fairly low noise.
With the exception of phone 4 the system seems to be OK.

However, really need time series data from all channels
to check this.

Make tentative plans to retrieve buoy in the morning to do
careful check of all data on subsea hard disk in preparation
for receiving shots on the 5th and 6th.

2130   Begin steaming away from buoy.

2225   Range is about 3.5 miles. Request bridge to come to all stop from
30 to 45 minute after the hour to reduce possible ship noise
in data. Vessel rolls badly after 5-10 minutes at all-stop.

Monday October 3rd

0600   Closing in on buoy. Winds 25 knots, gusts to 30 knots. Seas
about 8 feet.

0615   Getting Argos data from ID 4658. Received data from 00, 02, 04
06, 08 and 09 hours GMT. Some data is as good or better than
set from last night, two data sets are noisier. Data from odd
hours is on the second ID which is not received by the Telonics.

0630   Lost 2nd generator. Captain requests that we terminate further
operations and return to AUTEC base. The third generator is
smaller than the first two and if we lose it we will have no
steering or other systems.

0730   We briefly consider pulling the array, but the weather is too rough
and it is also possible that we would miss the shot on the 5th
if we cannot get back out in time.

Maneuverability is also limited with only one screw and the bow
thruster is inadequate in these seas. Chief engineer is concerned
about having enough power to operate the crane and A frame for
any deck operations.

0800   Deck secure and begin transit to AUTEC base. 30 hours is estimated
for trip.

Position of buoy at 0730 is: 28 27.718 N
                                76 29.046 W

In 10 hours it has gone 3.6 miles. (8.6 miles per day).

Tuesday October 4

1030 Receive word that shots are delayed at least one additional
      day. Earliest shot will be on the 6th. More information
      expected this afternoon.

1200 At AUTEC base.

SSAR Atlantic Test Cruise Report
Leg 2: October 4 to October 9

Woods Hole Oceanographic Institution

October 4

AUTEC personnel board as soon as the R/V Ranger arrives. Within a few hours the
problems with the engine and generators are diagnosed. Departure is set for 1200 October 5.

Tom Zeh arrives at AUTEC to review requirements for the rest of the experiments. States
that Ernie Moody agrees that ship time for transit to and from work site due to engine
problems will not be charged to the project. Schedule set for deployment of SSAR off
Eluethera with MAXISATS to be done on the way north to pick up the shot buoy.

End-end checkout of m-sequence generator and tomography processing performed.

October 5

1200   Depart AUTEC for 25 deg 30 N, 75 deg 30 W.

October 6

0015   On station. Preparing for deployment.

0045   Buoy over the side.

0145   E/M cable out, bottom connected to top via cable for test.

0158   Systems running and ready.

0215   Array and weight over the side.

0300   Time and position log set up in MAXISATS van

0330   Start setting up MAXISATS for test transmission.

0405   MAXISATS transducer over the side and ready

0430   Reset and power on full at 08:30:02.060 GMT.
25 27.7103 N 284 34.3159 E.

Breaker tripped in SATS main power supply, back on after less
than 1 minute.

0450   Tomography data received via local receiver is good: 2 peaks
1 at greater than 50 dB SNR, 1 at 27 dB. GPS data is also
good. Sensor data looks incomplete but it is not possible to
check without pulling buoy. Decide to continue since tomo is
main objective and it appears to be working fine.

0500   MAXISATS retrieved. Monitor hydrophone support breaks off during
retrieval (the 3000 lb transducer is swinging fairly badly
during recovery).

0530   Depart site. RDF unit gets range of 2-3 miles but bearings are
ambiguous sometimes.

Buoy gps data is: 25.463 N, 284.560 E at 0430 local.

1050   On station at first long-range transmission site. Preparing
to lower MAXISATS. Range calculated from ship's GPS is 60.1
miles.

1110   MAXISATS transducer deployed to 350 ft.

1130   Transmission 1 at 160 dB (est).
Sync: 15:28:49.692 GMT at 26 20.0332 N, 283 59.6185 E
Heading 260 deg at 1531 GMT.

1200   Transmission 2 at 165 dB (est).
Sync: 15:58:49.005 GMT at 26 19.9059 N, 283 59.5268 E
Heading 253 deg.

1230   Transmission 3 at 170 dB (est).
Sync: 16:28:49.053 GMT at 26 19.68180 N, 283 59.4258 E
Heading 56 deg.

1300   Transmission 4 at 170 dB.
Sync: 16:58:49.802 GMT at 26 19.5027 N, 283 59.3320 E
Heading 241 deg.

1315   Pulling up transducer.

1330   Begin steaming to next site.

1420   Received positions from WHOI via AUTEC SSB for both buoys.
        SUS charges will be on 10/7 at 0935 and 1035.

1830   On site for 2nd long-range transmission.
        XBT taken.

1900   Transmission 1 at 160 dB.
        Sync: 22:57:42.160 GMT at 27 17.6545 N, 283 47.3282 E
        [Heading held at 200 to 210 deg during all transmissions].

1930   Transmission 2 at 165 dB.
        Sync: 23:27:41.029 GMT at 27 17.3358 N, 283 46.7557 E

2000   Transmission 3 at 170 dB.
        Sync: 23:57:40.594 GMT at 27 16.9913 N, 283 46.1583 E

2030   Transmission 4 at 170 dB.
        Sync: 00:27:43.882 GMT at 27 16.7707 N, 283 45.5346 E

2100   Transmission 5 at 170 dB.
        Sync: 00:57:41.868 GMT at 27 16.5621 N, 283 44.9367 E

2130   MAXISATS on board and secure

October 7

0230   About 5 miles from estimated position of shot buoy.
        Begin slowly approaching area.

0400   RDF gear is receiving transmissions. Ship is at
        28 8.9 N, 76 58.0 W.

0600   Visibility is very poor, heavy rain, wind to 30 knots.

0800   Preparing to leave search area in anticipation of SUS
        drops (want to avoid ship noise in data).

0823   Abandon search and begin transit, presumably away from
        buoy. However, local receiver starts getting more data.

0831   Buoy in sight at 28 11.68 N, 77 00.331 W. Pass within
        300 m and pause with engines off from 0834 to 0850.

0850   Transit north, pause with engines at all stop from
        0930-0945 and 1030-1045.

        Estimated distance from SSAR buoy is 191 miles.

1100   MAXISATS deployed. Seas rough, 4-7 ft. Drift at 1-2 knots.

1130   Transmission 1 at 170 dB.
        Sync: 15:26:4.02 GMT at 28 18.8338 N, 282 57.5471 E.

1200   Transmission 2 at 170 dB.
        Sync: 15:56:0.023 GMT at 28 18.7478 N, 282 56.3704 E.

1230   Transmission 3 at 170 dB.
        Sync: 16:25:57.625 GMT at 28 18.7019 N, 282 55.0696 E.
        Kept source on through 1245 local so that shot buoy can
        also record the data.

1315   Transducer on deck.

1405   Back at previous buoy sighting point.

1425   Buoy in sight about 1.5 miles from last fix.

1445   Buoy on deck.

1600   Cable up

1615   Array on deck.

1700   Deck secure, hose coiled. Start transit south back to SSAR.

October 8

1030   About 3 miles from latest Argos positions.

1035   Receiving signal on RDF

1045   First sighting (visibility excellent)

1050   Position at pickup is 25 deg 12.528 N, 75 deg 10.236 W

1115   Buoy on board

1130   Hose up and on deck

1150   E/M cable coming in

1230   Bottom case and array on deck

1400   Deck secure, start transit back to base.

October 9

0730   In port at AUTEC, Andros Is.

Appendix C1 - Hydrophones and Analog Front-end Sensitivity

Net response of High-Tech hydrophones is -184.5 with a 506 ohm termination resistor and -187.8 with a 383 ohm resistor (as installed in the current system).

Power consumption is 5.5 mA each over the rated voltage range.

Analog front-end gain (fixed portion) is 24 dB. No programmable gain is added. Additional gain in the A/D converter board is 3 dB.

Total response is thus -187.8 + 24 + 3 = -160.8 dB.

Appendix C2 - Estimated output voltage levels from COMBO shots.

Galen Pound of ENSCO estimated that at a distance of 60 degrees the first shot would have a received sound pressure level of 44 dB re uBar (144 dB re uPa). (ref memo Sept. 9, 1994 from ENSCO.)

Voltage out of the A/D will then be 144 - 160.8 = -16.8 dB re volt.

A/D max is 5 V peak-peak or about 14 dB re volt. Headroom is thus about 31 dB for the first (largest) shot.

Appendix C3 - Data Format for Shot Buoy Argos Buffers

ID 4654 will send only a 4 byte buffer if no data is received from the bottom system. In this case the buffer will be:

DAY HOUR MIN SEC

This date and time is when the Argos uploading process is being performed.

ID 4654 will contain 32 bytes if data is received from the bottom system.
The buffer format will be:

DAY	HOUR	MIN	SEC	M1	M2	M3	M4
M5	M6	S1	S2	S3	S4	S5	S6
L1	L1	L2	L2	L3	L3	L4	L4
L5	L5	L6	L6	xx	xx	xx	xx

where the date and time are when the data collection was completed, Mx are the buffer maxima/128, Sx are the buffer standard deviations divided by 64, and the two byte Lx values are indices into the buffers where the maxima occurred. Maxima and standard deviations are in A/D counts.

Standard deviation values are calculated on a small buffer of 100 pts about 30 seconds into the data collection period. They are intended as only a very rough guide to total energy. 150 Hz of bandwidth is assumed in these calculations.

S value	StdDev counts	dBV	dB re uPa
0	0-63	< 46	< 93
1	64	-46	93
2	128	-40	99
4	256	-34	115
8	512	-28	121

Argos IDs 4658 and 4659 have the same data format as noted above. However, these IDs contain information from the most recent 16 data collection periods. Each hour the oldest buffer is removed and the current one added.

APPENDIX D

Summary of deployment: Depart San Diego late on the 11th. Arrive off Pt. Sur on the 13th. Deploy one SSAR buoy near NAVFACS receiver and let run for 6 hours (3 source transmissions). Recover and steam south to 35 deg N, 123 deg W. Deploy all buoys in this area and check for proper operation. Return to San Diego on the 17th. Note: we must be back on the 17th because another party is scheduled to load on the 18th and depart on the 19th.

Science Party: John Bouthillette, Neil McPhee, Skip Gleason, Larry Costello and Lee Freitag (all WHOI). Penn State: Carter Ackerman, Bruce Einfalt and George Parides.

Cruise Schedule

Note: We will be leaving the dock after the Flip leaves port, which is scheduled for November 10th. We will not depart until they leave port.

November 8

Deployment party travels to San Diego.

November 9-10

Mobilization on-shore at Scripps.

November 11

0800   Begin loading the Sproul if USNS Sioux has departed at 0600
        on the 10th with Flip as scheduled.

        Depart when ready, probably between 2100 and 2300 hours.

        First deployment is at Pt. Sur: 36 deg 18' N, 122 deg 24' W

        Estimated distance 400 miles, 43 hours transit time.

November 12

        Transit

November 13

1800   On-site and preparing for deployment

2000   Buoy deployed. Check data via Argos.

2200   Steam away about 10 km to cut down on ship noise at buoy.

November 14

0000   First source transmission from Flip

0030   Steam back to buoy location.

0130   Data from first buoy received via Argos and checked.
         Begin steaming away at least 10 km and hold station.

0200   2nd source transmission from Flip
0400   3rd
0600   4th

0630   Steam back to buoy to begin recovery at first light.

0730   Recovery started

0930   Recovery complete

1000   Begin steaming for 35 deg N, 123 deg W. (About 80 miles south,
         9 hours transit).

1900   On-site

2000   Deploy 1st buoy.

November 15

0000   Transmission from FLIP

0100   Move close to buoy to get Argos data

0400   Transmission from FLIP

0500   Move close to buoy to get Argos data

0600   Deploy 2nd buoy at first light
         Check data after deployed.

1200   Deploy 3rd buoy
         Check data after deployed.

1800   Return to port. (estimated distance is 300 miles, 33 hours)

November 16

transit

November 17

0600 In port

1700 Deck gear removed from vessel

November 18

Personnel return to WHOI and PSU

Leg 2 - R/V Sproul, November 29-December 3

SSAR Retrieval Cruise
Personnel: Alex Bocconcelli, Skip Gleason, Steve Merriam, John Bouthillette
and Neil McPhee (all WHOI).

November 28

Personnel travel to San Diego

November 29

0800 Load vessel with retrieval gear, radio direction finding system and
3rd buoy if it was not deployed earlier.

1600 Depart for extrapolated buoy positions based on Argos satellite info.

November 30

Transit

December 1

0600 Arrive near expected position of first buoy

0900 Retrieve first buoy

1200 Arrive near expected position of 2nd and 3rd buoys

1500 Retrieve 2nd and 3rd buoys

Begin transit back to San Diego (allow 48 hours for transit plus
possible buoy deployment and data check).

December 2

    Transit

December 3

1800 In port

December 4

0800 Off-load vessel

December 5

    Contingency for weather or other delays.

DRIFTING BUOY SYSTEMS USING RUBBER STRETCH HOSE

The following manuscript was submitted to the SEA TECHNOLOGY magazine to be published in the December 1994 issue.

DRIFTING BUOY SYSTEMS USING RUBBER STRETCH HOSE

Walter Paul and Alessandro Bocconcelli

Woods Hole Oceanographic Institution

Applied Ocean Physics and Engineering Department

Woods Hole, Massachusetts

ABSTRACT

Most drifting buoy systems require the capability to transmit position and sensor information to satellites. In order to send data from sensors suspended below a drifting surface buoy a reliable electrical conductor path is mandatory. However the long term survivability of conductors in the upper portion of a suspended surface buoy tether is a challenging problem due to the continuous action of surface waves. This article describes information about the development and testing of compliant nylon reinforced rubber hoses that serve as conduits for electrical conductors and as shock absorbers in drifting buoy systems.

INTRODUCTION

A free drifting acoustic receiver is being developed as part of the Global Acoustic Mapping of Ocean Temperatures (GAMOT) project [1]. It consists of a surface buoy from which an instrument package and vertical hydrophone array are suspended at about 500 meter depth. Called the Surface Suspended Acoustic Receiver (SSAR), it is designed to be a low cost alternative to fixed receiver arrays used to detect changes in sound travel time between acoustic sources and the array hydrophones. Two prototype SSARs called *Standard* and *Snubber* (Fig. 1) have been developed.

THE NEED OF TETHER COMPLIANCE IN DRIFTING BUOY SYSTEMS

A drifting buoy with a suspended cable and sensor package is a spring mass system responding to the heave motions of the buoy in a sea state with distinct natural frequencies, motions, and tether tensions.
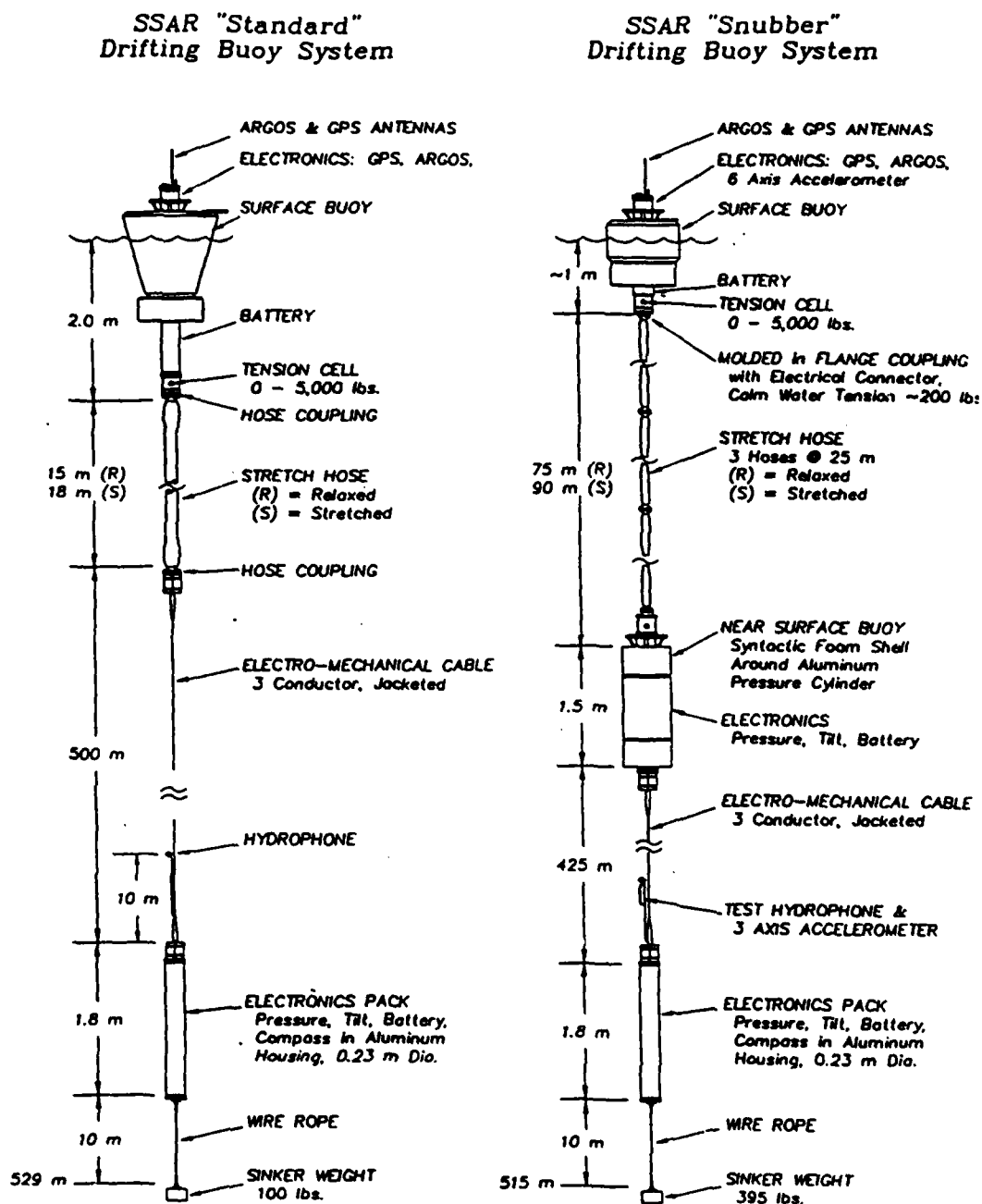
Fig. 1: *Standard* and *Snubber* prototype SSAR designs as used during the 1993 at-sea tests.

Wave motions at the buoy introduce dynamic loading. Tensions in the tether cable increase when the surface buoy is lifted by a wave due to the need to overcome hydrodynamic drag and inertial resistance of the suspended cable and sensor package. When the buoy descends from a wave crest, inertia and dynamic drag loads act opposite to the static weight load and reduce and possibly eliminate the tether tension. If in this case the dynamic and inertia forces become larger than the static weight load, the cable tether becomes slack, since it cannot support compressive forces like a connecting rod. When the buoy is being raised by the next wave, the unavoidable sudden tensioning of the slack cable can cause impact or snap loading [2]. Snap loads are significantly reduced or eliminated by the inclusion of a compliant shock absorber between the surface buoy and the suspended cable. A sea test of the *Standard* SSAR recorded maximum tensions of about twice the static weight force and 100 lbs minimum tension without occurrence of snap load.

DEVELOPMENT OF THE STRETCH HOSE AS AN ELASTIC TETHER

Reinforced rubber stretch hoses were developed for two SSAR drifting buoy systems to serve as a compliant shock absorber and as a conductor path between surface buoy and the suspended electro-mechanical cable and sensor package. In the *Snubber* SSAR the hose is arranged between the surface float and a subsurface buoy. In the *Standard* SSAR the hose connects the surface buoy to the suspended cable and sensor package directly (see Fig. 1). Both designs incorporate electrical conductors arranged inside the stretch hose cavity with sufficient length to allow for the hose stretch without straining the copper conductors. The hoses may also contain an initially slack stop rope, which engages when the hose exceeds a certain elongation. The rope with higher modulus and strength than the hose will dominantly

share severe tensions and limit hose load and stretch to safe fractions of its strength.

Hose Construction:

The SSAR hose wall is made of suitable rubber compounds which are encapsulating layers of reinforcing materials. The main reinforcement consists of parallel nylon tire cords, which form an evenly and tightly spaced fabric structure. The tire cord fabric is covered with rubber, resulting in a thin cord containing rubber sheet as the building element for the hose. Its strength in the direction of the cord axis is over 250 times that of a cross section made entirely of rubber. Custom compounded rubber materials form the inner tube, intermediate layers, and the outer jacket of the hose.

The hose components are hand laid up around a steel mandrel. Over the inner rubber tube the reinforcement layers, sliced to specified widths, are counter-helically applied similar to the ribbon wrapping around a maypole. Identified wrap angles deliver the required compliance of the hose [3]. Additional reinforcing layers are gradually built up at each hose end to create low stretch sections with increased axial and bending stiffness. A spiralled arrangement of Kevlar tire cord fabric is built into the outer hose wall to increase the hose resistance to fishbite, a serious problem in many parts of the world oceans. An outer rubber jacket completes the hose.

The hose terminates into a flanged coupling, which is molded into the hose body during its fabrication process. Through steam treatment (vulcanization) the couplings form an intrinsic part of the hose. The vulcanization process creates the extraordinary toughness and cohesion of reinforced rubber structures. The hose end section with its coupling is shown in Figure 2.

In service the hose is filled with a suitable fluid (water in this case) to prevent hose

collapse under hydrostatic pressure. The counterhelically arranged load carrying tire cord layers increase the fill fluid pressure when the hose is under tension.

① STANDARD OFFSHORE FUEL HOSE COUPLING

② HOSE BODY WITH EXTRA REINFORCEMENT BUILDUP AT COUPLING

③ BEND LIMITING SECTION OF HOSE

④ STRETCH SECTION OF HOSE

⑤ COUNTERHELICAL NYLON REINFORCEMENT TO CONTROL HOSE STRETCH

⑥ FISHBITE PROTECTIVE COUNTERHELICAL LAYER OF KEVLAR FABRIC
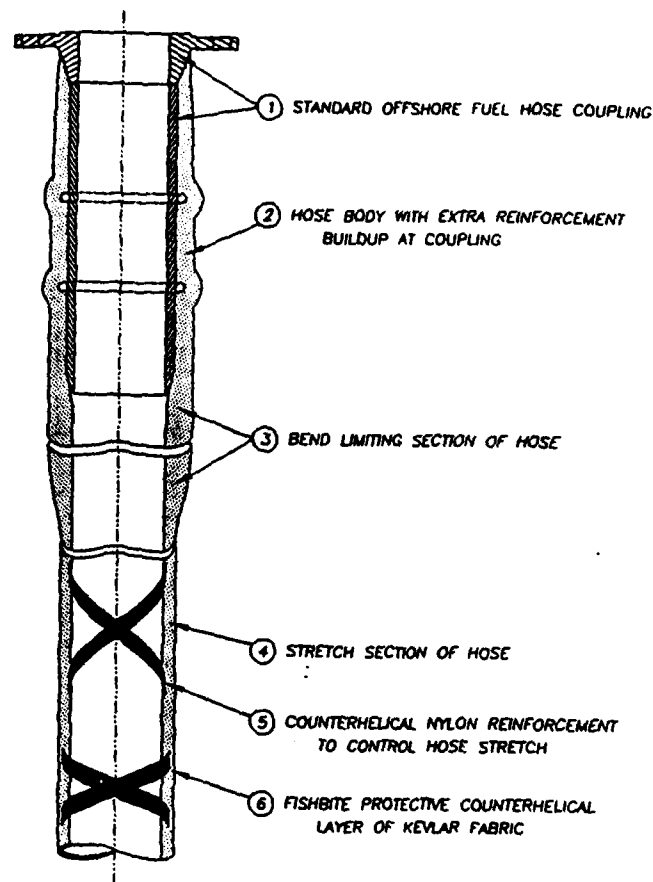
Figure 2

Fig. 2: Cross section of stretch hose and termination

Hose Load Elongation Properties:

The hose load elongation properties are dominated by the reinforcing nylon tire cord fabric, with additional stiffness provided by the rubber material. The stretch resistance of a given hose size is strongly influenced by the wrap angle at which the nylon tire cord is applied. The higher the wrap angle, the stretchier the hose and the lower its load carrying capability. The load level for a given wrap angle can also be modified by altering the hose diameter, cord size, and cord density. The hoses are considerably larger than ropes of the same strength and have the appearance of elephant trunks. For a 1,600 lbs safe working load a well padded hose with maximized stretch has an outer diameter of 5.2 inches and a wall thickness of 0.6 inch. The diameter of an equally strong nylon rope with much lower stretch is only 0.75 inch. The maximum new hose stretch is kept at about 30 percent, at which the tension of the nylon tire cords is designed to be about 10 percent of their breaking strength. Some of the new hose stretch is lost in use through permanent elongation and modulus increase found in most materials. The bulkiness of the shock absorbing hoses seems to be advantageous in the turbulent surface wave field.

Laboratory Fatigue Testing of Hose:

A special test machine was built by a commercial laboratory to simulate combined axial elongation and flexing cycles experienced by the surface buoy end of the hose in its duty at sea. One end of the tester stretches and relaxes the hose, while the other hose end is bent back and forth at a faster frequency. Flex angle, amount of stretch, and flex and stretch test frequencies can be adjusted. Fill fluid pressure and stretch under applied axial tension was monitored, as was the change of stretch near the hose terminations due to the addition of extra reinforcing.

Three hoses have been tested; the first two with exaggerated hose tensions and flex angles of +/-45 and +/-25 degrees. Hoses were stretched up to 50 percent at each tension peak, loading the reinforcement up to 30 percent of its breaking strength, and developing fill fluid pressure up to 220 psi during each cycle. The two hoses failed by bursting the hose wall at the flexing end of the samples with no appearant damage of the reinforcement after less than 10,000 and 40,000 flex cycles respectively. An improved test sample was built with increased wall thickness and additional end reinforcement, which was tapered more gradually. This third sample also incorporated electrical conductors into its hose wall. This hose survived 1 million flex cycles to +/- 30 degrees at tensions simulating survival tensions and twice survival loads.

BEHAVIOR IN SEA TRIALS

The *Standard* SSAR was deployed for an endurance test 50 miles southwest of Bermuda in September 1993. After an unscheduled recovery and redeployment - the *Standard* SSAR had almost drifted onto one of the Bermuda reefs - the endurance test was terminated after four winter months at sea in the Atlantic near Bermuda when electrical communication between suspended sensors and surface buoy was lost. After retrieval it was found that the conductor rope assembly inside the hose had formed sharp loops which abraded at contact points with the inner hose surface. Otherwise the buoy system was functioning properly.

The hose was attacked by a shark. Long thin razorblade-like cuts were found on one hose side, the other side showed impress-ions of the lower jaw's teeth. The cuts did not penetrate beyond the fishbite protective layer of Kevlar tire cord fabric located about 0.1 inch

beneath the hose surface, which captured a small toothtip as evidence. The load carrying nylon fabric layers and the inner hose wall were not damaged.

CONDUCTOR ISSUES

The upper conductor portion inside the fluid filled hose is subject to relentless lifting and lowering tensions as the hose responds with stretch and relaxation to the sea state motions of the surface buoy. The conductors are subject to dynamic tensions maximized at the top. The conductors have to permit up to 30 percent cyclical hose stretch and relaxation. This was made possible by arranging in a somewhat coiled fashion 30 percent longer strength member supported conductor assemblies into the hose cavity, a practice used in horizontally towed stretch hose.

In the prototype *Standard* SSAR a stop rope was arranged in combination with a longer conductor rope. The prime reason for a stop rope was to have an elongation limiter for the stretch hose to prevent the loading of the hose reinforcement above safe limits. During the 4 month sea test, the 30 percent extra conductor length migrated toward the bottom end of the hose. This caused formation of the sharp loops which destroyed the copper wires through abrasion against the inner hose wall after an estimated 4 million stretch cycles. Our conclusion is that randomly arranging extra conductor length into a vertically operating stretch hose was not reliable.

The most recognized stretch cable is the coiled telephone cord, which can typically increase its length five fold and can therefore easily accommodate the 20 to 30 percent cyclical length change of the stretch hose in a severe sea state. If such a cord is able to retract to its coiled configuration even after a large number of extension cycles, it should

form a reliable conductor path. Custom configured coil cords as shown in Figure 3 were

therefore developed for the SSAR application [4].
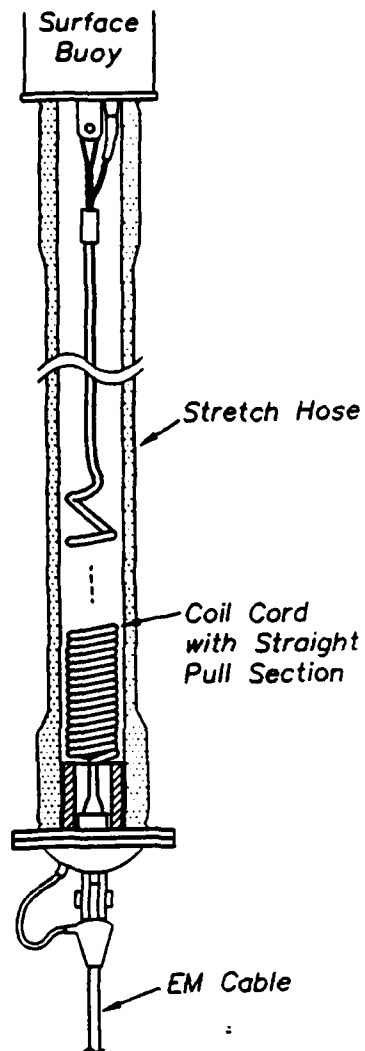
Fig. 3: Coil cord assembly prevents snarling inside stretch hose

A 10 meter high vertical coil cord fatigue test facility was constructed from

transparent PVC tubing by the Woods Hole Oceanographic Institution. A coil cord assembly

is being lifted inside the water filled tubing 3 ft every 3 seconds, and has

passed the two million cycle count at the time of this writing. So far no noticeable abrasion

or snarling has been observed.

REVISED CONDUCTOR DESIGN FOR STRETCH HOSE ASSEMBLIES

For a currently ongoing assembly of a small series of *Snubber* and *Standard* drifting buoy systems custom sized coilcord assemblies have been developed and the stretch hoses have been ruggedized. Due to the low peak loads monitored in the *Standard* sea test and the inherent strength of the hoses it was decided to eliminate the stop rope inside the hose. This way the heavy coil cords do not have to share the hose cavity with the stop rope, reducing the risk of abrasion and entanglement. With the good performance of the coilcords in fatigue testing, and the endurance of the hose in the four month sea trial, it is hoped to keep the SSAR buoy configurations electrically and mechanically intact over a planned one year service life.

ACKNOWLEDGMENTS

REFERENCES

[1]   Spiesberger, J.L., Frye, D.E., O'Brien, J.O.., Hulbert, H., McChaffrey, J.W.,

Johnson, M., Kenny, J. (1993): *Global Acoustic Mapping of Ocean Temperatures

(GAMOT);* IEEE Oceans'93 Proceedings, pp. I-253-I-257.

[2]   Berteaux, H.O. (1989). *Equipment Lowering Mechanics*; In: Handbook of

Oceanographic Winch, Wire and Cable Technology

A. Driscoll, Ed.), Chapter 9, pp. 9-7, 9-19

[3]   Paul, W., Bocconcelli, A., Grosenbaugh, M.(1994): *Drifting Buoy Systems Using

Elastic Rubber Stretch Hose*, BOSS'94 Behavior of Offshore Structures, Pergamon

Press, Vol.2, Cambridge, MA, pp. 213-225.

[4]   Paul, W., Bocconcelli, A., Boutin, P.B., (1994): *The SSAR Drifting Buoy System, a

New Approach for a Reliable Telemetry Link to a Suspended Sensor Package*, MTS'94

Conference Proceedings, Marine Technology Society, Washington, DC, pp. 398-408.

Alessandro Bocconcelli is a Research Associate in the Ocean Systems and Moorings Laboratory at Woods Hole Oceanographic Instutiton. He specializes in the design of buoys, mooring systems, and underwater structures. He graduated from the Italian Merchant Marine Institute with a Captain degree (unlimited tonnage) and holds a Bachelor's and Master's degree in Ocean Engineering, both from MIT. Alessandro has been working for WHOI for nine years.

Walter Paul received his PhD degree from the University of Hannover, Germany, with thesis work in the area of fiber rope mechanics. After employment in the rope industry he worked for 19 years at Gould Inc., later Martin Marietta in Maryland in the design of fibreous strength members, EM and EOM tow cables, and reinforced hose structures in support of high speed towed arrays. At the Woods Hole Oceanographic Institution's Ocean Systems and Moorings Laboratory his work includes new approaches to design, build, and test compliant shock absorbing strength members in form of reinforced rubber hoses with electrical conductors.

QUARTERLY PROGRESS REPORT NO. 6

Contract: SC25048

Sponsor: Woods Hole Oceanographic Institution

Project Leader: Mark Leach

Report Period: July, August, and September 1994

Applied Research Laboratories, The University of Texas at Austin (ARL:UT), is tasked to provide Woods Hole Oceanographic Institution (WHOI) with a method and system for determining accurate positions of free floating Surface Suspended Acoustic Receivers (SSAR). ARL:UT is to provide guidance in the selection of Global Positioning System (GPS) equipment, and determine the best method of obtaining SSAR positions. Subtasks 1, 2, 4, 5, 6, 8, have been completed and documented in previous Quarterly Progress Reports. During this report period the following efforts were completed.

<u>Subtask 3:</u> Develop Receiver Control Software

During this report period, ARL:UT provided enhancements and modifications to the receiver control software (RCS) to improve reliability and to correct an anomaly discovered during buoy system integration and testing. While conducting reliability testing, ARL:UT identified a potential failure path that could have resulted in a loss of both position fixes if the second of two positions was not obtained. The output file writing logic was modified to write position information for each fix independently. The information for both fixes is then combined into a single file when both positions are successfully obtained. Also, a potential memory allocation conflict problem was identified, and additional memory handling logic was implemented to preclude any conflicts.

The RCS was modified to reduce the communication baud rate between the buoy computer and the GPS receiver. During system integration testing, WHOI observed system lock-up while collecting GPS position data. The cause of these system lock-ups was the buoy processor's inability to support the baud rate specified by the RCS. ARL:UT had not observed any anomalies during testing of the RCS due to differences in computer microprocessors. The buoy's system processor will not reliably support the 9600 baud rate originally used by the RCS. The baud rate was reduced from 9600 to 1200, and no further occurrences of system lock-up have been reported. Utilization of the 1200 baud rate will not adversely affect GPS system operation. An additional checksum verification was also enabled to improve reliability. ARL:UT will continue to support and maintain the RCS until system integration and testing is complete.

<u>Subtask 7:</u> Position Correction Facility Integration and Testing

During the previous report period, adaptation of the Position Correction Facility (PCF) software from a prototype to deliverable configuration was completed. ARL:UT's principal effort on this subtask during this report period was isolating an error discovered while testing

the GPS pseudorange reconstruction software. The program was computing incorrect psuedoranges for a subset of the observed satellites at irregular intervals. The cause of the error was identified and corrected, and preliminary test results indicate the PCF is performing nominally. ARL:UT will continue to operate and test the PCF through the next quarter.

Subtask 9: Develop PCF and RCS Documentation

Documentation efforts for the RCS and the PCF continued during this quarterly period. The software programs that comprise the PCF process will each be documented in separate sections for user reference. The PCF process has five software components: 1) automated ephemeris data downloading from the Defense Mapping Agency (DMA); 2) decompression and formatting of ephemeris data; 3) reconstruction of GPS observable data from position information; 4) removal of Selective Availability effects; and 5) computation of corrected positions. Draft documentation was completed for items 1 and 5. Documentation for the PCF and RCS, including system design, will be completed during the next quarter.

NUM	TASK C	Start Date	Finish Date
C.1	MECHANICAL DESIGN OF CABLE, BOUY AND TERMINATIONS		
	INITIAL DESIGN	4/15/93	8/9/93
	ACCEL LIFE TESTS	8/31/93	4/17/94
	AT SEA TRIALS	9/13/93	12/18/94
	DESIGN REFINEMENTS	3/1/94	3/1/95
C.2	BOUY ELECTRONICS AND NAV SYSTEMS		
	SYSTEM DESIGN	4/15/93	9/1/93
	CONTROLLER /GPS INTERFACE	4/15/93	12/15/93
	ARGOS TELEMETRY	4/18/93	8/28/94
	POWER SYSTEM	4/15/93	12/15/93
	PROTOTYPE TESTS	8/1/93	12/11/94
C.3	DSP SYS ACOUSTIC NAV AND SENSOR MODULE		
	SYSTEM DESIGN	4/15/93	9/1/93
	SENSOR MODULE	4/15/93	12/15/93
	ACOUS NAV MODULE	4/15/93	5/15/94
	DSP MODULE	4/18/93	5/15/94
	DSP SOFTWARE	5/23/93	12/18/94
	TELEMETRY	4/15/93	12/15/93

Timeline columns: 1993 (A M J J A S O N D), 1994 (J F M A M J J A S O N D), 1995 (J F M A M J J)

NUM	TASK C	Start Date	Finish Date
	PROTOTYPE TESTS	8/1/93	12/18/94
	DESIGN REFINEMENTS	3/1/94	3/1/95
C.4	HYDROPHONE ARRAY		
	ARRAY DESIGN	4/15/93	6/10/93
	PROTOTYPE TESTS	10/1/93	12/18/94
C.5	GPS NAV SA CORRECTIONS		
	DATA COLLECTION METHODS	4/15/93	6/12/94
	DEVELOP SOFTWARE	5/1/93	12/15/93
	PROTOTYPE TESTS	12/15/93	12/11/94
C.6	SYSTEM INTEGRATION		
	LAB TESTS	11/15/93	5/15/94
	AT SEA TESTS	8/14/94 10/16/94	8/28/94 10/23/94
	DESIGN REFINEMENTS	2/25/94	2/5/95
C.7	FABRICATION OF SSAR		
	BUILD 2 PROTOTYPES	5/1/93	8/30/93
	BUILD & TEST 3 SSARS	1/1/94	12/4/94
	BUILD & TEST 3 SSARS	3/1/94	12/4/94
	BUILD & TEST 4 SSARS	5/1/94	12/4/94

NUM	TASK C	Start Date	Finish Date	1993	1994	1995
C.8	FIELD OPERATIONS					
	DEPLOY 4 SSARS	7/16/95	7/16/95			⊠
	DEPLOY 3 SSARS	7/16/95	7/16/95			⊠
	DEPLOY 3 SSARS	7/16/95	7/16/95			⊠

ISSUES AND CONCERNS

There are three issues which have been discussed previously and are briefly updated:

- Acoustic interaction of cabled sources with the bottom slope.
- Identification of a source for the Task D autonomous mooring.
- An at-sea test with a suitable source transmitting M sequences over long range is desirable to fully verify SSAR operation.

There is one new issue:

- The October Atlantic Test was not part of our original Task C requirements. As a consequence, the resources set aside for deployment of the operational SSARs were used to perform this important test (with ARPA's concurrence). Thus, new funds are needed to conduct the deployment cruises.

CABLED SOURCES ON THE BOTTOM

As previously discussed, bottom interaction may be a problem for the SSAR because the transmission paths change for each different SSAR position and the bottom interactions are typically not known well enough to accurately predict its effects. The Kauai and Pt. Sur sources will be bottom mounted

In November 1994, ATOC will conduct the AET test which should provide valuable information about signal to noise ratios, stability of multipaths, and possible bottom interactions. GAMOT will participate in that test.

IDENTIFICATION OF A SOURCE FOR THE AUTONOMOUS MOORING: TASK D

ARPA has decided that an autonomously moored source is not needed at the present time and therefore did not approved the GAMOT proposal to build a 70 Hz source.

AT SEA TEST

Although NMFS had given permission to GAMOT to conduct this test, the at sea test of the SSARs using the HLF-6A source suspended from a ship has been scrubbed due to lack of funds.

SSAR DEPLOYMENT FUNDING

The October Atlantic Test was not part of our original Task C requirements. As a consequence, the resources set aside for deployment of the operational SSARs were used to perform this important test (with ARPA's concurrence). Thus, new funds are needed to conduct the deployment cruises.

DELIVERABLES

There were no deliverables due this quarter.

Four deliverables are due during the next quarter:

     1. Seasonal cycle influences on acoustic travel times based on the analysis of the 1987 tomographic data.

     2. Documentation of ray tracing programs used in ocean models.

     3. SSAR design and test report.

     4. Delivery of SSARs 1 through 3.

Figure:
Fig. 1 GAMOT Deliverable Master Schedule

TASK	DELIVERABLE	Start Date
A.1	SOURCE DEPTH, FREQ, LOCATION AND TYPE RECOMMENDATION	11/30/93
A.2	RANGE OF ACCEPTABLE SSAR DEPTHS	11/30/93
A.3	SIGNAL PROCESSING OF SSAR SIGNAL	6/30/95
A.4	ARRAY MOTION COMPENSATION SOFTWARE	3/30/94
A.5	SEASONAL MULTIPATH ALGORITHMS	6/30/95
A.6	ARGOS RECEPTION ERROR STUDY	6/30/95
A.7	ALTERNATIVE SATELLITE SYSTEM EVALUATION	6/30/95
A.8	REAL TIME TOMOGRAPHY ALGORITHMS	6/30/95
A.9	NEW WORK: SEASONAL CYCLE INFLUENCES ON ACOUSTIC TRAVEL TIMES BASED ON ANALYSIS OF 1987 TOMO DATA	10/30/94
A.10	NEW WORK: OCEAN MODEL OF TEMPERATURE MAPPING USING SSARS	5/30/95
B.1	1980-1991 EQUATORIAL WIND FIELD MODEL STATEMENT OF COMPLETION	6/30/93
B.2	EXTRACT THE COASTAL KELVIN SIGNAL FROM THE EQUATORIAL MODEL AND DRIVE THE MID-LATITUDE MODEL FROM 1980-1990 AND PROVIDE A VIDEO OF THE SOLUTION	9/30/93

Figure 1: GAMOT Deliverable Master Schedule

Figure 1: GAMOT Deliverable Master Schedule

TASK	DELIVERABLE	Start Date	Milestone
B.3	INTEGRATE THE MODEL SOLUTIONS BETWEEN HAWAII AND WEST COAST RECEIVERS AND PROVIDE A GRAPH OF TRAVEL TIME DIFFERENCE AS A FUNCTION OF TIME AND GREAT CIRCLE PATH	9/30/93	◆ (Sep 1993)
B.4	DRAFT PAPER (AND PROGRESS REPORT) DEMONSTRATING CONNECTION BETWEEN OBSERVED ACOUSTIC DATA AND OCEAN CLIMATE MODEL	12/30/93	◆ (Dec 1993)
B.5	PROVIDE DETAILED PLAN FOR IMPLEMENTING INVESTIGATION FOR MORE COMPLICATED MODELS. PROVIDE PROTOTYPE DESIGN OF EXPERIMENT FOR MONITORING THE NORTH PACIFIC FOR CLIMATE CHANGE AND NATURAL VARIABILITY	6/30/94	◆ (Jun 1994)
B.6	DOCUMENT RAY TRACING PROGRAMS USED IN OCEAN PHYSICAL MODELING	12/30/94	◇ (Dec 1994)
B.7	REPORT ON THE ANALYSIS OF THE RUN OF 1970-1991 NRL MODELS	5/30/95	◇ (May 1995)
B.8	IMPLEMENT DATA ASSIMILATION PLAN USING ADJOINT MODEL	5/30/95	◇ (May 1995)

Figure 1: GAMOT Deliverable Master Schedule

TASK	DELIVERABLE	Start Date	Schedule (1993–1995)
B.9	FINAL REPORT EXPLAINING OR NOT EXPLAINING OBSERVED CLIMATE VARIABILITY IN THE NORTH PACIFIC OCEAN	6/30/95	◇ 1995 (J)
C.1	SSAR PROGRESS REPORT	11/30/93	◆ 1993 (N)
C.2	SSAR DESIGN AND TEST REPORT	12/18/94	◇ 1994 (D)
C.3	SSAR UPDATED DESIGN REPORT	3/30/95	◇ 1995 (M)
	SSAR DELIVERIES		
C.4	TWO PROTOTYPES	8/30/93	◆ 1993 (A)
C.5	SSARs 1 THRU 3	11/27/94	◇ 1994 (N)
C.6	SSARs 4 THRU 6	1/22/95	◇ 1995 (J)
C.7	SSARs 7 THRU 10	1/22/95	◇ 1995 (J)
	CRUISE REPORTS		
C.8	DEPLOY SSARs 1-2	7/16/95	◇ 1995 (J)
C.9	DEPLOY SSARs 3-6	7/16/95	◇ 1995 (J)
C.10	DEPLOY SSARs 7-10	7/16/95	◇ 1995 (J)
C.11	SSAR FINAL REPORT	7/16/95	◇ 1995 (J)
D.1	70 HZ SOURCE ASSESSMENT		
D.1	MOORING FABRICATION REPORT		
D.2	AUTONOMOUS MOOR AT SEA TEST AND CRUISE REPORT		

Figure 1: GAMOT Deliverable Master Schedule

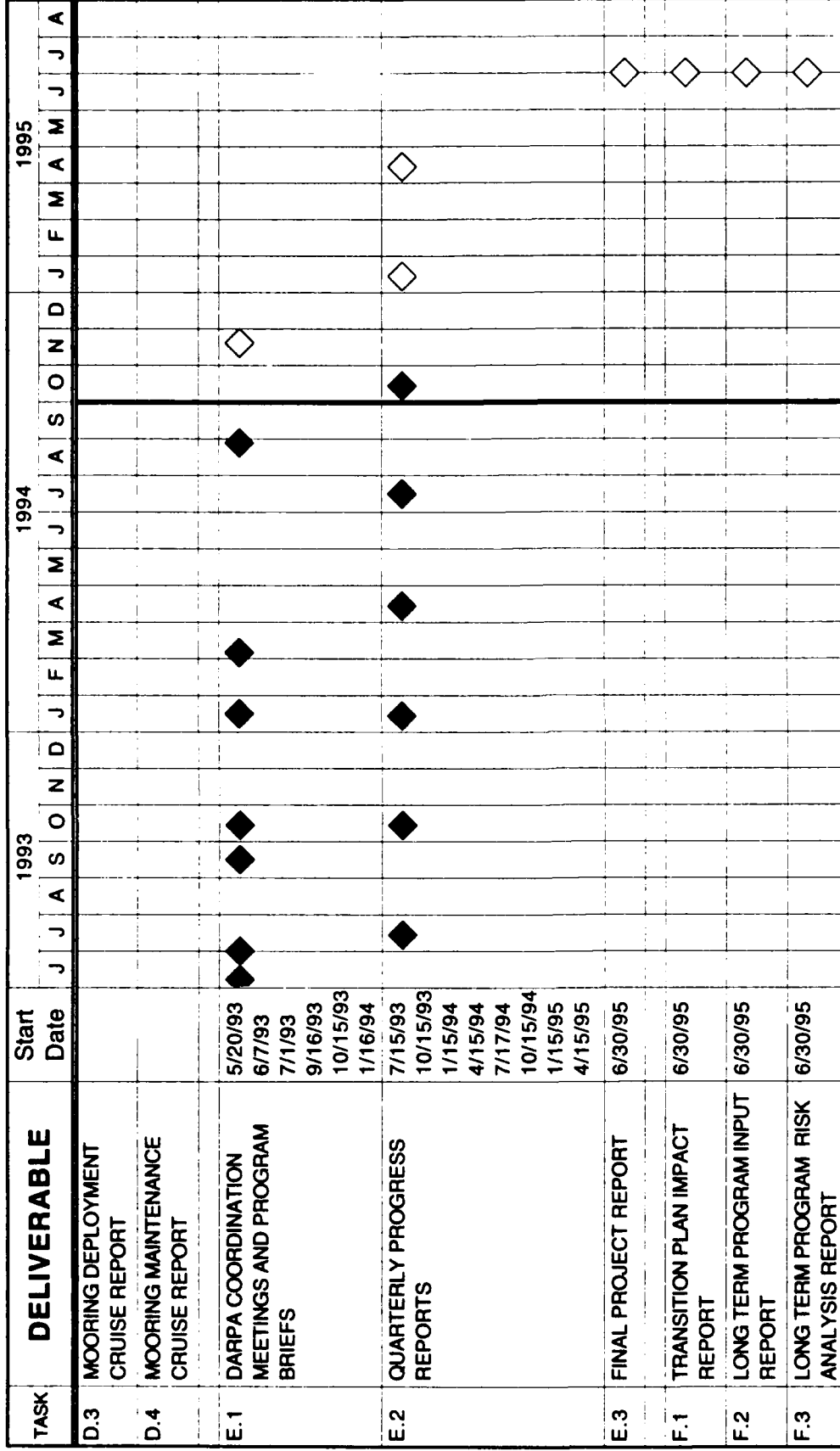| TASK	DELIVERABLE	Start Date
D.3	MOORING DEPLOYMENT CRUISE REPORT	
D.4	MOORING MAINTENANCE CRUISE REPORT	
E.1	DARPA COORDINATION MEETINGS AND PROGRAM BRIEFS	5/20/93, 6/7/93, 7/1/93, 9/16/93, 10/15/93, 1/16/94
E.2	QUARTERLY PROGRESS REPORTS	7/15/93, 10/15/93, 1/15/94, 4/15/94, 7/17/94, 10/15/94, 1/15/95, 4/15/95
E.3	FINAL PROJECT REPORT	6/30/95
F.1	TRANSITION PLAN IMPACT REPORT	6/30/95
F.2	LONG TERM PROGRAM INPUT REPORT	6/30/95
F.3	LONG TERM PROGRAM RISK ANALYSIS REPORT	6/30/95

Figure 1: GAMOT Deliverable Master Schedule